Dampening type 2 properties of group 2 innate lymphoid cells by a gammaherpesvirus infection reprograms alveolar macrophages

Authors: Pauline Loos[1], Jérôme Baiwir[1], Céline Maquet[1], Justine Javaux[1], Rémy Sandor[1], François Lallemand[2], Thomas Marichal[3], Bénédicte Machiels[1,†,*], Laurent Gillet[1,†,*]

Affiliations:
[1]Laboratory of Immunology and Vaccinology, Faculty of Veterinary Medicine, FARAH, ULiège, Liège, 4000, Belgium.
[2]Centre Hospitalier Universitaire de Liège, Département de Physique Médicale, Service médical de radiothérapie, Liège, 4000, Belgium.
[3]Laboratory of Immunophysiology, GIGA-Research and Faculty of Veterinary Medicine, ULiège, Liège, 4000, Belgium.

† co-senior authors
*Corresponding authors: L.gillet@uliege.be, bmachiels@uliege.be

Abstract: Immunological dysregulation in asthma is associated with changes in exposure to microorganisms early in life. Gammaherpesviruses (γHVs) are widespread human viruses that establish lifelong infection and profoundly shape host immunity. Using Murid herpesvirus 4 (MuHV-4), a mouse γHV, we show that after infection, lung-resident and recruited innate lymphoid group 2 cells (ILC2s) exhibit a reduced ability to expand and produce type 2 cytokines in response to house dust mites, thereby contributing to protection against asthma. In contrast, MuHV-4 infection triggers GM-CSF production by those lung ILC2s, which orders the differentiation of monocytes (Mo) into alveolar macrophages (AMs) without promoting their type 2 functions. In the context of γHV infection, ILC2s are therefore essential niche cells that imprint the tissue-specific identity of Mo-derived AMs and determine their function well beyond the initial acute infection.

One Sentence Summary: Gammaherpesvirus infection subverts lung ILC2s thereby promoting Mo-derived AM differentiation with reduced type 2 orientation.

INTRODUCTION

Asthma is a chronic inflammatory disease of the airways that affects more than 250 million people worldwide and causes around 500,000 deaths per year (*1*). Asthma is characterized by episodes of wheezing, coughing, chest tightness and shortness of breath. These symptoms are driven by aberrant airway inflammation and subsequent processes such as mucus hypersecretion, remodeling of the airway wall and bronchial hyperresponsiveness (*2*). The development and exacerbation of asthma are influenced by many environmental factors including infectious agents. Some respiratory viral infections can trigger severe adverse outcomes in patients at risk of asthma or with existing asthma (*3*). In particular, respiratory syncytial virus (RSV) and rhinovirus (RV) are the main drivers of asthma exacerbation in children and adults, respectively (*4*). While there is considerable epidemiological evidence to support these observations, the pathophysiological mechanisms are not well understood. In particular, the potential long-term effect of these infections on lung immune cells and the subsequent consequences on the development of asthma is not clear. Conversely, the "hygiene hypothesis" proposes that one reason for the dramatic increase in the occurrence of allergic diseases in western lifestyle countries could be linked to reduced exposure to microbes or microbial products during childhood (*5–7*). Epidemiological studies have shown that higher levels of circulating IgE were observed in children who were infected late with a human gammaherpesvirus (γHV), the Epstein Barr virus (EBV), compared to children who were infected early during childhood (*8*). In this context, we recently showed that Murid herpesvirus 4 (MuHV-4), a mouse model for EBV, has long-term inhibitory effects on the development of house dust mites (HDM)-induced airway allergy (*9*). Specifically, MuHV-4 infection induced the replacement of resident alveolar macrophages (AMs) by monocyte-derived (Mo-) AMs that blocked the development of a type 2 T helper (TH2) response against HDM (*9*). However, the initial immunological mechanism underlying this observation is still completely unknown.

Innate lymphoid cells (ILCs) are a heterogeneous family of cells that are particularly abundant at barrier surfaces where they act as first line innate immune sensors (*10–12*). Group 2 ILCs (ILC2s) are the predominant ILC population in the lung at steady state (*13*). While ILC2s are essential to promote type 2 inflammation against helminths (*14–16*), they also control eosinophil homeostasis (*17*) and play a major role in chronic type 2 inflammatory diseases such as asthma (*18–22*). Thus, ILC2s are essential for the initiation and persistence of type 2 inflammation in protease and HDM-induced models of airway allergy (*20, 22–24*). ILC2s expand in response to various signals including epithelial cytokines (IL-25, IL-33 and thymic stromal lymphopoietin (TSLP)), lipid mediators and neurotransmitters (*25–30*). Based on the integration of these signals, ILC2s can affect the function of their neighboring cells through the cytokines they produce or *via* direct cell-cell interactions. Respiratory viruses associated with asthma exacerbation, such as RSV, RV or influenza virus, have been shown to increase the number of ILC2s and to promote their activation and production of type 2 cytokines (*31*). In contrast, the long-term impact of persistent viruses, such as MuHV-4, on ILC2s function is still unknown.

In this study, we investigate how infection history shapes long-term lung immunity. We demonstrate that MuHV-4 infection modulates the dialogue between ILC2s and AMs in an IFN-γ-dependent manner with major consequences for the development of asthma. Specifically, we demonstrate the key role of pulmonary ILC2s in conferring identity and functional specification of Mo-AMs after virus-induced niche depletion. We further show that ILC2-derived GM-CSF is necessary to promote differentiation of Mo-AMs after MuHV-4 infection. Our results reveal

73 important insights into ILC2-dependent AM plasticity following γHV infection with long-term
74 consequences for host allergic susceptibility.

RESULTS

MuHV-4 infection reduces the number of lung ILC2s and modifies their functional properties in response to subsequent HDM exposure

To investigate whether γHV infection affects pulmonary ILC2s over the long term with possible consequences for the development of type 2 responses, BALB/c mice were infected or not with MuHV-4 and subjected to HDM-induced airway allergy (Fig. 1A). Lung innate immune response was analyzed by flow cytometry one day after the first HDM instillation (sensitization) and three days after the last instillation (challenge). As previously shown (*9*), MuHV-4 infection conferred protection against HDM-induced airway allergy as illustrated by the reduced eosinophilia observed in MuHV-4-infected mice (Fig. 1B). Lung ILC2s were identified as Lin^- $CD45^+CD90.2^+$ $ST2^+CD25^+$ live cells (with lineage composed of B220, CD11c, CD3, CD4, CD49b, CD5, CD8α, F4/80, FcεR1, Gr1 and Siglec-F markers) (Fig. 1C) and pulmonary ILC1s and some ILC3s have been jointly identified as $CD45^+Lin^-NKp46^+$ living cells (*32*). Interestingly, in contrast with mock infected mice, we did not observe an increase in lung ILC2 number in MuHV-4 infected mice after HDM challenge, an observation that was not associated with differences in ILC1s or ILC3s (Fig. 1D). Moreover, within MuHV-4 infected mice, ILC2s displayed decreased expression of GATA3 and reduced production of IL-13 and IL-5 upon *ex vivo* stimulation both at sensitization and challenge phases (Fig. 1, E-I), suggesting that mouse infection by MuHV-4 affects the functional properties of lung ILC2s upon HDM treatment. In order to directly assess IL-5 production *in vivo*, we repeated those experiments using IL-5 reporter mice (IL5-tdtomato-cre, also called Red5) (*33*) subjected to HDM-induced airway allergy (Fig. S1A) and analyzed the number and function of lung ILC2s (Fig. S1B). In line with the reduced lung eosinophilia (Fig. S1C), MuHV-4 infection blocked the increase of lung ILC2 number observed upon HDM challenge in mock infected mice (Fig. S1D). Similar to BALB/c mice, ILC2s from MuHV-4 infected Red5 C57BL/6 mice also displayed lower GATA3 expression and IL-5 production compared to mock infected mice both at HDM sensitization and challenge (Fig. S1, E-H). Furthermore, this also revealed a reduced expansion of IL-5-producing T cells in MuHV-4 infected mice (Fig. S1I). Finally, these differences in the number of IL-5-producing cells were readily visible in lung sections in which numerous ILC2s were observed within the lung parenchyma of uninfected and HDM-challenged mice, while they were hardly found in lungs of corresponding MuHV-4 infected mice (Fig. S1, J and K). Overall, these observations revealed that the history of MuHV-4 infection profoundly modifies the pool of lung ILC2s and affects their ability to initiate and amplify an effective HDM-induced type 2 response.

MuHV-4 infection impairs both the expansion and recruitment of pulmonary ILC2s

While we did not observe any differences of ILC2 apoptosis or necrosis between groups (Fig. 1, J-K), we observed a significant difference in ILC2 ability to proliferate upon HDM challenge between groups, as demonstrated by the reduction of $Ki67^+$ ILC2s (Fig. 1, J and L). We then assessed whether HDM treatment could induce the presence of ILC2 from a recruited origin (either recruitment of ILC progenitors (*34*) or of ILC2s from bone marrow (BM) or from other tissues (*35*)) and whether MuHV-4 infection could affect it. To this end, BALB/c $CD45.2^+$ mice were lethally irradiated with the exception of the thoracic cavity to spare lung-resident cells. These recipient mice were transplanted with BM from $CD45.1^+$ BALB/c congenic donors. Eight weeks after irradiation and BM transfer, mice were infected or not with MuHV-4 and then subjected to

HDM sensitization and challenge (Fig. 1M-P). As expected, MuHV-4 infection conferred protection against HDM-induced airway allergy as demonstrated by the reduced eosinophilia (Fig. 1N). HDM challenge induced the presence of ILC2s from a recruited origin that were significantly reduced in MuHV-4 infected mice (Fig. 1O-P). Moreover, cells of both origins were similarly affected by MuHV-4 infection for their capacity to produce type 2 cytokines (Fig. 1O-P). Similar results were obtained in C57BL/6 mice upon HDM challenge (Fig. S1 L-Q). Taken together, these data demonstrate that MuHV-4 infection impairs the proliferation, recruitment and pro-TH2 functions of lung ILC2s following HDM challenge, irrespective of the ontogeny of these ILC2s.

MuHV-4 infection imprints substantial changes on lung ILC2 transcriptional program

We then performed single-cell RNA sequencing on sorted ILC2s after MuHV-4 infection and/or HDM instillations, (Fig. 2A and Fig. S2, A-F). As ILC2s can acquire ILC1-like properties under the influence of the cytokine microenvironment (*36*), we assessed the potential plasticity of these cells by monitoring the expression of specific transcription factors following MuHV-4 infection and HDM treatments. In contrast to previous studies on ILC2s after other respiratory viral infections (*37*), we did not observe increased expression of *Tbx21* (T-bet) or *Rorc* (RORγt) in lung ILC2s from any group (Fig. 2B). Accordingly, no increase in T-bet or IFN-γ levels was observed by flow cytometry after MuHV-4 infection as compared to mock-infected mice (Fig. 2C). In contrast, expression of *Gata3* and *Rorα* (*38*) were significantly higher after HDM challenge in lung ILC2s from mock infected mice compared to their MuHV-4 counterparts (Fig. 2B), supporting the negative regulation of ILC2s by infection.

In order to identify any potential effect of the infection on some specific ILC2 subsets, we partitioned transcriptionally distinct ILC2s into 5 clusters and projected cells in two dimensions, using Uniform Manifold and Projection (UMAP) (Fig. 2D). Then, we selected the top 10 genes differentially expressed (DE) across clusters to define the phenotypic heterogeneity underlying each cell cluster and their proportion within the different conditions (Fig. 2D-F). Unexpectedly, we did not observe any significant enrichment of any ILC2 subset over another upon MuHV-4 infection alone or following HDM exposures (Fig. 2F). Bulk analysis of DE genes identified significant upregulation of genes associated with ILC2 activation such as *Pdcd1* and *Klrg1* in mock infected mice after HDM sensitization, and *Il-13* after HDM challenge, within ILC2 from mock infected mice compared to MuHV-4 infected mice (Fig. 2G-H). Interestingly, expression of PD-1 in ILC2s is an important regulator of the maturation marker KLRG1 in ILC2s (*39*, *40*). These differences in expression of PD-1 and KLRG1 following HDM sensitization were also confirmed by flow cytometry analysis (Fig. 2I-J). At the same time, *Ly6a* expression, encoding the IFN-inducible GPI-linked protein Sca-1 involved in cell-cell adhesion and signaling (*41*), was higher in ILC2s from MuHV-4 infected mice (Fig. 2J). Interestingly, some differences were already observed prior to any HDM stimulation, as shown by higher expression of genes involved in tissue repair (*Areg*) or response to IFN-γ (*Ifrd1*, *Stat1*) (Fig. 2G-H). In particular, ST2 expression (encoded by *Il1rl1*) appeared to be reduced in ILC2s from MuHV-4 infected mice prior to any HDM treatment (Fig. 2 G, I and J). This difference was even increased upon sensitization to HDM while IL-33 production was similar between infected and uninfected mice (Fig 2 K and L) providing a potential mechanistic explanation of the lower responsiveness of ILC2s in MuHV-4 infected mice.

Finally, gene-set enrichment analysis of transcriptomic data, revealed that HDM challenge induced the upregulation of genes involved in TH2 immunity and lymphocyte migration in ILC2s from mock infected mice in comparison with ILC2s from MuHV-4 infected mice (Fig. 2M). In contrast, increased expression of genes playing a role in negative regulation of innate immune response was observed in ILC2s from infected mice upon HDM challenge (Fig. 2M). Especially, our analysis highlighted that infection with MuHV-4 induced substantially higher expression of genes involved in response to IFN-γ, which is a well-known inhibitor of ILC2s (*42*, *43*) (Fig. 2M). Interestingly, ILC2s from MuHV-4 infected mice appeared to display reduced orientation of their metabolism towards aerobic respiration in comparison with ILC2s from mock infected mice, suggestive of the involvement of metabolism in regulating their function.

IFN-γ directs the functional impairment of pulmonary ILC2s after MuHV-4 infection

MuHV-4 latency is associated with elevated levels of IFN-γ (*9*, *44*) and BubbleGUM analysis revealed a strong IFN-γ related alteration on MuHV-4 ILC2s (Fig. 2M). To determine whether inhibition of pulmonary ILC2s was directly dependent on IFN-γ signaling, we generated mixed BM chimeras, in which C57BL/6 CD45.1.2^{+} mice were exposed to a complete lethal irradiation protocol and then transplanted with a mix (1:1) of BM cells from C57BL/6 CD45.1^{+} and from C57BL/6 IFN-γR$^{-/-}$ CD45.2^{+} congenic donors. 8 weeks after BM transplantation, mice were subjected to MuHV-4 infection and subsequent HDM treatment (Fig. 3A). The mixed chimera model allowed us to track the production of type 2 cytokines from wild-type (WT) ILC2s and from ILC2s lacking IFN-γ receptor in the same mouse. Interestingly, reduced production of IL-5 and IL-13 by ILC2s following infection was only observed in WT cells while ILC2s lacking IFN-γ receptor produced more IL-5 or IL-13 than WT ILC2s (Fig. 3 B and C), indicating that IFN-γ sensing by ILC2s blocks type 2 cytokine production by these cells and plays a role in the protection conferred against HDM-induced airway allergy. Accordingly, in those mice, we did not observe any reduction in the number of ILC2s following MuHV-4 infection or protection against lung eosinophilia (Fig. 3 D and E). Altogether, these data revealed that inhibition of ILC2 responses following MuHV-4 infection was dependent on direct IFN-γ sensing.

In BALF, a peak of IFN-γ production occurs at day 8 after MuHV-4 infection (Fig. 3F) (*45*). We therefore assessed the impact of MuHV-4 infection on lung ILC2s before any HDM treatment (Fig. 3 G-I). The phenotype of ILC2s was altered as early as 5 days post-infection with a transient increased expression of Sca1 and PD-1 (Fig. 3I). Interestingly, PD-1 acts as a metabolic checkpoint in ILC2s to restrain inflammation (*46*). This was associated with a decrease in the percentage of IL-13^{+} ILC2s correlating with the peak of IFN-γ (Fig. 3H). Using the same mixed chimera model as in Fig. 3A, we confirmed a major role of IFN-γ in inhibiting lung ILC2s at early time points post-infection (Fig. 3, J-L). Importantly, protection against airway allergy was maintained even 3 months post-infection and was associated with a decrease in proliferation and cytokine production by lung ILC2s in the infected groups subjected to allergic challenge (Fig. 3, M-P). Moreover, these modifications were also observed after infection with a latency-deficient MuHV-4 mutant (*47*) (Fig. 3, M-P), demonstrating that functional changes in ILC2s persist even in the absence of long-term IFN-γ production. This observation underlines the imprinting effect of infection on ILC2s associated with the peak of IFN-γ released into the airway during acute infection.

Monocyte-derived alveolar macrophages reconstituting the alveolar niche after infection are in close contact with lung ILC2s

We have previously demonstrated the necessary and sufficient role of Mo-AMs in the protection conferred by MuHV-4 against allergic asthma (*9*). Therefore, we investigated a possible link between MuHV-4-imprinted ILC2s and the functional properties of AMs reconstituting the alveolar niche after infection. As observed previously, day 8 post-MuHV-4 infection correlates with the depletion of the AM niche and the recruitment of Mos associated with MHC-II overexpression and Siglec-F downregulation (Fig. 4, A-C). To assess first whether ILC2s and AMs are able to interact closely, we performed imaging of lungs from IL-5 reporter mice at days 0, 5, 8, 14 and 28 post-infection and observed ILC2s and AMs in close contact at all post-infection times (Fig. 4, D-H). MuHV-4 infection induced a massive infiltration of immune cells in the bronchovascular areas at day 8 post-infection (Fig. 4E). In those clusters, we observed T cells ($CD3^+$), myeloid cells ($CD68^+$) and ILC2s ($CD3^-IL\text{-}5^+$). 28 days post-infection, inflammation was resolved with some remaining T cells observed (Fig. 4E). In order to better define the cell-cell interactions upon infection, we distinguished resident AMs ($CD68^+CD11c^+$) from Mos ($CD68^+CD11b^+$) and Mo-derived AMs ($CD68^+CD11c^+CD11b^+$) (Fig. 4 F-G) and quantified the distance between these subsets and ILC2s, in comparison to the distance with another cell type as control. We observed that 50% of ILC2s were at least in close contact (shortest distance <5µm) with myeloid cells (Fig. 4G) and most of them were even closer (shortest distance <1µm), a distance that had been shown to allow direct cell contacts (*48*) (Fig. 4H and Supplementary Movie 1), with temporal changes correlating with AM niche depletion and replenishment. On the contrary, such close interactions were not observed so frequently with control cells (neutrophils identified as $CD68^-$, $CD11b^+$) (Fig. 4, G), suggesting that the close contacts observed between ILC2s and myeloid cells may have biological relevance for the immune landscape of the alveolar niche after MuHV-4 infection.

MuHV-4 infection induces concomitant changes in the transcriptional profiles of AM and ILC2, suggestive of key cell-cell interactions underlying AM differentiation and identity

To assess the modifications induced by MuHV-4 infection on ILCs and AMs and a possible crosstalk between those cells, ILCs and AMs were sorted and profiled by scRNA-sequencing at different times post-infection (Fig. 5 A-B and Fig. S2, G-M). Lung ILC2s represented more than 95% of the lung ILC populations and this proportion was maintained throughout the infection (Fig. 5C). As early as 5 days after infection, ILC2 activation was observed as indicated by increased expression of *Klrg1*, *Il-5* and *Il-13* (Fig. S3A). Moreover, lung ILC2s also seemed to play a role in lung homeostasis following MuHV-4 infection based on production of *Areg*, essential for maintaining epithelial integrity and airway remodeling to restore lung function (*49*). Nevertheless, we detected a subsequent downregulation of *Pdcd1* (PD-1), *Klrg1* and *Arg1*, reduction of cytokine production correlating with upregulation of *Ifit1* and *Ifitm3* genes related to IFN-γ signaling by lung ILC2s from day 8 post-infection (Fig. S3A). Analysis of phenotypic molecular signatures with BubbleGUM confirmed that infection with MuHV-4 induced a higher expression of genes negatively regulating immune system processes and genes involved in response to viral infection, tolerance and response to IFN-γ. Finally, genes implicated in cellular respiration were downregulated in ILC2s from MuHV-4 infected mice, which could imply reduced aerobic respiration (Fig. S3B). Clustering of ILC2s showed that ILC2s producing *Areg* (cluster 0) were proportionally more abundant at day 8 post-infection (Fig. 5, D-F). This highlights a possible role

of ILC2s in tissue repair after initial acute infection, as found for influenza virus infection (*49*) confirming that MuHV-4 infection affects lung ILC2s much earlier than HDM instillations.

Next, we performed clustering of AMs to better define changes in AM heterogeneity upon MuHV-4 infection. We identified 7 different subsets characterized by distinct transcriptional profiles and whose proportion varied over time (Fig. 5, G and H). To infer transcriptional dynamics between these cell subsets, we applied RNA velocity analysis (*50*) (Fig. 5I). This analysis clearly showed a transition from subsets 3-4 to subsets 1-2 and then to subsets 0-5 (Fig. 5I). Based on the relative proportion of the different subsets over time (Fig. 5I), and on canonical phenotypic markers such as SiglecF, ApoE and CCR2 (*9*, *45*), we identified recruited Mos (subsets 3-4), differentiated AMs (subsets 0 and 5) and cells differentiating into AMs (subsets 1-2) (Fig. 5, J and K). Interestingly, clusters 0 and 5, identified as differentiated AMs, is present before infection, disappears and is then re-enriched on day 28 (Fig. 5 G and H). The low level of Ki67 expression in most of these clusters (except cluster 5) reinforce the view that these are recruited cells differentiating *in situ* as suggested by the velocity analysis (Fig. 5 I) but that do not multiply. In contrast, cluster 5 expressing high level of Ki67 (Fig. 5 K) potentially represents a self-renewing subpopulation of resident AMs. Bulk transcriptome analysis over the different time points showed that AMs from mock infected mice displayed a M2/resting profile, as shown by the overexpression of genes such as *Marco*, *CD36*, *Chil3* and *Fabp4* (Fig. S3C). In contrast, AMs from MuHV-4 infected mice exhibited a shift towards classical macrophage activation (M1), overexpression of MHC-II and downregulation of SiglecF (Fig. S3C). BubbleGUM analysis confirmed these observations and highlighted regulatory properties associated with production of IL-10 at days 5 and 8 post-infection (Fig. S3D). Altogether, this analysis highlights that, following MuHV-4 infection, resident AMs displaying a M2 phenotype are progressively and mainly replaced by Mo-derived AMs displaying M1 and regulatory properties.

In allergic asthma or in early life, ILC2s coordinate the polarization of AMs to a M2 phenotype (*51*, *52*). To assess a potential crosstalk between ILC2s and myeloid cells (differentiated AMs, Mo differentiating into AMs and Mos) during MuHV-4 infection, we extrapolated putative interactions from transcriptomic data using NicheNET analysis (*53*). This analysis allowed us to characterize ligands expressed by ILC2s and myeloid cells, their associated receptors and the target genes activated by these interactions (Fig. 5L and M). Interestingly, our analysis highlighted that production of GM-CSF (*Csf2*) by ILC2s (Fig. 5L) could educate incoming Mos towards AMs as this cytokine is essential for AM development in early life (*54*). Furthermore, 5 days post-infection, they might produce Cxcl10 (*Cxcl10*), also known as IFNɣ-induced protein 10, that could induce the chemotaxis of Mos from the BM (*55*, *56*) (Fig. S3A and E). Twenty-eight days post-infection, interaction seems to rely on *Ptprc* expression by ILC2s and CD44 by Mos differentiating into AMs and AMs (Fig S3F). This interaction is known to regulate AM homeostasis and lung inflammation (*57*). Conversely, long-term *Il-1β* production by Mo-derived AMs may contribute to control lung ILC2s as previously shown (*36*) (Fig. 5M). These data further point to a complex crosstalk between MuHV-4-imprinted ILC2s and Mo-derived AMs that may shape long-term alveolar niche immunity.

MuHV-4 infection inhibits the capacity of lung ILC2s to polarize AMs towards a "M2-phenotype" *ex vivo*.

We next confirmed the potential role of lung ILC2s on AM maturation in *ex vivo* co-cultures (Fig. 6A and Fig. S4A). To obtain Mos in the process of differentiation into AMs, we first co-cultured BM Mos with lung epithelial cells (ECs) from naïve mice for 3 days (Fig. 6 and S4). ILC2s from mock or MuHV-4 infected mice were then added (Fig. 6A). ILC2s from MuHV-4 infected mice maintained their expression of Sca1 (Fig. 6B). A substantial fraction of BM-Mos differentiated into AM-like cells, as observed by the expression of CD11c (Fig. 6C). As previously described (*51*), Mo-derived macrophages acquired the M2 marker Arg1 when co-cultured with ILC2s from mock infected mice (Fig. 6C). In contrast, Mo-derived macrophages in culture with ILC2s from MuHV-4 infected mice showed less expression of Arg1 and an increased expression of MHC-II (Fig. 6C). AMs isolated from BALF and co-cultured with ILC2s do not show such phenotypic plasticity, suggesting a greater sensitivity of differentiating Mos to education by ILC2s. (Fig. S5).

We then performed transcriptomic analysis of *ex vivo* differentiated Mo-derived macrophages (defined as $Ly6G^-$, $Ly6C^-$, autofluorescent, $CD11c^+$ living cells) in the presence of lung ECs and cultured or not with lung ILC2s from mock or MuHV-4 infected mice. Macrophage identity was confirmed by the expression of associated genes (Fig. 6D). Principal component analysis revealed major differences depending mainly on the presence or absence of ILC2s (Fig. 6E). In particular, lung ILC2s induced expression of genes related to macrophage differentiation and activation (*Csf1*, *Pparg*, *Il4ra*) and chemotaxis (*Ccr7*) (Fig. 6F). Genes that were differentially expressed between the conditions were classified with PANTHER (Fig. 6G). This revealed highly significant enrichments for pathways such as macrophage differentiation, activation or chemotaxis. In total, we observed 112 differentially expressed genes ($P < 0.05$) between Mos cultured with ILC2s from mock or infected mice (Fig. 6F). While ILC2s from mock infected mice promoted Mo-derived AMs differentiation (*Pparg*) and a M2 polarization phenotype (*Arg1*, *Chil3*, *Ear2*, *Fabp4*, *Il1r2*), macrophages cultured with ILC2s from MuHV-4 infected mice, in addition to not overexpressing M2-gene profiles, displayed expression of genes related to immunosuppression such as *Csf3r*, or to regulatory orientation such as *Socs3* (Fig. 6, H and I). Altogether, these data indicate that, *in vitro*, besides positively regulating macrophage differentiation, lung ILC2s from MuHV-4 infected mice are not able to prone a M2 phenotype of Mo-derived AMs.

Lung ILC2s from MuHV-4 infected mice promote Mo-AM differentiation through GM-CSF with subsequent *in vivo* consequences for HDM-induced airway allergy.

As our NicheNet analysis highlighted that GM-CSF may be a major mediator of crosstalk between ILC2s and Mos differentiating into AMs after MuHV-4 infection (Fig. 5L), we investigated the role of GM-CSF in this context. To this end, Mos from BM or BALF AMs from naïve mice were co-cultured with lung ECs along with ILC2s from mock- or infected-mice during three days, with or without antibody blocking GM-CSF activity (Fig. 7A). As already observed (Fig. 6), Mos undergo a wave of differentiation into AMs, with several stages of differentiation identifiable after 3 days of co-culture (Fig. 7, B and C). Interestingly, ILC2s from infected mice were found to be more effective in inducing Mo differentiation into AMs, as indicated by their higher expression of CD11c compared to ILC2s from mock-infected mice (Fig. 7F). While GM-CSF neutralizing antibodies did not affect the numbers of AMs, Mos or Mo-derived AMs when these cells were cultured with ECs alone (Fig. 7, D and E), they strongly blocked the increase in numbers of these cells observed in the presence of ILC2s. This effect was particularly marked in

the presence of ILC2s from MuHV-4 infected mice (Fig. 7, E-G), demonstrating that lung ILC2s from MuHV-4 infected mice promote the differentiation of Mo-derived AMs through GM-CSF production. Importantly, *ex vivo* co-culture of ILC2s, from mock infected or MuHV-4 infected mice, failed to polarize resident AMs from mock infected mice towards a M2 phenotype (Fig. S5) whereas Mo-derived AMs were sensitive to ILC2-induced polarization (Fig. 6). MuHV-4 promoted the production of GM-CSF by lung ILC2s and simultaneously decreased production of type 2 cytokines (such as IL-13) by ILC2s 8 days post-infection (Fig. 3L). We therefore examined the effects of IL-13, as its production has been described to polarize AMs to a M2 phenotype with homeostatic functions (*52*). Repeated instillations of rIL-13 in MuHV-4 infected mice were sufficient to polarize AMs from infected mice to a M2 phenotype (Fig. 7, H and I), supporting that decreased production of IL-13 by ILC2s contributes to the absence of M2 phenotype of Mo-derived AMs following MuHV-4 infection.

Afterwards, to assess the importance of the ILC2-AM crosstalk in the context of *in vivo* replenishment of the alveolar niche by incoming Mos, we used ILC2s deficient mice (*Rorα*$^{lox/lox}$ *Il7r*$^{Cre/+}$) (*58*), infected or not with MuHV-4, and subjected to HDM sensitization and challenge (Fig. 7J). In mock infected littermates, AMs expressed M2 markers such as YM1/CHIL3 at steady state as described (*59*). In contrast, decreased expression of these markers was observed in the absence of ILC2s (Fig. 7K). Similarly, the M2 marker RELMα was not increased in ILC2-deficient mice following HDM instillations (Fig. 7L). The absence of eosinophilia observed following HDM-induced airway allergy highlighted the essential role of ILC2s in allergic challenge (Fig. 7M-N). This was associated with the lack of an M2 phenotype of AMs following HDM challenge, based on the expression of RELMα and Arg1 (Fig. 7O). These findings confirmed that ILC2s were essential to promote a M2-AM profile at steady state, and after HDM instillations in mock infected mice. Conversely, upon MuHV-4 infection, AMs from infected littermate mice showed the same profile as those from ILC2-deficient mice, meaning an absence of M2 polarization irrespective of HDM stimulation (Fig. 7, K, L and O).

Finally, we performed AM transfer to address their functionality in the absence or presence of lung ILC2s (Fig. 7P). AMs from WT or ILC2s deficient mice, infected or not with MuHV-4, were transferred intranasally to recipient mice expressing CD45.1 and then subjected to HDM sensitization and challenge (Fig. 7P). As already described (*9*), AMs from MuHV-4 infected mice maintained their phenotypic changes including overexpression of MHC-II and downregulation of Siglec-F (Fig. 7Q). AM transfer from littermate mock mice amplified the type 2 immune response, as indicated by increased BALF eosinophils counts (Fig. 7R). Remarkably, this amplification did not occur with AM transfer from mock infected ILC2s deficient mice (Fig. 7R), confirming that ILC2s instruct AMs toward M2 polarization profile and amplify a type 2 immune response. AMs from WT and ILC2-deficient MuHV-4 infected mice were similarly sufficient to provide protection against HDM-induced airway allergy, attesting again the absence of TH2 properties of ILC2s from MuHV-4 infected mice (Fig. 7R).

DISCUSSION

ILC2s are key players in the initiation and maintenance of allergic asthma (*20*, *24*). Viruses known to trigger or exacerbate asthmatic symptoms, such as RV or RSV are associated with expansion and activation of ILC2s (*60–62*). In contrast, the effect of persistent viruses, such as herpesviruses, on ILC2s was unknown. Here, we showed that ILC2s from γHV infected mice displayed long-term decreased expression of canonical type 2 markers but were able to promote the differentiation of Mo-derived AMs without promoting their type 2 functions.

We observed that ILC2s from MuHV-4 infected mice have a reduced capacity to expand in response to type 2 stimuli, due to reduced recruitment and proliferation. In asthmatic human, circulation of ILC2s into the blood has been described (*63*), suggesting recruitment of ILC2s to specific tissues. Although the recruitment of ILC2s has been described in mice (*35*), this is not clear if it occurs in allergic asthma. Thus, some authors did not detect any recruitment of ILC2s in the lungs after administration of HDM (*64*), while others observed that the administration of HDM activated IL-33 responsive ILC2s in the BM suggesting potential mobilization and tissue recruitment (*65*). The partial chimera model used here definitely demonstrated the recruitment of ILC2s into the lung after HDM challenge. However, different ILC2 populations could not be identified through sc-trancriptomics. On the contrary, modifications of gene expression within ILC2s was rather uniform, with activation in the early post-infection period, and then, a gradual return to the baseline situation with the maintenance of a reduced number of transcriptomic changes (Fig. 5 and Fig. S3). Comparison of corresponding groups in the two scRNAseq experiments, performed on BALB/c and C57BL/6 mice respectively, revealed important similarities. In particular, the transcriptome modifications in response to MuHV-4 infection were homogeneous within ILC2s and mainly marked by the expression of genes associated with the negative regulation of innate immune responses and with response to IFN-γ (Fig. 2, Fig. 5 and Fig. S3).

IFN-γ is a known inhibitor of ILC2s (*42*, *43*, *66*). However, while IFN-γ release induces a transient ILC2 counter regulation during influenza infection (*67*), we observed that MuHV-4 infection, irrespective of latency establishment (Fig. 3 M-P), sustains long-term regulation of those cells. It therefore seems that it is the initial peak of IFN-γ rather than its long-term production that impacts the functions of ILC2s. In the future, it will be interesting to investigate the role of IFN-γ on ILC2s as a trigger for a long-term trained immunity state. The maintenance of this effect could also rely on a dialogue between ILC2s and Mo-derived AMs. For example, Mo-derived AMs produced IL-1β, a critical regulator of ILC2 function and plasticity (*68*) and PD-L1 that could interact with PD-1 at the ILC2 surface. Several recent studies, have indeed demonstrated the crucial role played by recruited monocytes in the regulation of the lung microenvironment after viral infections (*45*, *69*).

Besides the influence of extrinsic factors, intrinsic intracellular alterations, induced at early time points post-infection, could play a key role in sustaining ILC2 functional profile. In that context, epigenetic and metabolic modulation are now well-established as sources of long-term changes in the immunological phenotype of innate immune cells (*70*, *71*). Thus, cytomegalovirus infection has been described to drive adaptive epigenetic diversification of NK cells with altered effector functions (*72*). This has not yet been shown for ILC2s, even if more than 300 asthma-associated genetic polymorphisms identified in genome-wide association studies have been

localized to H3K4Me2 gene regulatory elements in ILC2s (*73*). Interestingly, epigenetic modifications in innate lymphoid progenitor induce glycolysis which in turn decreases ST2 expression and inhibits ILC2s activation by IL-33 (*62*). Similarly, we observed a reduction of ST2 expression by ILC2s following MuHV-4 infection (Fig. 2 I-J).

In addition to the direct influences on lung immunity, we showed important role for ILC2s in shaping the alveolar landscape upon infections. Tissue resident macrophages, such as AMs, display unique transcriptomic profiles (*74*, *75*). However, how they acquire these profiles is still poorly understood. During physiological lung development, crosstalk between ILC2s, basophils and alveolar type II ECs seems to modulate the development of AMs (*76*, *77*). This crosstalk occurs notably during first breath after birth when the alveolar expansion correlates with production of IL-33, which expands and activates ILC2s. In these conditions, ILC2s produce IL-13 that polarizes newly differentiating AMs to a M2 phenotype with homeostatic functions (*52*). How circulating Mos acquire macrophage properties and establish in tissues later in life is much largely unknown (*77*).

The macrophage niche model states that embryonic or adult macrophage precursors have an almost identical potential to develop into tissue-resident macrophages, while competing for a restricted number of niches (*78*). However, pathways promoting macrophage replenishment and phenotype could rely on immune shaping by specific microbes. Here, we showed that MuHV-4 imprinted-ILC2s were able to coordinate the differentiation of recruited Mo into Mo-derived AMs, but did not confer them a M2 polarization as it could have been expected (*52*, *76*). Indeed, we established that ILC2s and ECs alone can reproduce *in vitro* an alveolar niche, which is sufficient to promote the differentiation of Mos into AM-like cells as revealed by the expression of PPAR-γ (Fig. 6 and 7), a transcription factor essential for the identity and function of AMs (*79*). Crucially, we highlighted the importance of GM-CSF production by MuHV-4-imprinted ILC2s to optimize the differentiation of Mo into mature AMs. Previous work has identified the function of GM-CSF, restricted to alveolar type 2 cells, in instructing AM fate, establishing the postnatal AM compartment, and maintaining AM pool in adult lungs (*80*). While these data have been described in steady state, we highlighted here, in the context of depletion of the alveolar niche by MuHV-4 infection, the necessary and sufficient role of ILC2 derived GM-CSF in driving Mo-AM differentiation. Further work is required to dissect the role of GM-CSF across macrophage subsets during inflammation and infection. Thus, while alterations in the ILC2/AM axis could explain part of the differences in susceptibility to the development of allergic asthma, they could also be involved in immunopathologies induced by viral infections such as COVID-19. Indeed, insufficient GM-CSF production in the airways of patients severely affected by SARS-CoV2 infection has been reported (*81*). Interestingly, clinical trials seem to show that early treatments with inhaled GM-CSF could restore alveolar gas exchange and simultaneously boost anti-SARS-CoV2 immunity potentially through Mo-derived AMs instruction (*82*). The role of ILC2s in the education of Mo-derived AMs and the resulting functional consequences should also be investigated in the context of influenza virus infection, as it has recently been shown that these cells determine the severity of the disease associated with this infection (*69*). Investigating potential functional alterations of lung ILC2s in these contexts could therefore open new therapeutic perspectives.

In the end, ILC2s are probably not the only cells that contribute to the functional education of Mo-derived AMs. Indeed, the transfer of Mo-derived AMs from ILC2s-deficient mice is still

accompanied by protection against allergic asthma, indicating that other factors are probably involved. Accordingly, our previous observation of phenotypic changes in Mos within the BM following MuHV-4 infection (*9*) suggests the existence of central imprinting of Mos in addition to their peripheral education.

Overall, this work substantially expands the understanding of γHV imprinting of lung immunity. In particular, it reveals the central importance of ILC2s to confer AM identity to Mos filling the niche following viral infection. As such, MuHV-4 imprinted ILC2s exhibit long-term alterations regulating the *in vivo* phenotypic and functional dynamics of AMs during allergic asthma. From a more general point of view, these results also suggest a central role for ILC2s in maintaining the delicate equilibrium between γHVs and the host immune system.

MATERIALS AND METHODS

Study design

The main goal of this study was to explore the long term effect of a γHV infection on lung ILC2s and the potential consequences on lung type 2 immune responses. The experiments were performed in mice using mouse genetics and molecular and cellular immunology approaches. In most of the experiments, 4 to 10 mice per group per time point were used to identify differences between groups with at least 80% power and 5% significance level. No data were excluded from the analysis and all replication gave similar readout. Allocation of animals into groups was done randomly at the start of the experiments. The specific numbers and genotypes of mice, the experimental replicates and the statistics performed are included in each figure legend.

Mice.

This study was conducted in accordance with guidelines of the European Convention for the Protection of Vertebrate Animals used for Experimental and other Scientific Purposes (CETS 123). Animal experiments were performed as specified in protocols approved by Committee on the Ethics of Animal Experiments of the University of Liege (permit number: 1845). All inoculations were performed under isoflurane anesthesia and every effort was made to minimize suffering.
Female BALB/c or C57BL/6 WT mice were purchased from Charles River (l'Arbresle, France). Red5 (IL5-tdtomato-cre), 'Great' (IFN-gamma reporter) and BALB/c CD45.1^{+} mice were from Jackson Laboratories (030926-017580-006584) (Maine, United States). C57BL/6 Rora$^{fl/sg}$ Il7r^{Cre} were provided by A. McKenzie (Cambridge, UK) and H. Rodewald (Heidelberg, Ger) and C57BL/6 IFN-γR$^{-/-}$ by E. Muraille (ULB). C57BL/6 CD45.1.2^{+} and CD45.1^{+} were bred in the GIGA animal facility (ULiege, Belgium). Except where otherwise stated, all mice used were 8-12 weeks of age. Animals were housed in the University of Liege.

Viruses.

The WT MHV-68 strain of MuHV-4 (*83*) and the latency-deficient mutant (MuHV-4 Del73) (*47*) were grown on BHK (baby hamster kidney) cells and were purified and titrated as described (*84*).

Mouse infection.

Intranasal or intratracheal infection was performed under isoflurane anesthesia, with 1×10^4 MuHV-4 PFU in 50 µl of PBS .

Administration of HDM extracts.

Anesthetized mice received intranasal instillation of PBS or HDM in 50 µL. To induce airway allergy, two different protocols were used. In the high-dose protocol, mice were treated with 100 µg HDM extracts on day 0 and were subsequently challenged with 100 µg HDM on days 7 and 14. In the HDM low-dose protocol, mice were sensitized with 10 µg HDM on day 0 and were subsequently challenged with 10 µg HDM on days 7 to 8 or on days 7 to 11. In both models, analyses were performed 3 days after the final HDM administration. As BALB/c and C57BL6 mice strains exhibit different sensitivities to HDM-induced airway allergy, the HDM high-dose model was used in BALB/c mice only while the HDM low-dose model was used in both genetic backgrounds. To assess the early innate response to HDM, mice were sensitized with 10 or 100 µg HDM and were euthanized after one day.

Immunofluorescence microscopy.

After euthanasia, 1 mL of 2% PFA were injected intratracheally and lungs were perfused through the right ventricle with 5 mL of 2% PFA. Tissues were harvested and fixed for 2 h in 2% PFA, washed for 4 h with PBS, cryoprotected overnight with 30% of sucrose, and embedded in OCT (Scigen) prior to freezing. Sections were processed on a Leica CM 3050S cryomicrotome (7-10 µm), dried on slides for 30 min, and kept at -80°C until staining. Tissues were blocked with 3% goat serum and 2% BSA and maintained in PBS + 0.2% triton X100 throughout antibody treatments. For multispectral analyses, endogenous biotin-blocking kit was used (ThermoFisher) before. Primary antibodies (rabbit IgG anti-dsRed (Takara, 1:200), rat IgG2b anti-CD3 (17A2, Biolegend, 1:100), rat IgG2a anti-CD68 (FA-11, Invitrogen, 1:100)) were incubated for 4h at 4°C and secondary antibodies (1:500 or 1:1000 dilution, conjugated to AF488, AF555, AF594, AF647 or biotin (ThermoFisher)) for 45 min at RT followed, when necessary, by secondary streptavidin (Brilliant Violet 421 Streptavidin (BioLegend, 1:700)) for 30 min at RT and primary antibodies (hamster IgG anti-CD11c AF488 conjugated (ThermoFisher, 1:200) and rat IgG2bkappa anti-CD11b eF660 conjugated (ThermoFisher, 1:100)) overnight. Slides were mounted with ProLong™ Gold or Diamond Antifade (ThermoFisher) with DAPI (BioLegend). Samples were rinsed 3 times in PBS between each steps. Slides were examined with a Nikon A1R confocal microscope or, for multispectral analysis with a Zeiss LSM980 inverted confocal microscope using a Plan-Apochromat 20x/0.8 or a LD C-Apochromat 40x/1.1 W objective. All fluorophores were excited simultaneously at 405/488/561/639 nm using main beam splitters at 405, 488, 561, 639 nm. The emission spectra were collected with a spectral detector 32 channels GaAsP Photomultiplier tube (PMT) in lambda mode at 8.8 nm bins from 411 to 694 nm. Then we perform a spectral unmixing process based on the monostaining spectra. Analysis was performed with ImageJ software for image calculator or IMARIS (Bitplane) software for the spatial colocalisation.

BAL, cytology and cytokine measurement.

After euthanasia, trachea was catheterized and BAL was performed by two consecutive flushes of the lungs with 1 mL of ice-cold PBS containing protease inhibitors (Complete, Roche). Cell density was evaluated using a hemocytometer after staining with Tuerk solution (Sigma-Aldrich). Cytokine production was measured by specific ELISA (Ready-SET-Go, eBioscience).

Cell suspension preparation from organs.

To harvest lung cells, mice were perfused with ice-cold PBS through the right ventricle. Then, lung lobes were collected into a C-Tube (Miltenyi) containing complete RPMI medium, 50 µg/mL liberase TM (Roche) and 100 µg/mL DNase I (Roche), before being processed with a gentleMACS dissociator (Miltenyi) and, finally incubated for 30 min at 37 °C. For ECs sorting, lung were previously digested 10 min at RT in DMEM medium with 10 U/mL of Dispase (Sigma-Aldrich) before C-Tube process. BM cells were obtained from adult mice by crushing the femurs and tibiae. Blood was acquired by cardiac puncture and was immediately suspended in ice-cold PBS complemented with 5 mM EDTA. Suspensions of cells were finally washed and treated for lysis of erythrocytes (1X RBC Lysis Buffer, ThermoFisher). For all preparations, cells were finally strained through a 70-µm filter.

Flow cytometry.

For intracellular staining, single-cell suspensions were stimulated for 4 h at 37°C in RPMI with 50 ng/mL phorbol 12-myristate 13-acetate (Sigma-Aldrich), 1 µg/mL ionomycin (Sigma-Aldrich), 8 mg/mL monensin and brefeldin (BD Biosciences) and 2 mM β-mercaptoethanol (Sigma-Aldrich).

Cells were firstly blocked with anti-FcR antibody (CD16/32, Biolegend) during 20 min. Labeling of single-cell suspensions was performed on ice in PBS containing 0.5% BSA and 0,1% Sodium azide with various panels of fluorochrome-conjugated antibodies for 30min. Antibodies to B220/CD45R (clone RA3-6B2, APC), CD11b (clone M1/70, BV605 and FITC), CD11c (clone N418, APC), CD19 (clone 6D5, APC/Cyanine7), CD25 (clone PC61, Alexa Fluor 700), CD274 (clone 10F.9G2, BV711 and APC), CD279 (clone 29F.1A12, APC/Fire750), CD3e (clone 145-2C11, APC, BV421 and FITC), CD4 (clones RM 4-5 GK1.5, APC and FITC), CD45 (clone 30-F11, BV510 and PE/Cyanine7), CD45.1 (clone A20, BV421 and APC), CD45.2 (clone 104, BV510 and PE/Cyanine7), CD49b (clone DX5, APC), CD5 (clone 53-7.3, APC), CD86 (clone GL-1, APC/Cyanine7), CD8α (clone 53-6.7, APC and PerCP/Cyanine5.5), CD90.2 (53-2.1, BV421), F4/80 (clone BM8, APC), FCεRIα (clone MAR-1, APC), Gr-1 (clone RB6-8C5, APC), I-A/I-E (clone M5/114.15.2, FITC and PE/Cyanine7), IFN-γ (clone XMG1.2, BV711), IL-5 (clone TRFK5, BV421 and PE), Ki-67 (clone 16A8, Alexa Fluor 488 and PE), KLRG1 (clone 2F1, BV711), Ly6A/E (clone D7, FITC), Ly6C (clone HK1.4, BV785), Siglec-F (clone E50-2440, APC) and ST2 (clone DIH9, BV421 and PE) all from Biolegend; antibodies to CD11b (clone M1/70, BV711), CD3e (clone 145-2C11, APC-Cy7), CD90.2 (clone 53-2.1, BV711), KLRG1 (clone 2F1, BV786), Ly6G (clone 1A8, APC-Cy7), Siglec-F (clone E50-2440, PE and PE-CF594), Streptavidin (APC) all from BD Biosciences; antibodies to Arginase 1 (clone AexF, PE-Cyanine7), CD11c (clone N418, Alexa Fluor 700), GATA-3 (clone TWAJ, PE), IL-13 (clone eBio13A, Alexa Fluor 488), iNOS (clone CXNFT, PE), Ly6C (clone HK1.4, PE), NK1.1 (clone PK136, PE-Cyanine7), RELM alpha (clone DS8RELM, PE), T-bet (clone eBio4B10, PE) and Streptavidin (FITC) all from ThermoFisher and antibody to YM1/Chitinase 3-like 3 (Biotinylated) from R&D Systems. The gating strategy to identify the different cell populations included successive forward- and side-scatter gating, exclusion of multiplets and selection of living cells with the viability marker Zombie Aqua™ or Violet™ (Biolegend) or Fixable Viability Dye eFluor™ 780 (eBioscience). Annexin V FITC and 7-AAD were purchased from Biolegend and apoptosis/necrosis assays were performed according to manufacturer's instructions. The Foxp3 Transcription Factor Staining kit was purchased from eBioscience and used for intranuclear staining. Samples were processed on a BD LSR Fortessa X-20 equipped with 50-mW violet 405-nm, 50-mW blue 488-nm, 50-mW yellow-green 561-nm and 40-mW red 633-nm lasers and an ND1.0 filter in front of the FSC photodiode.

Cytokine treatment.

Recombinant murine IL-13 (Biolegend) was administered intratracheally (1 µg into 50µL) from day 8 post-infection for 5 days and analysis was performed one day after the last instillation.

Real-time quantitative PCR.

Lung tissue were homogenized in TRIzol (ThermoFisher) and RNA extracted using RNeasy Mini Kit (Qiagen). RNA was reverse transcribed using iScript™ cDNA Synthesis Kit (Bio-Rad) and real-time qPCR was performed using SYBR Green IQ supermix (Bio-Rad) and primers detailed in Table S1. The comparative ΔCt method was used to represent relative expression normalized to the housekeeping gene glyceraldehyde 3-phosphate dehydrogenase (GAPDH).

Generation of BM chimeras.

BM chimeras were constructed by exposure of BALB/c CD45.2$^+$ or C57BL/6 CD45.1.2$^+$ mice to a lethal irradiation protocol (see below) that preserves or not the thoracic cavity. These recipient mice were then given intravenous injection of 5×10^6 BM cells isolated from the femur and tibia

of BALB/c CD45.1$^+$ WT or a mix (1:1) of C57BL/6 CD45.1$^+$ WT and C57BL/6 IFN-γR$^{-/-}$ CD45.2$^+$ congenic BM cells. The host mice were given broad-spectrum antibiotics (endotrim, Ecuphar, 1.5 mg/ml), for 4 weeks in drinking water. Experimental manipulations on chimeric mice were allowed 8 weeks after the BM transplantation.

Mouse irradiation.

A dose of 6 Gy was delivered to the whole body and 7,5 Gy when the thoracic cavity was spared with a dedicated small animal radiotherapy device (SmART Irradiator from Precision X-Ray Inc). Radiation was delivered using a photon beam (maximum energy of 225 kV and 13 mA), which provided a dose rate of 3 Gy/min. The planning system SmART-plan (version 1.3.9 Precision X-ray, North Branford, CT) was used to establish and deliver the treatment. To target the whole body except the thoracic cavity, we used two opposite beams to irradiate the head and the same schedule to irradiate the abdominal cavity. The dose delivered was almost 0 Gy to the lungs, 7.5 Gy to the soft tissue and 20.5 Gy to the bones. Fluoroscopy was used to check mouse positioning before each beam to avoid thoracic irradiation. During irradiation, mice received continuous isoflurane anesthesia.

AM isolation and transfer.

AMs were purified by positive CD11c MACS selection (Miltenyi Biotech) from BALF of mock- or MuHV-4-infected mice (C57BL/6) 30 days after infection. AM purity was checked by flow cytometry (autofluorescent CD11c$^+$ living cells) and was confirmed to be >95%. For transfer experiments, 8×10^5 AMs in 75 µl of PBS were injected intranasally into naive CD45.1$^+$ congenic C57BL/6 mice under isoflurane anesthesia.

Cell sorting of ILC2s, ILCs, AMs, Mos and ECs.

Lung ILC2s (defined as Lin$^-$CD45$^+$CD127$^+$CD90.2$^+$ST2$^+$CD25$^+$ living cells) were sorted after negative enrichment against lineage markers (B220, CD11c, CD3, CD4, CD49b, CD5, CD8α, F4/80, FcεR1, Gr1 and Siglec-F) using MojoSort™ Mouse anti-APC Nanobeads (Biolegend) and magnetic separation using LD columns (Miltenyi). Lung ILCs (defined as Lin$^-$CD45$^+$CD90.2$^+$ living cells) were sorted after negative enrichment against lineage markers (B220, CD11c, CD3, CD4, CD5, CD8α, F4/80, FcεR1, Ly6G and Siglec-F) using MojoSort™ Mouse anti-APC Nanobeads and magnetic separation using LD columns (Miltenyi). AMs from BALF were defined as autofluorescent, FSC-A^{high} living cells. Lung ECs were sorted (CD45-CD31-Epcam+ live cells) after depletion of CD45+ cells using using MojoSort™ Mouse anti-CD45 Nanobeads (Biolegend). BM Mos were sorted (CD19-CD3-CD11b+Ly6C+ living cells), after depletion of Ly6G+ and B220+ cells using MojoSort™ Mouse anti-APC Nanobeads (Biolegend) and magnetic separation using LD columns (Miltenyi). All cells were sorted on a FACSAria IIIu (BD Biosciences).

***Ex vivo* culture.**

50,000 BM Mos and 5,000 lung ECs were co-cultured in 200 µL of RPMI 1640 medium containing Glutamax-I with 10% FCS, 1% MEM, 50 µM 2-mercaptoethanol, 100 U/ml penicillin, 100 mg/ml streptomycin and 10 ng/ml recombinant murine GM-CSF (Peprotech). Directly or 3 days after the start of the co-culture, 2,500 ILC2s from mock- or MuHV-4 infected C57BL/6 mice (sorted as described above) were added with IL-2 (final concentration 10 ng/mL) and anti-mouse GM-CSF (BE0259, BioXcell, 15 µg/mL) when specified. Cells were analyzed 3 days after the addition of ILC2s and supernatant was used for analyzing cytokine levels.

Bulk RNA sequencing.

From *ex vivo* co-culture, cells were harvested using Cell Dissociation Buffer (ThermoFisher) for 15 min in 37°C and then macrophages (FSC-A^{high}, $CD11c^{+}$ living cells) were sorted and kept in TRIzol at -80°C. RNA from macrophages was extracted using the RNeasy Mini kit (Qiagen), and quality was assessed on Agilent RNA 6000 Pico. cDNA was prepared using SmartSeq HT (1ng). RNA-Seq libraries were prepared using the Illumina Nextera XT DNA Library Preparation Kit. Libraries were quantified and normalized by qPCR. Libraries were finally sequenced using Illumina NovaSeq6000 and bioinformatics analysis was performed. Approximately 25×10^6 75-base single-end reads were generated per sample. Subsequent analysis used R bioconductor (v.4.0.3). The nf-core/rnaseq pipeline (v.3.0) was used to generate the QC of the raw data and the count matrix (*85*). The DESeq2 package was used to process the count matrix in order to get differentially expressed genes (*86*). The vsn package was used to generate a variance stabilizing transformation out of the count matrix for visualization and clustering (*87*). List of DE genes between were uploaded on PANTHER and GO biological process complete was selected. The results with a FDR ≤ 0.05 were considered as significant.

Single cell RNA sequencing.

Libraries preparations for single-cell immune profiling, sequencing, and post-processing of the raw data were performed at the GIGA-Genomics Core Facility (Belgium). Sorted cells were washed with PBS (calcium and magnesium free) containing BSA (400 µg/mL). 12,800 cells were loaded on Chromium Controller (10x Genomics). Samples were further processed for droplet-based RNA sequencing and libraries were prepared using Chromium Single Cell 3' Reagent Kits v3 (10x Genomics). Amplified cDNA quality controls were performed with an Agilent bioanalyzer (Agilent) and final library profile were checked on Qiaxcel (Qiagen). Sequencing libraries were loaded an Illumina Novaseq sequencer with NovaSeq SP 100 v1 kit (Illumina, CA, USA) using the following read lengths: 28 bp for Read1 (18 bp Barcode + 10 bp Randomer), 8 bp for Sample Index and 88 bp for Read2. Library quantification was processed with KAPA Library quantification kit (KAPA Biosystems). Analysis of scRNA-seq samples is described in supplementary Material and Methods.

Quantification and statistical analysis.

Statistical tests are described in the figure legends. Data were analyzed using Prism software (GraphPad10, San Diego, CA). For RNA or scRNA sequencing data, statistical analyses were performed in R v.4.0.3 and various Bioconductor packages. No statistical methods were used to predetermine sample size prior to experiments.

References

1. C. Abbafati, K. M. M. Abbas, M. Abbasi-Kangevari, F. Abd-Allah, A. Abdelalim, M. Abdollahi, I. Abdollahpour, K. H. H. Abegaz, H. Abolhassani, V. Aboyans, L. G. G. Abreu, M. R. M. R. M. Abrigo, A. Abualhasan, L. J. J. Abu-Raddad, A. I. I. Abushouk, M. Adabi, V. Adekanmbi, A. M. M. Adeoye, O. O. O. Adetokunboh, D. Adham, S. M. M. Advani, A. Afshin, G. Agarwal, S. M. K. M. K. Aghamir, A. Agrawal, T. Ahmad, K. Ahmadi, M. Ahmadi, H. Ahmadieh, M. B. B. Ahmed, T. Y. Y. Akalu, R. O. O. Akinyemi, T. Akinyemiju, B. Akombi, C. J. J. Akunna, F. Alahdab, Z. Al-Aly, K. Alam, S. Alam, T. Alam, F. M. M. Alanezi, T. M. M. Alanzi, B. W. W. Alemu, K. F. F. Alhabib, M. Ali, S. Ali, G. Alicandro, C. Alinia, V. Alipour, H. Alizade, S. M. M. Aljunid, F. Alla, P. Allebeck, A. Almasi-Hashiani, H. M. M. Al-Mekhlafi, J. Alonso, K. A. A. Altirkawi, M. Amini-Rarani, F. Amiri, D. A. A. Amugsi, R. Ancuceanu, D. Anderlini, J. A. A. Anderson, C. L. L. Andrei, T. Andrei, C. Angus, M. Anjomshoa, F. Ansari, A. Ansari-Moghaddam, I. C. C. Antonazzo, C. A. T. A. T. Antonio, C. M. M. Antony, E. Antriyandarti, D. Anvari, R. Anwer, S. C. Y. C. Y. Appiah, J. Arabloo, M. Arab-Zozani, A. Y. Y. Aravkin, F. Ariani, B. Armoon, J. Ärnlöv, A. Arzani, M. Asadi-Aliabadi, A. A. A. Asadi-Pooya, C. Ashbaugh, M. Assmus, Z. Atafar, D. D. D. Atnafu, M. M. d. W. M. d. W. Atout, F. Ausloos, M. Ausloos, B. P. P. Ayala Quintanilla, G. Ayano, M. A. A. Ayanore, S. Azari, G. Azarian, Z. N. N. Azene, A. Badawi, A. D. D. Badiye, M. A. A. Bahrami, M. H. H. Bakhshaei, A. Bakhtiari, S. M. M. Bakkannavar, A. Baldasseroni, K. Ball, S. H. H. Ballew, D. Balzi, M. Banach, S. K. K. Banerjee, A. B. B. Bante, A. G. G. Baraki, S. L. L. Barker-Collo, T. W. W. Bärnighausen, L. H. H. Barrero, C. M. M. Barthelemy, L. Barua, S. Basu, B. T. T. Baune, M. Bayati, J. S. S. Becker, N. Bedi, E. Beghi, Y. Béjot, M. L. L. Bell, F. B. B. Bennitt, I. M. M. Bensenor, K. Berhe, A. E. E. Berman, A. S. S. Bhagavathula, R. Bhageerathy, N. Bhala, D. Bhandari, K. Bhattacharyya, Z. A. A. Bhutta, A. Bijani, B. Bikbov, M. S. S. Bin Sayeed, A. Biondi, B. M. M. Birihane, C. Bisignano, R. K. K. Biswas, H. Bitew, S. Bohlouli, M. Bohluli, A. S. S. Boon-Dooley, G. Borges, A. M. M. Borzì, S. Borzouei, C. Bosetti, S. Boufous, D. Braithwaite, M. Brauer, N. J. K. J. K. Breitborde, S. Breitner, H. Brenner, P. S. S. Briant, A. N. N. Briko, N. I. I. Briko, G. B. B. Britton, D. Bryazka, B. R. R. Bumgarner, K. Burkart, R. T. T. Burnett, S. Burugina Nagaraja, Z. A. A. Butt, F. L. L. Caetano Dos Santos, L. E. E. Cahill, L. A. A. Cámera, I. R. R. Campos-Nonato, R. Cárdenas, G. Carreras, J. J. J. Carrero, F. Carvalho, J. M. M. Castaldelli-Maia, C. A. A. Castañeda-Orjuela, G. Castelpietra, F. Castro, K. Causey, C. R. R. Cederroth, K. M. M. Cercy, E. Cerin, J. S. S. Chandan, K. L. L. Chang, F. J. J. Charlson, V. K. K. Chattu, S. Chaturvedi, N. Cherbuin, O. Chimed-Ochir, D. Y. Y. Cho, J. Y. J. Y. J. Choi, H. Christensen, D. T. T. Chu, M. T. T. Chung, S. C. C. Chung, F. M. M. Cicuttini, L. G. G. Ciobanu, M. Cirillo, T. K. D. K. D. Classen, A. J. J. Cohen, K. Compton, O. R. R. Cooper, V. M. M. Costa, E. Cousin, R. G. G. Cowden, D. H. H. Cross, J. A. A. Cruz, S. M. A. M. A. Dahlawi, A. A. M. A. M. Damasceno, G. Damiani, L. Dandona, R. Dandona, W. J. J. Dangel, A. K. K. Danielsson, P. I. I. Dargan, A. M. M. Darwesh, A. Daryani, J. K. K. Das, R. Das Gupta, J. das Neves, C. A. A. Dávila-Cervantes, D. V. V. Davitoiu, D. De Leo, L. Degenhardt, M. DeLang, R. P. P. Dellavalle, F. M. M. Demeke, G. T. T. Demoz, D. G. G. Demsie, E. Denova-Gutiérrez, N. Dervenis, G. P. P. Dhungana, M. Dianatinasab, D. Dias da Silva, D. Diaz, Z. S. S. Dibaji Forooshani, S. Djalalinia, H. T. T. Do, K. Dokova, F. Dorostkar, L.

Doshmangir, T. R. R. Driscoll, B. B. B. Duncan, A. R. R. Duraes, A. W. W. Eagan, D. Edvardsson, N. El Nahas, I. El Sayed, M. El Tantawi, I. Elbarazi, I. Y. Y. Elgendy, S. I. I. El-Jaafary, I. R. F. R. F. Elyazar, S. Emmons-Bell, H. E. E. Erskine, S. Eskandarieh, S. Esmaeilnejad, A. Esteghamati, K. Estep, A. Etemadi, A. E. E. Etisso, J. Fanzo, M. Farahmand, M. Fareed, R. Faridnia, A. Farioli, A. Faro, M. Faruque, F. Farzadfar, N. Fattahi, M. Fazlzadeh, V. L. L. Feigin, R. Feldman, S. M. M. Fereshtehnejad, E. Fernandes, G. Ferrara, A. J. J. Ferrari, M. L. L. Ferreira, I. Filip, F. Fischer, J. L. L. Fisher, L. S. S. Flor, N. A. A. Foigt, M. O. O. Folayan, A. A. A. Fomenkov, L. M. M. Force, M. Foroutan, R. C. C. Franklin, M. Freitas, W. Fu, T. Fukumoto, J. M. M. Furtado, M. M. M. Gad, E. Gakidou, S. Gallus, A. L. L. Garcia-Basteiro, W. M. M. Gardner, B. S. S. Geberemariyam, A. A. A. A. A. Ayalew Gebreslassie, A. Geremew, A. Gershberg Hayoon, P. W. W. Gething, M. Ghadimi, K. Ghadiri, F. Ghaffarifar, M. Ghafourifard, F. Ghamari, A. Ghashghaee, H. Ghiasvand, N. Ghith, A. Gholamian, R. Ghosh, P. S. S. Gill, T. G. G. Ginindza, G. Giussani, E. V. V. Gnedovskaya, S. Goharinezhad, S. V. V. Gopalani, G. Gorini, H. Goudarzi, A. C. C. Goulart, F. Greaves, M. Grivna, G. Grosso, M. I. M. I. M. Gubari, H. C. C. Gugnani, R. A. A. Guimarães, R. A. A. Guled, G. Guo, Y. Guo, R. Gupta, T. Gupta, B. Haddock, N. Hafezi-Nejad, A. Hafiz, A. A. Haj-Mirzaian, A. A. Haj-Mirzaian, B. J. J. Hall, I. Halvaei, R. R. R. Hamadeh, S. Hamidi, M. S. S. Hammer, G. J. J. Hankey, H. Haririan, J. M. M. Haro, A. I. I. Hasaballah, M. M. M. Hasan, E. Hasanpoor, A. Hashi, S. Hassanipour, H. Hassankhani, R. J. J. Havmoeller, S. I. I. Hay, K. Hayat, G. Heidari, R. Heidari-Soureshjani, H. J. J. Henrikson, M. E. E. Herbert, C. Herteliu, F. Heydarpour, T. R. R. Hird, H. W. W. Hoek, R. Holla, P. Hoogar, H. D. D. Hosgood, N. Hossain, M. Hosseini, M. Hosseinzadeh, M. Hostiuc, S. Hostiuc, M. Househ, M. Hsairi, V. C. R. C. R. Hsieh, G. Hu, K. Hu, T. M. M. Huda, A. Humayun, C. K. K. Huynh, B. F. F. Hwang, V. C. C. Iannucci, S. E. E. Ibitoye, N. Ikeda, K. S. S. Ikuta, O. S. S. Ilesanmi, I. M. M. Ilic, M. D. D. Ilic, L. R. R. Inbaraj, H. Ippolito, U. Iqbal, S. S. N. S. N. Irvani, C. M. S. M. S. Irvine, M. M. M. Islam, S. M. S. M. S. Islam, H. Iso, R. Q. Q. Ivers, C. J. C. C. D. C. D. C. J. Iwu, C. J. C. C. D. C. D. C. J. Iwu, I. O. O. Iyamu, J. Jaafari, K. H. H. Jacobsen, H. Jafari, M. Jafarinia, M. A. A. Jahani, M. Jakovljevic, F. Jalilian, S. L. L. James, H. Janjani, T. Javaheri, J. Javidnia, P. Jeemon, E. Jenabi, R. P. P. Jha, V. Jha, J. S. S. Ji, L. Johansson, O. John, Y. O. O. John-Akinola, C. O. O. Johnson, J. B. B. Jonas, F. Joukar, J. J. J. Jozwiak, M. Jürisson, A. Kabir, Z. Kabir, H. Kalani, R. Kalani, L. R. R. Kalankesh, R. Kalhor, T. Kanchan, N. Kapoor, B. K. K. Matin, A. Karch, M. A. A. Karim, G. M. M. Kassa, S. V. V. Katikireddi, G. A. A. Kayode, A. Kazemi Karyani, P. N. N. Keiyoro, C. Keller, L. Kemmer, P. J. J. Kendrick, N. Khalid, M. Khammarnia, E. A. A. Khan, M. Khan, K. Khatab, M. M. M. Khater, M. N. N. Khatib, M. Khayamzadeh, S. Khazaei, C. Kieling, Y. J. J. Kim, R. W. W. Kimokoti, A. Kisa, S. Kisa, M. Kivimäki, L. D. D. Knibbs, A. K. S. K. S. Knudsen, J. M. M. Kocarnik, S. Kochhar, J. A. A. Kopec, V. A. A. Korshunov, P. A. A. Koul, A. Koyanagi, M. U. G. U. G. Kraemer, K. Krishan, K. J. J. Krohn, H. Kromhout, B. Kuate Defo, G. A. A. Kumar, V. Kumar, O. P. P. Kurmi, D. Kusuma, C. La Vecchia, B. Lacey, D. K. K. Lal, R. Lalloo, T. Lallukka, F. H. H. Lami, I. Landires, J. J. J. Lang, S. M. M. Langan, A. O. O. Larsson, S. Lasrado, P. Lauriola, J. V. V. Lazarus, P. H. H. Lee, S. W. H. W. H. Lee, K. E. E. Legrand, J. Leigh, M. Leonardi, H. Lescinsky, J. Leung, M. Levi, S. Li, L. L. L. Lim, S. Linn, S. S. Liu, S. S. Liu, Y. Liu, J. Lo, A. D. D. Lopez, J. C. F. C. F. Lopez, P. D. D. Lopukhov, S. Lorkowski, P. A. A. Lotufo, A. Lu, A. Lugo, E. R. R. Maddison, P. W. W. Mahasha, M.

M. M. Mahdavi, M. Mahmoudi, A. Majeed, A. Maleki, S. Maleki, R. Malekzadeh, D. C. C. Malta, A. A. A. Mamun, A. L. L. Manda, H. Manguerra, F. Mansour-Ghanaei, B. Mansouri, M. A. A. Mansournia, A. M. M. Mantilla Herrera, J. C. C. Maravilla, A. Marks, R. V. V. Martin, S. Martini, F. R. R. Martins-Melo, A. Masaka, S. Z. Z. Masoumi, M. R. R. Mathur, K. Matsushita, P. K. K. Maulik, C. McAlinden, J. J. J. McGrath, M. McKee, M. M. M. Mehndiratta, F. Mehri, K. M. M. Mehta, Z. A. A. Memish, W. Mendoza, R. G. G. Menezes, E. W. W. Mengesha, A. Mereke, S. T. T. Mereta, A. Meretoja, T. J. J. Meretoja, T. Mestrovic, B. Miazgowski, T. Miazgowski, I. M. M. Michalek, T. R. R. Miller, E. J. J. Mills, G. K. K. Mini, M. Miri, A. Mirica, E. M. M. Mirrakhimov, H. Mirzaei, M. Mirzaei, R. Mirzaei, M. Mirzaei-Alavijeh, A. T. T. Misganaw, P. Mithra, B. Moazen, D. K. K. Mohammad, Y. Mohammad, N. Mohammad Gholi Mezerji, A. Mohammadian-Hafshejani, N. Mohammadifard, R. Mohammadpourhodki, A. S. S. Mohammed, H. Mohammed, J. A. A. Mohammed, S. Mohammed, A. H. H. Mokdad, M. Molokhia, L. Monasta, M. D. D. Mooney, G. Moradi, M. Moradi, M. Moradi-Lakeh, R. Moradzadeh, P. Moraga, L. Morawska, J. Morgado-Da-Costa, S. D. D. Morrison, A. Mosapour, J. F. F. Mosser, S. Mouodi, S. M. M. Mousavi, A. M. M. Khaneghah, U. O. O. Mueller, S. Mukhopadhyay, E. C. C. Mullany, K. I. I. Musa, S. Muthupandian, A. F. F. Nabhan, M. Naderi, A. J. J. Nagarajan, G. Nagel, M. Naghavi, B. Naghshtabrizi, M. D. D. Naimzada, F. Najafi, V. Nangia, J. R. R. Nansseu, M. Naserbakht, V. C. C. Nayak, I. Negoi, J. W. W. Ngunjiri, C. T. T. Nguyen, H. L. T. L. T. Nguyen, M. Nguyen, Y. T. T. Nigatu, R. Nikbakhsh, M. R. R. Nixon, C. A. A. Nnaji, S. Nomura, B. Norrving, J. J. J. Noubiap, C. Nowak, V. Nunez-Samudio, B. Oancea, C. M. M. Odell, F. A. A. Ogbo, I. H. H. Oh, E. W. W. Okunga, M. Oladnabi, A. T. T. Olagunju, B. O. O. Olusanya, J. O. O. Olusanya, M. O. O. Omer, K. L. L. Ong, O. E. E. Onwujekwe, H. M. M. Orpana, A. Ortiz, O. Osarenotor, F. B. B. Osei, S. M. M. Ostroff, A. Otoiu, N. Otstavnov, S. S. S. Otstavnov, S. Øverland, M. O. O. Owolabi, P. A. A. Mahesh, J. R. R. Padubidri, R. Palladino, S. Panda-Jonas, A. Pandey, C. D. H. D. H. Parry, M. Pasovic, D. K. K. Pasupula, S. K. K. Patel, M. Pathak, S. B. B. Patten, G. C. C. Patton, H. P. P. Toroudi, A. E. E. Peden, A. Pennini, V. C. F. C. F. Pepito, E. K. K. Peprah, D. M. M. Pereira, K. Pesudovs, H. Q. Q. Pham, M. R. R. Phillips, C. Piccinelli, T. M. M. Pilz, M. A. A. Piradov, M. Pirsaheb, D. Plass, S. Polinder, K. R. R. Polkinghorne, C. D. D. Pond, M. J. J. Postma, H. Pourjafar, F. Pourmalek, A. Poznañska, S. I. I. Prada, V. Prakash, D. R. A. R. A. Pribadi, E. Pupillo, Z. Q. Q. Syed, M. Rabiee, N. Rabiee, A. Radfar, A. Rafiee, A. Raggi, M. A. A. Rahman, A. Rajabpour-Sanati, F. Rajati, I. Rakovac, P. Ram, K. Ramezanzadeh, C. L. L. Ranabhat, P. C. C. Rao, S. J. J. Rao, V. Rashedi, P. Rathi, D. L. L. Rawaf, S. Rawaf, L. Rawal, R. Rawassizadeh, R. Rawat, C. Razo, S. B. B. Redford, R. C. C. Reiner, M. B. B. Reitsma, G. Remuzzi, V. Renjith, A. M. N. M. N. Renzaho, S. Resnikoff, N. N. Rezaei, N. N. Rezaei, A. Rezapour, P. A. A. Rhinehart, S. M. M. Riahi, D. C. D. C. Ribeiro, D. C. D. C. Ribeiro, J. Rickard, J. A. A. Rivera, N. L. S. L. S. Roberts, S. Rodríguez-Ramírez, L. Roever, L. Ronfani, R. Room, G. Roshandel, G. A. A. Roth, D. Rothenbacher, E. Rubagotti, G. M. M. Rwegerera, S. Sabour, P. S. S. Sachdev, B. Saddik, E. Sadeghi, M. Sadeghi, R. Saeedi, S. Saeedi Moghaddam, Y. Safari, S. Safi, S. Safiri, R. Sagar, A. Sahebkar, S. M. M. Sajadi, N. Salam, P. Salamati, H. Salem, M. R. R. Salem, H. Salimzadeh, O. M. M. Salman, J. A. A. Salomon, Z. Samad, H. Samadi Kafil, E. Z. Z. Sambala, A. M. M. Samy, J. Sanabria, T. G. G. Sánchez-Pimienta, D. F. F. Santomauro, I. S. S. Santos, J. V. V. Santos, M. M. M. Santric-Milicevic, S. Y. I. Y. I.

Saraswathy, R. Sarmiento-Suárez, N. Sarrafzadegan, B. Sartorius, A. Sarveazad, B. Sathian, T. Sathish, D. Sattin, S. Saxena, L. E. E. Schaeffer, S. Schiavolin, M. P. P. Schlaich, M. I. I. Schmidt, A. E. E. Schutte, D. C. C. Schwebel, F. Schwendicke, A. M. M. Senbeta, S. Senthilkumaran, S. G. G. Sepanlou, B. Serdar, M. L. L. Serre, J. Shadid, O. Shafaat, S. Shahabi, A. A. A. Shaheen, M. A. A. Shaikh, A. S. S. Shalash, M. Shams-Beyranvand, M. Shamsizadeh, K. Sharafi, A. Sheikh, A. Sheikhtaheri, K. Shibuya, K. D. D. Shield, M. Shigematsu, J. I. Il Shin, M. J. J. Shin, R. Shiri, R. Shirkoohi, K. Shuval, S. Siabani, R. Sierpinski, I. D. D. Sigfusdottir, R. Sigurvinsdottir, J. P. P. Silva, K. E. E. Simpson, J. A. A. Singh, P. Singh, E. Skiadaresi, S. T. T. Skou, V. Y. Y. Skryabin, E. U. R. U. R. Smith, A. Soheili, S. Soltani, M. Soofi, R. J. D. J. D. Sorensen, J. B. B. Soriano, M. B. B. Sorrie, S. Soshnikov, I. N. N. Soyiri, C. N. N. Spencer, A. Spotin, C. T. T. Sreeramareddy, V. Srinivasan, J. D. D. Stanaway, C. Stein, D. J. J. Stein, C. Steiner, L. Stockfelt, M. A. A. Stokes, K. Straif, J. L. L. Stubbs, M. B. B. Sufiyan, H. A. R. A. R. Suleria, R. Suliankatchi Abdulkader, G. Sulo, I. Sultan, R. Tabarés-Seisdedos, K. M. M. Tabb, T. Tabuchi, A. Taherkhani, M. Tajdini, K. Takahashi, J. S. S. Takala, A. T. T. Tamiru, N. Taveira, A. Tehrani-Banihashemi, M. H. H. Temsah, G. A. A. Tesema, Z. T. T. Tessema, G. D. D. Thurston, M. V. V. Titova, H. R. R. Tohidinik, M. Tonelli, R. Topor-Madry, F. Topouzis, A. E. E. Torre, M. Touvier, M. R. R. Tovani-Palone, B. X. X. Tran, R. Travillian, A. Tsatsakis, L. T. T. Tudor Car, S. Tyrovolas, R. Uddin, C. D. D. Umeokonkwo, B. Unnikrishnan, E. Upadhyay, M. Vacante, P. R. R. Valdez, A. van Donkelaar, T. J. J. Vasankari, Y. Vasseghian, Y. Veisani, N. Venketasubramanian, F. S. S. Violante, V. Vlassov, S. E. E. Vollset, T. Vos, R. Vukovic, Y. Waheed, M. T. T. Wallin, Y. P. Y. Y. P. Wang, Y. P. Y. Y. P. Wang, A. Watson, J. Wei, M. Y. W. Y. W. Wei, R. G. G. Weintraub, J. Weiss, A. Werdecker, J. J. J. West, R. Westerman, J. L. L. Whisnant, H. A. A. Whiteford, K. E. E. Wiens, C. D. A. D. A. Wolfe, S. S. S. Wozniak, A. M. M. Wu, J. Wu, S. Wulf Hanson, G. Xu, R. Xu, S. Yadgir, S. H. H. Yahyazadeh Jabbari, K. Yamagishi, M. Yaminfirooz, Y. Yano, S. Yaya, V. Yazdi-Feyzabadi, T. Y. Y. Yeheyis, C. S. S. Yilgwan, M. T. T. Yilma, P. Yip, N. Yonemoto, M. Z. Z. Younis, T. P. P. Younker, B. Yousefi, Z. Yousefi, T. Yousefinezhadi, A. Y. Y. Yousuf, C. Yu, H. Yusefzadeh, T. Z. Z. Moghadam, M. Zamani, M. Zamanian, H. Zandian, M. S. S. Zastrozhin, Y. Zhang, Z. J. J. Zhang, J. T. T. Zhao, X. J. G. J. G. Zhao, Y. Zhao, P. Zheng, M. Zhou, K. Davletov, S. E. E. Karimi, S. Mondello, C. J. L. J. L. Murray, Global burden of 369 diseases and injuries in 204 countries and territories, 1990–2019: a systematic analysis for the Global Burden of Disease Study 2019. *Lancet*. **396**, 1204–1222 (2020).

2. H. Hammad, B. N. Lambrecht, The basic immunology of asthma. *Cell*. **184**, 2521–2522 (2021).
3. W. W. Busse, R. F. Lemanske Jr., J. E. Gern, Role of viral respiratory infections in asthma and asthma exacerbations. *Lancet*. **376**, 826–834 (2010).
4. T. Jartti, J. E. Gern, Role of viral infections in the development and exacerbation of asthma in children. *J. Allergy Clin. Immunol.* **140** (2017), pp. 895–906.
5. M. J. Schuijs, M. A. Willart, K. Vergote, D. Gras, K. Deswarte, M. J. Ege, F. B. Madeira, R. Beyaert, G. van Loo, F. Bracher, E. von Mutius, P. Chanez, B. N. Lambrecht, H. Hammad, Farm dust and endotoxin protect against allergy through A20 induction in lung epithelial cells. *Science (80-.).* **349**, 1106–1110 (2015).
6. B. N. Lambrecht, H. Hammad, The immunology of the allergy epidemic and the hygiene hypothesis. *Nat Immunol*. **in press**, 1076–1083 (2017).

7. E. Haspeslagh, I. Heyndrickx, H. Hammad, B. N. Lambrecht, The hygiene hypothesis: immunological mechanisms of airway tolerance. *Curr. Opin. Immunol.* **54**, 102–108 (2018).
8. S. Saghafian-Hedengren, E. Sverremark-Ekstrom, A. Linde, G. Lilja, C. Nilsson, Early-life EBV infection protects against persistent IgE sensitization. *J Allergy Clin Immunol*. **125**, 433–438 (2010).
9. B. Machiels, M. Dourcy, X. Xiao, J. Javaux, C. Mesnil, C. Sabatel, D. Desmecht, F. Lallemand, P. Martinive, H. Hammad, M. Guilliams, B. Dewals, A. Vanderplasschen, B. N. Lambrecht, F. Bureau, L. Gillet, A gammaherpesvirus provides protection against allergic asthma by inducing the replacement of resident alveolar macrophages with regulatory monocytes. *Nat. Immunol.* **18**, 1310–1320 (2017).
10. D. Artis, H. Spits, The biology of innate lymphoid cells. *Nature*. **517**, 293–301 (2015).
11. M. Colonna, Innate Lymphoid Cells: Diversity , Plasticity , and Unique Functions in Immunity. *Immunity*. **48**, 1104–1117 (2018).
12. M. E. Kotas, R. M. Locksley, Why Innate Lymphoid Cells? *Immunity*. **48**, 1081–1090 (2018).
13. B. C. Mindt, J. H. Fritz, C. U. Duerr, Group 2 innate lymphoid cells in pulmonary immunity and tissue homeostasis. *Front. Immunol.* **9**, 1–17 (2018).
14. D. R. Neill, S. H. Wong, A. Bellosi, R. J. Flynn, M. Daly, T. K. Langford, C. Bucks, C. M. Kane, P. G. Fallon, R. Pannell, H. E. Jolin, A. N. McKenzie, Nuocytes represent a new innate effector leukocyte that mediates type-2 immunity. *Nature*. **464**, 1367–1370 (2010).
15. B. Pulendran, D. Artis, New paradigms in type 2 immunity. *Science (80-.).* **337**, 431–435 (2012).
16. M. W. Dahlgren, A. B. Molofsky, All along the watchtower: group 2 innate lymphoid cells in allergic responses. *Curr. Opin. Immunol.* **54**, 13–19 (2018).
17. J. C. Nussbaum, S. J. Van Dyken, J. von Moltke, L. E. Cheng, A. Mohapatra, A. B. Molofsky, E. E. Thornton, M. F. Krummel, A. Chawla, H. E. Liang, R. M. Locksley, Type 2 innate lymphoid cells control eosinophil homeostasis. *Nature*. **502**, 245–248 (2013).
18. B. N. Lambrecht, H. Hammad, The immunology of asthma. *Nat Immunol*. **16**, 45–56 (2015).
19. H. Hammad, B. N. Lambrecht, Barrier Epithelial Cells and the Control of Type 2 Immunity. *Immunity*. **43**, 29–40 (2015).
20. T. Y. F. Halim, C. A. Steer, L. Matha, M. J. Gold, I. Martinez-Gonzalez, K. M. McNagny, A. N. J. McKenzie, F. Takei, L. Mathä, M. J. Gold, I. Martinez-Gonzalez, K. M. McNagny, A. N. J. McKenzie, F. Takei, L. Matha, M. J. Gold, I. Martinez-Gonzalez, K. M. McNagny, A. N. J. McKenzie, F. Takei, L. Mathä, M. J. Gold, I. Martinez-Gonzalez, K. M. McNagny, A. N. J. McKenzie, F. Takei, Group 2 innate lymphoid cells are critical for the initiation of adaptive T helper 2 cell-mediated allergic lung inflammation. *Immunity*. **40**, 425–435 (2014).
21. P. Licona-Limon, L. K. Kim, N. W. Palm, R. A. Flavell, TH2, allergy and group 2 innate lymphoid cells. *Nat Immunol*. **14**, 536–542 (2013).
22. C. A. Christianson, N. P. Goplen, I. Zafar, C. Irvin, J. T. Good Jr., D. R. Rollins, B. Gorentla, W. Liu, M. M. Gorska, H. Chu, R. J. Martin, R. Alam, Persistence of asthma requires multiple feedback circuits involving type 2 innate lymphoid cells and IL-33. *J Allergy Clin Immunol*. **136**, 59-68 e14 (2015).
23. M. J. Gold, F. Antignano, T. Y. F. Halim, J. A. Hirota, M. R. Blanchet, C. Zaph, F. Takei,

K. M. McNagny, Group 2 innate lymphoid cells facilitate sensitization to local, but not systemic, TH2-inducing allergen exposures. *J. Allergy Clin. Immunol.* **133**, 1142-1148.e5 (2014).

24. T. Y. F. Halim, Y. Y. Hwang, S. T. Scanlon, H. Zaghouani, N. Garbi, P. G. Fallon, A. N. J. McKenzie, Group 2 innate lymphoid cells license dendritic cells to potentiate memory TH2 cell responses. *Nat Immunol*. **17**, 57–64 (2016).
25. M. M. Fort, J. Cheung, D. Yen, J. Li, S. M. Zurawski, S. Lo, S. Menon, T. Clifford, B. Hunte, R. Lesley, T. Muchamuel, S. D. Hurst, G. Zurawski, M. W. Leach, D. M. Gorman, D. M. Rennick, IL-25 induces IL-4, IL-5, and IL-13 and Th2-associated pathologies in vivo. *Immunity*. **15**, 985–95 (2001).
26. T. Y. F. Halim, R. H. Krauss, A. C. Sun, F. Takei, Lung natural helper cells are a critical source of Th2 cell-type cytokines in protease allergen-induced airway inflammation. *Immunity*. **36**, 451–63 (2012).
27. C. S. N. Klose, T. Mahlakõiv, J. B. Moeller, L. C. Rankin, A. L. Flamar, H. Kabata, L. A. Monticelli, S. Moriyama, G. G. Putzel, N. Rakhilin, X. Shen, E. Kostenis, G. M. König, T. Senda, D. Carpenter, D. L. Farber, D. Artis, The neuropeptide neuromedin U stimulates innate lymphoid cells and type 2 inflammation. *Nature*. **549**, 282–286 (2017).
28. V. Cardoso, J. Chesné, H. Ribeiro, B. García-Cassani, T. Carvalho, T. Bouchery, K. Shah, N. L. Barbosa-Morais, N. Harris, H. Veiga-Fernandes, Neuronal regulation of type 2 innate lymphoid cells via neuromedin U. *Nature*. **549**, 277–281 (2017).
29. J. von Moltke, C. E. O'Leary, N. A. Barrett, Y. Kanaoka, K. F. Austen, R. M. Locksley, Leukotrienes provide an NFAT-dependent signal that synergizes with IL-33 to activate ILC2s. *J. Exp. Med.* **214**, 27–37 (2017).
30. P. Sui, D. L. Wiesner, J. Xu, Y. Zhang, J. Lee, S. Van Dyken, A. Lashua, C. Yu, B. S. Klein, R. M. Locksley, G. Deutsch, X. Sun, Pulmonary neuroendocrine cells amplify allergic asthma responses. *Science (80-.).* **360**, eaan8546 (2018).
31. W. Fonseca, N. W. Lukacs, S. Elesela, C. A. Malinczak, *Role of ILC2 in Viral-Induced Lung Pathogenesis* (Frontiers Media S.A., 2021; https://pubmed.ncbi.nlm.nih.gov/33953732/), vol. 12.
32. M. Killig, T. Glatzer, C. Romagnani, Recognition strategies of group 3 innate lymphoid cells. *Front. Immunol.* **5**, 1–8 (2014).
33. A. B. Molofsky, J. C. Nussbaum, H.-E. Liang, S. J. Van Dyken, L. E. Cheng, A. Mohapatra, A. Chawla, R. M. Locksley, Innate lymphoid type 2 cells sustain visceral adipose tissue eosinophils and alternatively activated macrophages. *J. Exp. Med.* **210**, 535–549 (2013).
34. P. Zeis, M. Lian, X. Fan, J. S. Herman, D. C. Hernandez, R. Gentek, S. Elias, C. Symowski, K. Knöpper, N. Peltokangas, C. Friedrich, R. Doucet-Ladeveze, A. M. Kabat, R. M. Locksley, D. Voehringer, M. Bajenoff, A. Y. Rudensky, C. Romagnani, D. Grün, G. Gasteiger, In Situ Maturation and Tissue Adaptation of Type 2 Innate Lymphoid Cell Progenitors. *Immunity*. **53**, 775-792.e9 (2020).
35. Y. Huang, K. Mao, X. Chen, M. Sun, T. Kawabe, W. Li, N. Usher, J. Zhu, J. F. Urban, W. E. Paul, R. N. Germain, S1P-dependent interorgan trafficking of group 2 innate lymphoid cells supports host defense. *Science (80-.).* **359**, 114–119 (2018).
36. S. M. Bal, J. H. Bernink, M. Nagasawa, J. Groot, M. M. Shikhagaie, K. Golebski, C. M. Van Drunen, R. Lutter, R. E. Jonkers, P. Hombrink, M. Bruchard, J. Villaudy, J. M. Munneke, W. Fokkens, J. S. Erjeflt, H. Spits, X. R. Ros, IL-1β, IL-4 and IL-12 control the

fate of group 2 innate lymphoid cells in human airway inflammation in the lungs. *Nat. Immunol.* **17**, 636–645 (2016).
37. J. S. Silver, J. Kearley, A. M. Copenhaver, C. Sanden, M. Mori, L. Yu, G. H. Pritchard, A. A. Berlin, C. A. Hunter, R. Bowler, J. S. Erjefalt, R. Kolbeck, A. A. Humbles, Inflammatory triggers associated with exacerbations of COPD orchestrate plasticity of group 2 innate lymphoid cells in the lungs. *Nat. Immunol.* **17**, 626–635 (2016).
38. C. Rajput, T. Cui, M. Han, J. Lei, J. L. Hinde, Q. Wu, J. Kelley Bentley, M. B. Hershenson, RORα-dependent type 2 innate lymphoid cells are required and sufficient for mucous metaplasia in immature mice. *Am. J. Physiol. - Lung Cell. Mol. Physiol.* **312**, L983–L993 (2017).
39. S. Taylor, Y. Huang, G. Mallett, S. Amarnath, PD-1 regulates KLRG1+ group 2 innate lymphoid cells. *J. Exp. Med*. **214**, 1663–1678 (2017).
40. T. Hoyler, C. S. N. Klose, A. Souabni, A. Turqueti-Neves, D. Pfeifer, E. L. Rawlins, D. Voehringer, M. Busslinger, A. Diefenbach, The Transcription Factor GATA-3 Controls Cell Fate and Maintenance of Type 2 Innate Lymphoid Cells. *Immunity*. **37**, 634–648 (2012).
41. C. Holmes, W. L. Stanford, Concise Review: Stem Cell Antigen-1: Expression, Function, and Enigma. *Stem Cells*. **25**, 1339–1347 (2007).
42. K. Moro, H. Kabata, M. Tanabe, S. Koga, N. Takeno, M. Mochizuki, K. Fukunaga, K. Asano, T. Betsuyaku, S. Koyasu, Interferon and IL-27 antagonize the function of group 2 innate lymphoid cells and type 2 innate immune responses. *Nat Immunol*. **17**, 76–86 (2016).
43. A. B. Molofsky, F. Van Gool, H. E. Liang, S. J. Van Dyken, J. C. Nussbaum, J. Lee, J. A. Bluestone, R. M. Locksley, Interleukin-33 and Interferon-gamma Counter-Regulate Group 2 Innate Lymphoid Cell Activation during Immune Perturbation. *Immunity*. **43**, 161–174 (2015).
44. E. S. Barton, D. W. White, J. S. Cathelyn, K. A. Brett-McClellan, M. Engle, M. S. Diamond, V. L. Miller, H. W. Virgin, Herpesvirus latency confers symbiotic protection from bacterial infection. *Nature*. **447**, 326–9 (2007).
45. C. Maquet, J. Baiwir, P. Loos, L. Rodriguez-Rodriguez, J. Javaux, R. Sandor, F. Perin, P. G. Fallon, M. Mack, D. Cataldo, L. Gillet, B. Machiels, Ly6Chi monocytes balance regulatory and cytotoxic CD4 T cell responses to control virus-induced immunopathology. *Sci. Immunol.* **7**, eabn3240 (2022).
46. D. G. Helou, P. Shafiei-Jahani, R. Lo, E. Howard, B. P. Hurrell, L. Galle-Treger, J. D. Painter, G. Lewis, P. Soroosh, A. H. Sharpe, O. Akbari, PD-1 pathway regulates ILC2 metabolism and PD-1 agonist treatment ameliorates airway hyperreactivity. *Nat. Commun.* **11**, 3998 (2020).
47. P. Fowler, S. Marques, J. P. Simas, S. Efstathiou, ORF73 of murine herpesvirus-68 is critical for the establishment and maintenance of latency, doi:10.1099/vir.0.19594-0.
48. M. W. Dahlgren, S. W. Jones, K. M. Cautivo, A. Dubinin, J. F. Ortiz-Carpena, S. Farhat, K. S. Yu, K. Lee, C. Wang, A. B. A. V. Molofsky, A. D. Tward, M. F. Krummel, T. Peng, A. B. A. V. Molofsky, Adventitial Stromal Cells Define Group 2 Innate Lymphoid Cell Tissue Niches. *Immunity*. **50**, 707-722.e6 (2019).
49. L. A. Monticelli, G. F. Sonnenberg, M. C. Abt, T. Alenghat, C. G. Ziegler, T. A. Doering, J. M. Angelosanto, B. J. Laidlaw, C. Y. Yang, T. Sathaliyawala, M. Kubota, D. Turner, J. M. Diamond, A. W. Goldrath, D. L. Farber, R. G. Collman, E. J. Wherry, D. Artis, Innate

lymphoid cells promote lung-tissue homeostasis after infection with influenza virus. *Nat Immunol*. **12**, 1045–1054 (2011).
50. G. La Manno, R. Soldatov, A. Zeisel, E. Braun, H. Hochgerner, V. Petukhov, K. Lidschreiber, M. E. Kastriti, P. Lönnerberg, A. Furlan, J. Fan, L. E. Borm, Z. Liu, D. van Bruggen, J. Guo, X. He, R. Barker, E. Sundström, G. Castelo-Branco, P. Cramer, I. Adameyko, S. Linnarsson, P. V. Kharchenko, RNA velocity of single cells. *Nature*. **560**, 494–498 (2018).
51. J. Kim, Y. Chang, B. Bae, K. H. Sohn, S. H. Cho, D. H. Chung, H. R. Kang, H. Y. Kim, Innate immune crosstalk in asthmatic airways: Innate lymphoid cells coordinate polarization of lung macrophages. *J. Allergy Clin. Immunol.* **143**, 1769-1782.e11 (2019).
52. S. Saluzzo, A. D. Gorki, B. M. J. Rana, R. Martins, S. Scanlon, P. Starkl, K. Lakovits, A. Hladik, A. Korosec, O. Sharif, J. M. Warszawska, H. Jolin, I. Mesteri, A. N. J. McKenzie, S. Knapp, First-Breath-Induced Type 2 Pathways Shape the Lung Immune Environment. *Cell Rep.* **18**, 1893–1905 (2017).
53. R. Browaeys, W. Saelens, Y. Saeys, NicheNet: modeling intercellular communication by linking ligands to target genes. *Nat. Methods*. **17**, 159–162 (2020).
54. M. Guilliams, I. De Kleer, S. Henri, S. Post, L. Vanhoutte, S. De Prijck, K. Deswarte, B. Malissen, H. Hammad, B. N. Lambrecht, Alveolar macrophages develop from fetal monocytes that differentiate into long-lived cells in the first week of life via GM-CSF. *J. Exp. Med.* **210**, 1977–1992 (2013).
55. A. D. Luster, P. Leder, IP-10, a -C-X-C- chemokine, elicits a potent thymus-dependent antitumor response in vivo. *J. Exp. Med.* **178**, 1057–1065 (1993).
56. D. D. Taub, A. R. Lloyd, K. Conlon, J. M. Wang, J. R. Ortaldo, A. Harada, K. Matsushima, D. J. Kelvin, J. J. Oppenheim, Recombinant human interferon-inducible protein 10 is a chemoattractant for human monocytes and T lymphocytes and promotes T cell adhesion to endothelial cells. *J. Exp. Med.* **177**, 1809–1814 (1993).
57. Y. Dong, A. A. Arif, J. Guo, Z. Ha, S. S. M. Lee-Sayer, G. F. T. Poon, M. Dosanjh, C. D. Roskelley, T. Huan, P. Johnson, CD44 Loss Disrupts Lung Lipid Surfactant Homeostasis and Exacerbates Oxidized Lipid-Induced Lung Inflammation. *Front. Immunol.* **11**, 29 (2020).
58. C. J. Oliphant, Y. Y. Hwang, J. A. Walker, M. Salimi, S. H. Wong, J. M. Brewer, A. Englezakis, J. L. Barlow, E. Hams, S. T. Scanlon, G. S. Ogg, P. G. Fallon, A. N. J. McKenzie, MHCII-mediated dialog between group 2 innate lymphoid cells and CD4+T cells potentiates type 2 immunity and promotes parasitic helminth expulsion. *Immunity*. **41**, 283–295 (2014).
59. F. R. Svedberg, S. L. Brown, M. Z. Krauss, L. Campbell, C. Sharpe, M. Clausen, G. J. Howell, H. Clark, J. Madsen, C. M. Evans, T. E. Sutherland, A. C. Ivens, D. J. Thornton, R. K. Grencis, T. Hussell, D. M. Cunoosamy, P. C. Cook, A. S. MacDonald, The lung environment controls alveolar macrophage metabolism and responsiveness in type 2 inflammation. *Nat. Immunol.* **20**, 571–580 (2019).
60. J. Beale, A. Jayaraman, D. J. Jackson, J. D. R. Macintyre, M. R. Edwards, R. P. Walton, J. Zhu, Y. M. Ching, B. Shamji, M. Edwards, J. Westwick, D. J. Cousins, Y. Y. Hwang, A. McKenzie, S. L. Johnston, N. W. Bartlett, Rhinovirus-induced IL-25 in asthma exacerbation drives type 2 immunity and allergic pulmonary inflammation. *Sci. Transl. Med.* **6**, 256ra134-256ra134 (2014).
61. M. T. Stier, M. H. Bloodworth, S. Toki, D. C. Newcomb, K. Goleniewska, K. L. Boyd, M.

Quitalig, A. L. Hotard, M. L. Moore, T. V. Hartert, B. Zhou, A. N. McKenzie, R. S. Peebles, Respiratory syncytial virus infection activates IL-13–producing group 2 innate lymphoid cells through thymic stromal lymphopoietin. *J. Allergy Clin. Immunol.* **138**, 814-824.e11 (2016).

62. B. W. S. S. Li, M. J. W. W. de Bruijn, M. Lukkes, M. van Nimwegen, I. M. Bergen, A. KleinJan, C. H. GeurtsvanKessel, A. Andeweg, G. F. Rimmelzwaan, R. W. Hendriks, B. W.S. Li, M. J.W. de Bruijn, M. Lukkes, M. van Nimwegen, I. M. Bergen, A. KleinJan, C. H. GeurtsvanKessel, A. Andeweg, G. F. Rimmelzwaan, R. W. Hendriks, B. W. S. S. Li, M. J. W. W. de Bruijn, M. Lukkes, M. van Nimwegen, I. M. Bergen, A. KleinJan, C. H. GeurtsvanKessel, A. Andeweg, G. F. Rimmelzwaan, R. W. Hendriks, B. W.S. Li, M. J.W. de Bruijn, M. Lukkes, M. van Nimwegen, I. M. Bergen, A. KleinJan, C. H. GeurtsvanKessel, A. Andeweg, G. F. Rimmelzwaan, R. W. Hendriks, B. W. S. S. Li, M. J. W. W. de Bruijn, M. Lukkes, M. van Nimwegen, I. M. Bergen, A. KleinJan, C. H. GeurtsvanKessel, A. Andeweg, G. F. Rimmelzwaan, R. W. Hendriks, T cells and ILC2s are major effector cells in influenza-induced exacerbation of allergic airway inflammation in mice. *Eur. J. Immunol.* **31**, 144–156 (2019).

63. K. R. Bartemes, G. M. Kephart, S. J. Fox, H. Kita, Enhanced innate type 2 immune response in peripheral blood from patients with asthma. *J. Allergy Clin. Immunol.* **134** (2014), doi:10.1016/j.jaci.2014.06.024.

64. M. M. Miller, P. S. Patel, K. Bao, T. Danhorn, B. P. O'Connor, R. L. Reinhardt, BATF acts as an essential regulator of IL-25–responsive migratory ILC2 cell fate and function. *Sci. Immunol.* **5**, eaay3994 (2020).

65. E. Boberg, K. Johansson, C. Malmhäll, J. Weidner, M. Rådinger, House dust mite induces bone marrow il-33responsive ILC2S and TH cells. *Int. J. Mol. Sci.* **21** (2020), doi:10.3390/ijms21113751.

66. C. U. Duerr, C. D. McCarthy, B. C. Mindt, M. Rubio, A. P. Meli, J. Pothlichet, M. M. Eva, J. F. Gauchat, S. T. Qureshi, B. D. Mazer, K. L. Mossman, D. Malo, A. M. Gamero, S. M. Vidal, I. L. King, M. Sarfati, J. H. Fritz, Type I interferon restricts type 2 immunopathology through the regulation of group 2 innate lymphoid cells. *Nat Immunol.* **17**, 65–75 (2016).

67. D. Califano, Y. Furuya, S. Roberts, D. Avram, A. N. J. McKenzie, D. W. Metzger, IFN-γ increases susceptibility to influenza A infection through suppression of group II innate lymphoid cells. *Mucosal Immunol.* **11**, 209–219 (2018).

68. Y. Ohne, J. S. Silver, L. Thompson-Snipes, M. A. Collet, J. P. Blanck, B. L. Cantarel, A. M. Copenhaver, A. A. Humbles, Y.-J. Liu, IL-1 is a critical regulator of group 2 innate lymphoid cell function and plasticity. *Nat. Immunol.* **17**, 646–655 (2016).

69. F. Li, F. Piattini, L. Pohlmeier, Q. Feng, H. Rehrauer, M. Kopf, Monocyte-derived alveolar macrophages autonomously determine severe outcome of respiratory viral infection. *Sci. Immunol.* **7**, eabj5761 (2022).

70. M. G. Netea, L. A. B. Joosten, Trained Immunity and Local Innate Immune Memory in the Lung. *Cell*. **175**, 1463–1465 (2018).

71. M. G. Netea, L. A. Joosten, E. Latz, K. H. Mills, G. Natoli, H. G. Stunnenberg, L. A. O'Neill, R. J. Xavier, Trained immunity: A program of innate immune memory in health and disease. *Science (80-.).* **352**, aaf1098 (2016).

72. H. Schlums, F. Cichocki, B. Tesi, J. Theorell, V. Beziat, T. D. Holmes, H. Han, S. C. C. Chiang, B. Foley, K. Mattsson, S. Larsson, M. Schaffer, K. J. Malmberg, H. G.

Ljunggren, J. S. Miller, Y. T. Bryceson, Cytomegalovirus infection drives adaptive epigenetic diversification of NK cells with altered signaling and effector function. *Immunity*. **42**, 443–456 (2015).
73. R. Stadhouders, B. W. S. Li, M. J. W. de Bruijn, A. Gomez, T. N. Rao, H. J. Fehling, W. F. J. van IJcken, A. I. Lim, J. P. Di Santo, T. Graf, R. W. Hendriks, Epigenome analysis links gene regulatory elements in group 2 innate lymphocytes to asthma susceptibility. *J. Allergy Clin. Immunol.* (2018), doi:10.1016/j.jaci.2017.12.1006.
74. Y. Lavin, D. Winter, R. Blecher-Gonen, E. David, H. Keren-Shaul, M. Merad, S. Jung, I. Amit, Tissue-resident macrophage enhancer landscapes are shaped by the local microenvironment. *Cell*. **159**, 1312–1326 (2014).
75. D. Gosselin, V. M. Link, C. E. Romanoski, G. J. Fonseca, D. Z. Eichenfield, N. J. Spann, J. D. Stender, H. B. Chun, H. Garner, F. Geissmann, C. K. Glass, Environment drives selection and function of enhancers controlling tissue-specific macrophage identities. *Cell*. **159**, 1327–1340 (2014).
76. M. Cohen, A. Giladi, A.-D. Gorki, D. G. Solodkin, M. Zada, A. Hladik, A. Miklosi, T.-M. Salame, K. B. Halpern, E. David, S. Itzkovitz, T. Harkany, S. Knapp, I. Amit, Lung Single-Cell Signaling Interaction Map Reveals Basophil Role in Macrophage Imprinting. *Cell*. **175**, 1031-1044.e18 (2018).
77. M. Guilliams, G. R. Thierry, J. Bonnardel, M. Bajenoff, Establishment and Maintenance of the Macrophage Niche. *Immunity*. **52**, 434–451 (2020).
78. L. van de Laar, W. Saelens, S. De Prijck, L. Martens, C. L. Scott, G. Van Isterdael, E. Hoffmann, R. Beyaert, Y. Saeys, B. N. Lambrecht, M. Guilliams, Yolk Sac Macrophages, Fetal Liver, and Adult Monocytes Can Colonize an Empty Niche and Develop into Functional Tissue-Resident Macrophages. *Immunity*. **44** (2016), doi:10.1016/j.immuni.2016.02.017.
79. C. Schneider, S. P. Nobs, M. Kurrer, H. Rehrauer, C. Thiele, M. Kopf, Induction of the nuclear receptor PPAR-γ 3 by the cytokine GM-CSF is critical for the differentiation of fetal monocytes into alveolar macrophages. *Nat. Immunol.* **15**, 1026–1037 (2014).
80. J. Gschwend, S. P. M. Sherman, F. Ridder, X. Feng, H.-E. E. Liang, R. M. Locksley, B. Becher, C. Schneider, Alveolar macrophages rely on GM-CSF from alveolar epithelial type 2 cells before and after birth. *J. Exp. Med.* **218** (2021), doi:10.1084/jem.20210745.
81. F. M. Lang, K. M. C. Lee, J. R. Teijaro, B. Becher, J. A. Hamilton, GM-CSF-based treatments in COVID-19: reconciling opposing therapeutic approaches. *Nat. Rev. Immunol.* **20**, 507 (2020).
82. C. Bosteels, K. F. A. Van Damme, E. De Leeuw, J. Declercq, B. Maes, V. Bosteels, L. Hoste, L. Naesens, N. Debeuf, J. Deckers, B. Cole, M. Pardons, D. Weiskopf, A. Sette, Y. Vande Weygaerde, T. Malfait, S. J. Vandecasteele, I. K. Demedts, H. Slabbynck, S. Allard, P. Depuydt, E. Van Braeckel, J. De Clercq, L. Martens, S. Dupont, R. Seurinck, N. Vandamme, F. Haerynck, D. F. Roychowdhury, L. Vandekerckhove, M. Guilliams, S. J. Tavernier, B. N. Lambrecht, Loss of GM-CSF-dependent instruction of alveolar macrophages in COVID-19 provides a rationale for inhaled GM-CSF treatment. *Cell Reports Med.* **3**, 100833 (2022).
83. H. Adler, M. Messerle, M. Wagner, U. H. Koszinowski, “Cloning and Mutagenesis of the Murine Gammaherpesvirus 68 Genome as an Infectious Bacterial Artificial Chromosome” (2000).
84. B. Machiels, P. G. Stevenson, A. Vanderplasschen, L. Gillet, A gammaherpesvirus uses

alternative splicing to regulate its tropism and its sensitivity to neutralization. *PLoS Pathog*. **9**, e1003753 (2013).
85. P. DI Tommaso, M. Chatzou, E. W. Floden, P. P. Barja, E. Palumbo, C. Notredame, Nextflow enables reproducible computational workflows. *Nat. Biotechnol.* **35** (2017), pp. 316–319.
86. M. I. Love, W. Huber, S. Anders, Moderated estimation of fold change and dispersion for RNA-seq data with DESeq2. *Genome Biol.* **15**, 550 (2014).
87. W. Huber, A. Von Heydebreck, H. Sültmann, A. Poustka, M. Vingron, in *Bioinformatics* (Oxford University Press, 2002; http://www.dkfz.de/abt0840/whuber), vol. 18, pp. 96–104.

Acknowledgments: The authors thank A. N.J. McKenzie (Cambridge University, UK) and H-R Rodewald (German Cancer Research Center DKFZ) for the Rorαlox/lox Il7rCre/+ mice; B.G. Dewals for critical discussions; the technician and administrative team of the Immunology-Vaccinology lab (especially L. Dams, M. Macar, S. Leemans and C. Espert), C. Humblet, A. Hego and the teams of GIGA imaging and genomic platforms and animal facility for very helpful assistance.

Funding:
This work was supported in part by University of Liège (VIR-IMPRINT ARC to L.G.), by Fondation Léon Fredericq (grant to P.L.), by the Fonds de la Recherche Scientifique - Fonds National Belge de la Recherche Scientifique (F.R.S./FNRS, "credit de recherche" J007515F to L.G.; "projet de recherche" T.0195.16 to L.G.; research associate support for B.M. and research fellow for P.L. and C.M., by Institut MERIEUX starting grant (to L.G.), by EOS joint programme of F.R.S./FNRS Fonds wetenschapellijk onderzoek – Vlaanderen - FWO (EOS ID:30981113) (to L.G.) and by ERC Starting Grant (ERC-StG-2020 VIROME, ID:853608) (to B.M.)

Author contributions: P.L., T.M., L.G. and B.M. designed the experiments. P.L., C.M., J.J., R.S., F.L. and B.M., and C.M. did most of the experiments. P.L. compiled the data. J.B. performed the transcriptomic analyses. P.L., L.G. and B.M. analyzed the data; P.L. and J.B. prepared the figures; P.L., B.M. and L.G. wrote the manuscript.

Competing interests: The authors declare no competing interests.

Data and materials availability: All data and codes used in this study are available from the corresponding authors upon request. All sequencing data are available on GEO repository (GSE218248).

Figures:

Fig. 1. MuHV-4 infection reduces the number of lung ILC2s and modifies their functional properties after HDM treatment.

(A) Experimental layout of MuHV-4 infection and high-dose HDM sensitization or challenge in 8-week-old-BALB/c mice (n= 4-8 in each group).

(B) Percentage and absolute numbers of eosinophils (out AMs (autofluorescent $CD11c^{+}SSC\text{-}A^{high}$) $Siglec\text{-}F^{+}CD11b^{+}$ living cells) from BALF.

(C) Strategy for the identification of lung ILC2s by flow cytometry. Lineage was defined as B220, CD11c, CD3, CD4, CD49b, CD4, CD8α, F4/80, FcεRI, Gr1 and Siglec-F. ILC2s are identified as $Lin^{-}CD45^{+}ST2^{+}CD90.2^{+}CD25^{+}$ living cells.

(D) Absolute numbers of lung ILC2s and ILC1-3s ($Lin^{-}CD45^{+}ST2^{+}CD90.2^{+}$ $Nkp46^{+}$ living cells).

(E) Representative flow cytometry plots and histograms of GATA3 staining in lung ILC2s.

(F) Mean fluorescence intensity (MFI) of GATA3 staining in lung ILC2s.

(G) Representative flow cytometry of intracellular staining of IL-5 and IL-13 pre-gated on lung ILC2s, numbers indicate the percentage of positive cells in each quadrant.

(H-I) Percentage and absolute numbers of $IL\text{-}5^{+}$ (H) and $IL\text{-}13^{+}$ (I) ILC2s in lung.

(J-L) 8 week-old-BALB/c mice were infected or not with MuHV-4 and subjected to a low-dose HDM sensitization or challenge (n= 5 in each group).

(J) Experimental layout.

(K) Quantification of necrosis (Annexin-V and 7-AAD double positive) and early apoptosis (Annexin-V positive and 7-AAD negative) in lung ILC2s.

(L) Percentage of $Ki67^{+}$ cells among lung ILC2s.

(M-P) 8 week-old-$CD45.2^{+}$ BALB/c mice were lethally irradiated, sparing the thoracic area, and transplanted with $CD45.1^{+}$ BM before being infected or not with MuHV-4 and subjected to a low-dose HDM challenge (n= 5 in each group).

(M) Experimental layout.

(N) Percentage of eosinophils (out AMs (autofluorescent $CD11c^{+}SSC\text{-}A^{high}$) $Siglec\text{-}F^{+}CD11b^{+}$ living cells) from BALF.

(O) Representative cytometry plots for the evaluation of chimerism between recipient ($CD45.2^{+}$) ad donor ($CD45.1^{+}$) cells in lung ILC2s.

(P) Absolute numbers of $CD45.1^{+}$ and $CD45.2^{+}$ cells among lung ILC2s.

For comparisons between two groups, Student's two-tailed t test was used. For comparisons between multiple groups, one-way or two-way ANOVA was used with multiple-comparison tests. *P < 0.05, **P < 0.01, ***P < 0.001, and ****P < 0.0001.

Error bars represent SEM. Data are representative of at least three independent experiments.

Fig. 2. MuHV-4 infection imprints changes on lung ILC2 transcriptional program.

8-week-old-BALB/c mice (n= 7 in each group) were infected or not with MuHV-4 and subjected to high-dose HDM sensitization or challenge before droplet-based single cell RNA-sequencing of ILC2s.

(A) Experimental layout.

(B) Violin plots of ILC1s, ILC2s and ILC3s canonical transcription factors expression in lung ILC2s.

(C) MFI of T-bet and IFN-γ staining of lung ILC2s of mock or MuHV-4 infected mice, treated or not with HDM measured by flow cytometry.

(D) Non-linear representation (UMAP) of the top 15 principal components (PCs) of 24,449 ILC2s split between the 6 conditions, cells are coloured by cluster.
(E) Heatmap representing the 10 most expressed genes for each cluster.
(F) Proportion of condition within each cluster of (D).
(G) Differentially expressed genes (*y* axis) by condition (*x* axis) in lung ILC2s. Dot size represents the fraction of cells in the cluster that express the gene and colour indicates the mean expression (logTPX (see Methods)) relative to each gene.
(H) Volcano plot comparison of whole transcriptome gene expression of ILC2s (defined as statistically significant adjusted false-discovery rate (FDR) <0.05).
(I) Representative flow cytometry plots of ST2 and KLRG1 expression in lung ILC2s (gated $CD45^+Lin^-CD90.2^+CD25^+$ living cells) 24h after intranasal instillation of high-dose HDM in mock- or MuHV-4 infected mice.
(J) Percentage of KLRG1, PD-1, Sca1 and ST2 expression in lung ILC2s from mock- or MuHV-4 infected mice subjected to high-dose HDM sensitization or challenge.
(K) ELISA measurement of IL-33 in BALF from mock- or MuHV-4 infected mice 24h after intranasal instillation of high-dose HDM (n= 10 in each group).
(L) Expression of IL-33 analyzed by RT-qPCR in lung from mock- or MuHV-4 infected-mice (n= 5 in each group) 2 or 6h after intranasal instillation of high-dose HDM.
(M) Enrichment for transcriptomic fingerprints specific for 12 Gene Ontology sets by gene set enrichment analysis with BubbleGum software in lung ILC2s. The color indicates the cell subset showing enrichment for the gene set. The surface area of the dots is proportional to the absolute value of the normalized enrichment score (NES). The color intensity indicates the false-discovery rate (FDR). Numbers in parentheses indicate the number of genes in each gene-set. NS, not significant
For comparisons between two groups, Student's two-tailed t test was used. For comparisons between multiple groups, one-way or two-way ANOVA was used with multiple-comparison tests. *P < 0.05, **P < 0.01, ***P < 0.001, and ****P < 0.0001.
. Error bars represent SEM. Analyses were performed using R.

Fig. 3. IFN-γ directs the functional impairment of pulmonary ILC2s after MuHV-4 infection

(A-C) $CD45.1.2^+$ C57BL/6 mice were exposed to lethal irradiation protocol (6Gy) before being transplanted with a mix (1:1) of $CD45.1^+$ WT and $CD45.2^+$ IFN-$\gamma R^{-/-}$ congenic donor BM cells. 8 weeks after transfer, those mice were subjected to MuHV-4 infection and then to HDM low-dose sensitization and challenge (n= 4-5 in each group).
(A) Experimental layout.
(B) Representative flow cytometry plots of IL-5 and IL-13 staining in lung. WT and IFN-$\gamma R^{-/-}$ lung ILC2s from the same mouse are shown. Numbers indicate the percentage of positive cells in each quadrant.
(C) Percentage of $IL\text{-}5^+$ and $IL\text{-}13^+$ cells among donor and host lung ILC2s.
(D-E) Absolute numbers of ILC2s (D) in lung and eosinophils (E) in BALF.
(F) ELISA measurement of IFN-γ in BALF at indicated times post-MuHV-4 infection in C57BL/6 mice (n= 4 in each group).
(G-I) C57BL/6 were subjected to MuHV-4 infection and analyzed at indicated times post-infection (n=5 in each group).
(G) Experimental layout.
(H) Percentage of $IL\text{-}13^+$ cells among lung ILC2s.

(I) Representative flow cytometry plots of Sca1 and PD-1 expression in lung ILC2s. Numbers indicate the percentage of positive cells in each quadrant.
(J-L) CD45.1.2$^+$ C57BL/6 mice were exposed to lethal irradiation protocol (6Gy) before being transplanted with a mix (1:1) of CD45.1$^+$ WT and CD45.2$^+$ IFN-γR$^{-/-}$ congenic donor BM cells. 8 weeks after transfer, those mice were subjected to MuHV-4 infection (n= 4 in each group).
(J) Experimental layout.
(K) Absolute numbers of ILC2s in lung.
(L) Percentage of IL-5$^+$ and IL-13$^+$ cells among donor and host lung ILC2s.
(M-P) 8-week-old-BALB/c mice (n= 5 in each group) were infected or not with MuHV-4 WT or with latency-deficient viral mutant (Del73 strain).
(M) Experimental layout.
(N) Absolute numbers of eosinophils (out AMs (autofluorescent CD11c$^+$SSC-A^{high}) Siglec-F$^+$CD11b$^+$ living cells) from BALF.
(O) Percentage of Ki67$^+$ cells among lung ILC2s.
(P) Percentage of IL-13$^+$ and IL-5$^+$ ILC2s in lung.
For comparisons between two groups, Student's two-tailed t test was used. For comparisons between multiple groups, one-way or two-way ANOVA was used with multiple-comparison tests. *P < 0.05, **P < 0.01, ***P < 0.001, and ****P < 0.0001.
Error bars represent SEM.

Fig. 4. Monocyte-derived alveolar macrophages reconstituting the alveolar niche after infection are in close contact with lung ILC2s.
(A-C) 8-week-old BALB/c mice were infected or not with MuHV-4 (n= 4 in each group).
(A) Experimental layout.
(B) Percentage of AMs (described as autofluorescent CD11c$^+$ living cells) and absolute numbers of Mos (described as CD11b$^+$Ly6C$^+$ living cells) from BALF.
(C) MFI of MHC-II and Siglec-F in BALF AMs.
(D-H) 8 week-old IL-5 reporter mice (Red5) were infected or not with MuHV-4, and lungs tissues were subjected to immunostaining and imaged at different times post-MuHV-4 infection.
(D) Experimental layout.
(E) 2D thin-cut images from the indicated conditions. Red circles highlight close contact between ILC2s and myeloid cells. Images are representative of 3 mice.
(F) Immunostaining for ILC2s (CD3$^-$ IL-5$^+$ cells), T cells (CD3$^+$ cells), resident AMs (CD68$^+$CD11c$^+$ cells), Mos (CD68$^+$CD11b$^+$ cells), Mo-derived AMs (CD68$^+$CD11b$^+$CD11c$^+$ cells) and Neutrophils (CD68$^-$CD11b$^+$ cells).
(G) Unsupervised quantification of the distance between CD68+ cells and ILC2s or neutrophils.
(H) Unsupervised quantification of the percentage of different subtypes of myeloid cells in shortest distance < 5μm to ILC2s (I).
For comparisons between two groups, Student's two-tailed t test was used. For comparisons between multiple groups, one-way or two-way ANOVA was used with multiple-comparison tests. *P < 0.05, **P < 0.01, ***P < 0.001, and ****P < 0.0001.
Error bars represent SEM.

Fig. 5. MuHV-4 infection induces changes in the transcriptional profiles of AM and ILC2, reflecting key cell-cell interactions underlying AM differentiation and identity.

Lung ILC2s (gated as $CD45^+Lin^-CD90.2^+$ living cells) and BALF AMs (gated as autofluorescent $CD11c^+$ living cells) from mock or MuHV-4 infected-8-week-old at different times post-infection.
(A) Experimental layout.
(B) Non-linear representation (UMAP) of the top 20 principal components (PCs) of 6,291 ILC2s, 244 ILC1-3s and 9,833 AMs pooled from the different time points.
(C) Proportions of lung ILC2s and ILC1-3s based on the transcriptomic data at different times post-infection.
(D) UMAP of the top 20 PCs of ILC2s, cells are colored by cluster. Heatmap represents the 10 most expressed genes for each cluster.
(E) Proportion of clusters in (D) at different times post-infection.
(F) Feature plots of the expression of the indicated genes in ILC2s, mapped to the UMAP in (D).
(G) UMAP of the top 20 PCs of myeloid cells. The cells were clustered into 7 groups, based on common genes expression profiles. Heatmap representing the 10 most expressed genes for each cluster.
(H) Proportion of clusters in (G) at different times post-infection.
(I) RNA velocity in macrophages, mapped to the UMAP in (G).
(J) Grouping of clusters in indicated populations based on the genes expression profiles and RNA velocity.
(K) Feature plots of the expression of indicated genes in macrophages, mapped to the UMAP in (G).
(L) Circular plot of the putative interactions between ILC2s' ligands (top), AMs' receptors (bottom) and the target genes activated by these interactions (up- or down-regulated) in AMs based on their expression at day 14 post-MuHV-4 infection. Opacity of the link correlates with the interaction score (alpha from 0.25 to 1).
(M) Circular plot of the putative interactions between AMs' ligands (top), ILC2s' receptors (bottom) and the target genes activated by these interactions (up- or down-regulated) in ILC2s based on their expression at day 28 post-MuHV-4 infection. Opacity of the link correlates with the interaction score (alpha from 0.25 to 1).
Analyses were performed using R.

Fig. 6. MuHV-4 infection inhibits the capacity of lung ILC2s to polarize AMs towards a "M2-phenotype" *ex vivo*.
BM Mos and lung epithelial cells (ECs) from mock infected mice were cultured *ex vivo* for three days before addition or not of lung ILC2s from mice mock or MuHV-4 infected 8 days before. Flow cytometry analysis and bulk RNA sequencing of sorted Mo-derived macrophages (gated as autofluorescent $CD11c^+$ living cells) were performed 3 days after addition of ILC2s.
(A) Experimental layout.
(B) Sca1 expression in ILC2s from the indicated conditions.
(C) MFI of CD11c, Siglec-F, Arg1 and MHC-II expression in Mos from the indicated conditions.
(D) Relative expression of genes associated with cell differentiation in Mo-derived macrophages isolated from the different co-cultures.
(E) Principal-component analysis (PCA) of Mo-derived macrophages isolated from the different co-cultures.
(F) Expression of all genes expressed differentially (FDR<0,05; change in expression of over twofold) in Mo-derived macrophages isolated from the different co-cultures.

(G) Biological processes identified by Panther analysis of DE upregulated genes between Mos cultured or not with ILC2s from mock-infected mice (FDR ≤ 0,05).
(H-I) Volcano plot for differentially expressed (DE) genes (FDR<0.05) by Mos cultured or not with ILC2s from mock-infected mice (H) or cultured with ILC2s of mock- or MuHV-4 infected mice (I).
For comparisons between two groups, Student's two-tailed t test was used. For comparisons between multiple groups, one-way or two-way ANOVA was used with multiple-comparison tests. *P < 0.05, **P < 0.01, ***P < 0.001, and ****P < 0.0001.
Error bars represent SEM.

Fig. 7. Lung ILC2s from MuHV-4 infected mice maintain a "non M2-phenotype" of Mo-derived AMs, which requires GM-CSF and has subsequent consequences for HDM-induced airway allergy.
(A-G) BM Mos or resident AMs and ECs from mock infected mice were cultured *ex vivo* with or without lung ILC2s from mice mock or MuHV-4 infected 8 days before.
(A) Experimental layout.
(B) Representative flow cytometry plots of indicated cell populations.
(C) Proportion of indicated cell populations in the indicated conditions.
(D-E) Total count of AMs (D) and indicated cell populations (E) of the indicated conditions.
(F) MFI of CD11c of indicated cell populations of the indicated conditions.
(G) Representative flow cytometry plots of indicated conditions, numbers indicate the percentage of gated population in each quadrant.
(H-I) 8-week-old C57BL/6 mice were infected or not with MuHV-4 and subjected to five daily instillations of rIL-13 and analyses were before one day after the last instillation (n= 5 in each group).
(H) Experimental layout.
(I) Percentage of RELMα$^+$ and Arg1$^+$ AMs from BALF from the indicated conditions.
(J-L) 8-week-old-ILC2s deficient mice (n= 5-6 in each group) were infected or not with MuHV-4 and subjected to low-dose HDM sensitization or challenge before analysis.
(J) Experimental layout.
(K-L) Percentage of YM1$^+$ (K) or RELMα$^+$ (L) AMs from BALF from the indicated conditions.
(M-O) 8-week-old-ILC2s deficient mice (n= 5 to 10 in each group) were infected or not with MuHV-4 and subjected to low-dose HDM challenge before analysis. Absolute numbers of eosinophils from BALF.
(M) Experimental layout.
(N) Absolute numbers of eosinophils (out AMs (autofluorescent CD11c+SSC-Ahigh) Siglec-F+CD11b+ living cells) from BALF.
(O) Percentage of RELMα$^+$ and Arg1$^+$ AMs from BALF from the indicated conditions.
(P-R) AMs were transfer from 8-week-old-ILC2s deficient mice or not, infected or not with MuHV-4, to 8-week-old-CD45.1 C57BL.6 mice subjected to a low-dose challenge of HDM 3 days after cell transfer (n= 5-10 in each group).
(P) Experimental layout.
(Q) Representative flow cytometry plots for the evaluation of the AMs transfer between recipient (CD45.1$^+$) and donor (CD45.2$^+$) cells AMs. Expression of MHC-II and SiglecF by transferred (donor) AMs from indicated conditions.
(R) Absolute numbers of eosinophils in BALF from indicated conditions.

For comparisons between two groups, Student's two-tailed t test was used. For comparisons between multiple groups, one-way or two-way ANOVA was used with multiple-comparison tests. *P < 0.05, **P < 0.01, ***P < 0.001, and ****P < 0.0001.
Error bars represent SEM.

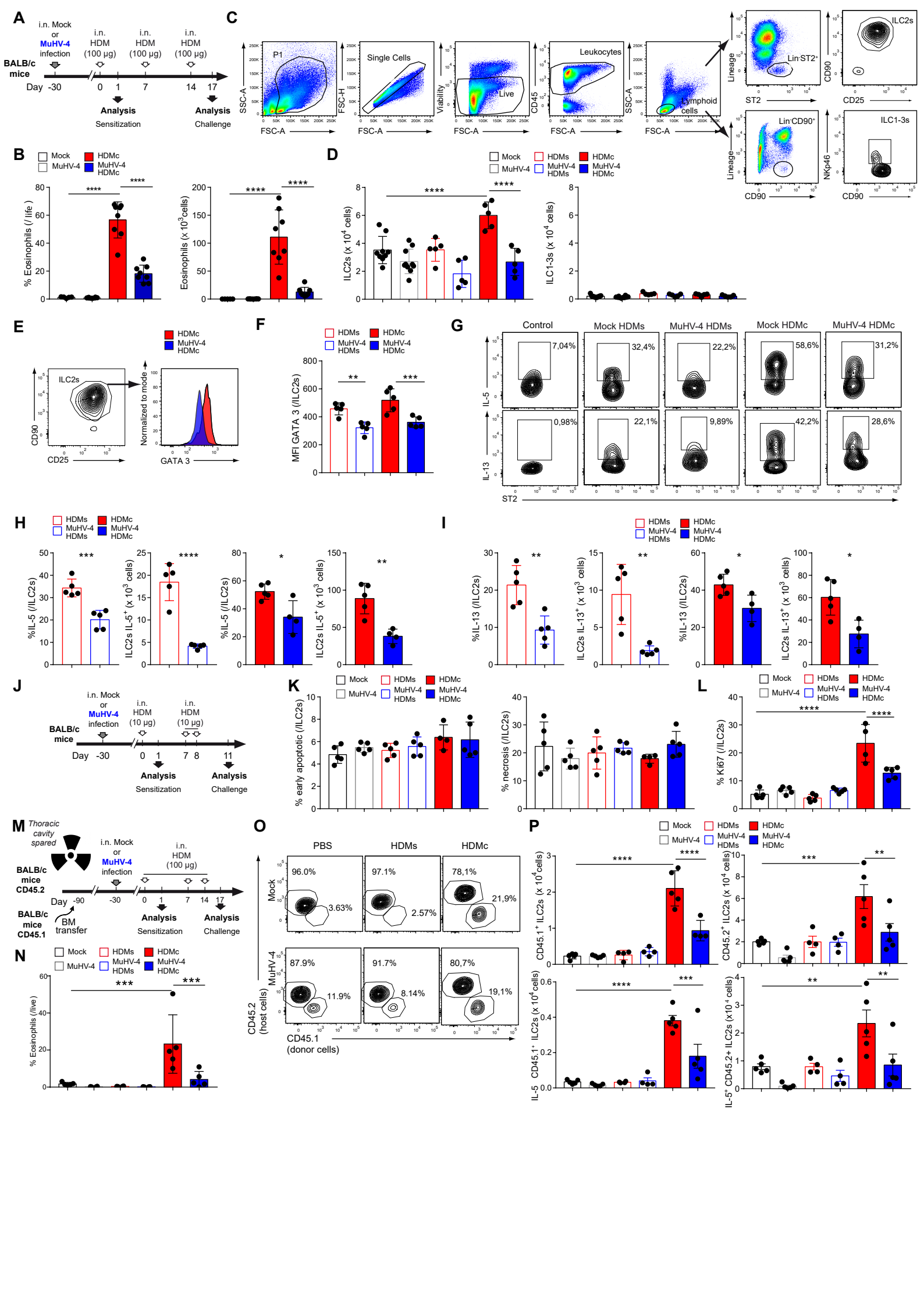
A
i.n. Mock or MuHV-4 infection
i.n. HDM (100 µg)
i.n. HDM (100 µg)
i.n. HDM (100 µg)
BALB/c mice
Day -30
0
1
7
14
17
Analysis
Sensitization
Analysis
Challenge
B
Mock
MuHV-4
HDMc
MuHV-4 HDMc
% Eosinophils (/ life)
Eosinophils (x 10³cells)
C
P1
SSC-A
FSC-A
Single Cells
FSC-H
Viability
Live
CD45
Leukocytes
Lymphoid cells
Lineage
Lin⁻ST2⁺
ST2
ILC2s
CD90
CD25
Lin⁻CD90⁺
ILC1-3s
NKp46
D
HDMs
MuHV-4 HDMs
ILC2s (x 10⁴ cells)
ILC1-3s (x 10⁴ cells)
E
ILC2s
CD90
CD25
Normalized to mode
GATA 3
F
MFI GATA 3 (/ILC2s)
G
Control
Mock HDMs
MuHV-4 HDMs
Mock HDMc
MuHV-4 HDMc
7,04%
32,4%
22,2%
58,6%
31,2%
0,98%
22,1%
9,89%
42,2%
28,6%
IL-5
IL-13
ST2
H
%IL-5 (/ILC2s)
ILC2s IL-5⁺ (x 10³ cells)
I
%IL-13 (/ILC2s)
ILC2s IL-13⁺ (x 10³ cells)
J
i.n. Mock or MuHV-4 infection
i.n. HDM (10 µg)
i.n. HDM (10 µg)
BALB/c mice
Day -30
0
1
7
8
11
Analysis
Sensitization
Analysis
Challenge
K
% early apoptotic (/ILC2s)
% necrosis (/ILC2s)
L
% Ki67 (/ILC2s)
M
Thoracic cavity spared
i.n. Mock or MuHV-4 infection
i.n. HDM (100 µg)
BALB/c mice CD45.2
BALB/c mice CD45.1
BM transfer
Day -90
-30
0
1
7
14
17
Analysis
Sensitization
Analysis
Challenge
N
% Eosinophils (/live)
O
PBS
HDMs
HDMc
Mock
MuHV-4
96.0%
3.63%
97.1%
2.57%
78,1%
21,9%
87.9%
11.9%
91.7%
8.14%
80,7%
19,1%
CD45.2 (host cells)
CD45.1 (donor cells)
P
CD45.1⁺ ILC2s (x 10⁴ cells)
CD45.2⁺ ILC2s (x 10⁴ cells)
IL-5⁺ CD45.1⁺ ILC2s (x 10⁴ cells)
IL-5⁺ CD45.2+ ILC2s (x10⁴ cells)

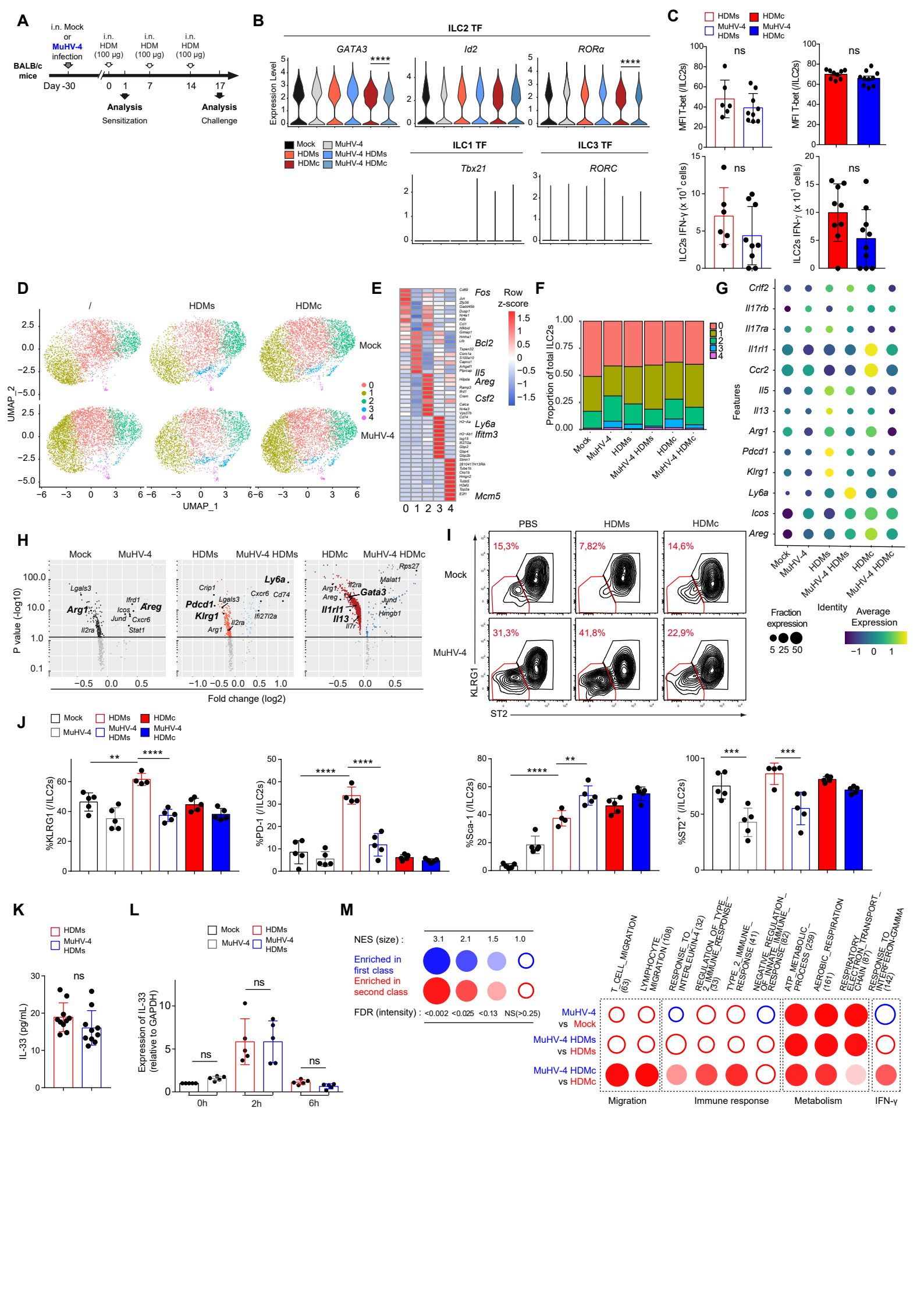
A
i.n. Mock or MuHV-4 infection
i.n. HDM (100 µg)
i.n. HDM (100 µg)
i.n. HDM (100 µg)
BALB/c mice
Day -30
0
1
7
14
17
Analysis
Sensitization
Analysis
Challenge
B
ILC2 TF
GATA3
Id2
RORα
Expression Level
****
Mock
HDMs
HDMc
MuHV-4
MuHV-4 HDMs
MuHV-4 HDMc
ILC1 TF
ILC3 TF
Tbx21
RORC
C
HDMs
MuHV-4 HDMs
HDMc
MuHV-4 HDMc
MFI T-bet (/ILC2s)
ILC2s IFN-γ (x 10^-1 cells)
ns
D
/
HDMs
HDMc
Mock
MuHV-4
UMAP_1
UMAP_2
E
Fos
Bcl2
Il5
Areg
Csf2
Ly6a
Ifitm3
Mcm5
Row z-score
F
Proportion of total ILC2s
Mock
MuHV-4
HDMs
MuHV-4 HDMs
HDMc
MuHV-4 HDMc
G
Crlf2
Il17rb
Il17ra
Il1rl1
Ccr2
Il5
Il13
Arg1
Pdcd1
Klrg1
Ly6a
Icos
Areg
Features
Fraction expression
Identity
Average Expression
H
Mock
MuHV-4
HDMs
MuHV-4 HDMs
HDMc
MuHV-4 HDMc
P value (-log10)
Fold change (log2)
Arg1
Areg
Icos
Jund
Cxcr6
Stat1
Il2ra
Lgals3
Ifrd1
Pdcd1
Klrg1
Crip1
Cxcr6
Cd74
Ly6a
Ifi27l2a
Gata3
Il1rl1
Il13
Il7r
Malat1
Jund
Hmgb1
Rps27
I
PBS
HDMs
HDMc
Mock
MuHV-4
15,3%
7,82%
14,6%
31,3%
41,8%
22,9%
KLRG1
ST2
J
Mock
MuHV-4
HDMs
MuHV-4 HDMs
HDMc
MuHV-4 HDMc
%KLRG1 (/ILC2s)
%PD-1 (/ILC2s)
%Sca-1 (/ILC2s)
%ST2+ (/ILC2s)
K
HDMs
MuHV-4 HDMs
IL-33 (pg/mL)
ns
L
Mock
MuHV-4
HDMs
MuHV-4 HDMs
Expression of IL-33 (relative to GAPDH)
0h
2h
6h
M
NES (size) :
3.1
2.1
1.5
1.0
Enriched in first class
Enriched in second class
FDR (intensity) :
<0.002
<0.025
<0.13
NS(>0.25)
T_CELL_MIGRATION (63)
LYMPHOCYTE MIGRATION (108)
RESPONSE_TO_INTERLEUKIN-4 (32)
REGULATION_OF_TYPE_2_IMMUNE_RESPONSE (33)
TYPE_2_IMMUNE_RESPONSE (41)
NEGATIVE_REGULATION_OF_INNATE_IMMUNE_RESPONSE (82)
ATP_METABOLIC_PROCESS (259)
AEROBIC_RESPIRATION (161)
RESPIRATORY_ELECTRON_TRANSPORT_CHAIN (87)
RESPONSE_TO_INTERFERON-GAMMA (142)
MuHV-4 vs Mock
MuHV-4 HDMs vs HDMs
MuHV-4 HDMc vs HDMc
Migration
Immune response
Metabolism
IFN-γ

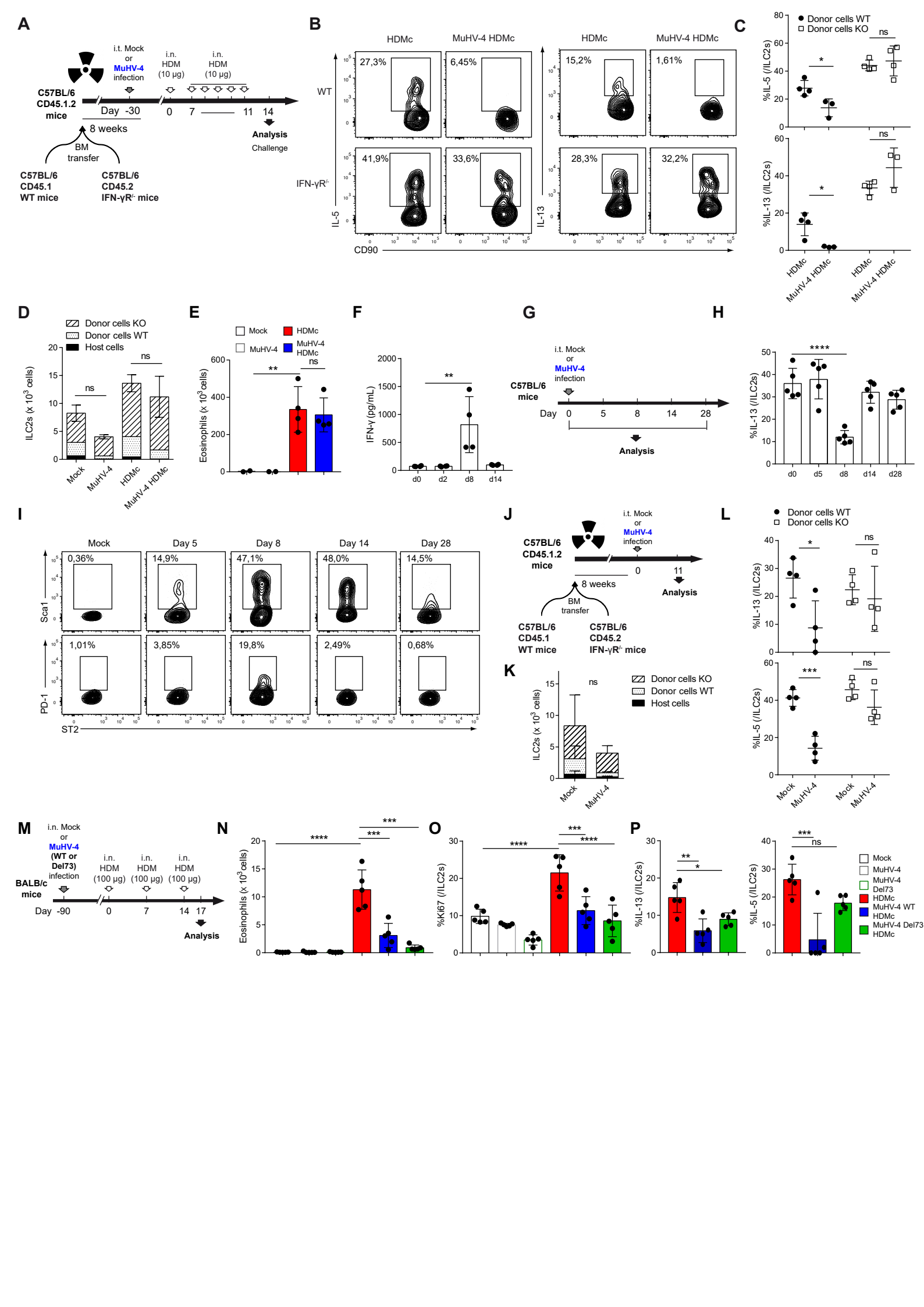
A
i.t. Mock or MuHV-4 infection
i.n. HDM (10 µg)
i.n. HDM (10 µg)
C57BL/6 CD45.1.2 mice
Day -30
0
7
11
14
Analysis
Challenge
8 weeks
BM transfer
C57BL/6 CD45.1 WT mice
C57BL/6 CD45.2 IFN-γR-/- mice
B
HDMc
MuHV-4 HDMc
HDMc
MuHV-4 HDMc
WT
IFN-γR-/-
27,3%
6,45%
15,2%
1,61%
41,9%
33,6%
28,3%
32,2%
IL-5
IL-13
CD90
C
Donor cells WT
Donor cells KO
ns
%IL-5 (/ILC2s)
%IL-13 (/ILC2s)
HDMc
MuHV-4 HDMc
D
Donor cells KO
Donor cells WT
Host cells
ILC2s (x 10³ cells)
Mock
MuHV-4
HDMc
MuHV-4 HDMc
E
Mock
MuHV-4
HDMc
MuHV-4 HDMc
Eosinophils (x 10³ cells)
F
IFN-γ (pg/mL)
d0
d2
d8
d14
G
i.t. Mock or MuHV-4 infection
C57BL/6 mice
Day 0 5 8 14 28
Analysis
H
%IL-13 (/ILC2s)
d0
d5
d8
d14
d28
I
Mock
Day 5
Day 8
Day 14
Day 28
0,36%
14,9%
47,1%
48,0%
14,5%
1,01%
3,85%
19,8%
2,49%
0,68%
Sca1
PD-1
ST2
J
i.t. Mock or MuHV-4 infection
C57BL/6 CD45.1.2 mice
0
11
Analysis
8 weeks
BM transfer
C57BL/6 CD45.1 WT mice
C57BL/6 CD45.2 IFN-γR-/- mice
K
Donor cells KO
Donor cells WT
Host cells
ILC2s (x 10³ cells)
Mock
MuHV-4
L
Donor cells WT
Donor cells KO
%IL-13 (/ILC2s)
%IL-5 (/ILC2s)
Mock
MuHV-4
M
i.n. Mock or MuHV-4 (WT or Del73) infection
BALB/c mice
i.n. HDM (100 µg)
i.n. HDM (100 µg)
i.n. HDM (100 µg)
Day -90
0
7
14
17
Analysis
N
Eosinophils (x 10³ cells)
O
%Ki67 (/ILC2s)
P
%IL-13 (/ILC2s)
%IL-5 (/ILC2s)
Mock
MuHV-4
MuHV-4 Del73
HDMc
MuHV-4 WT HDMc
MuHV-4 Del73 HDMc

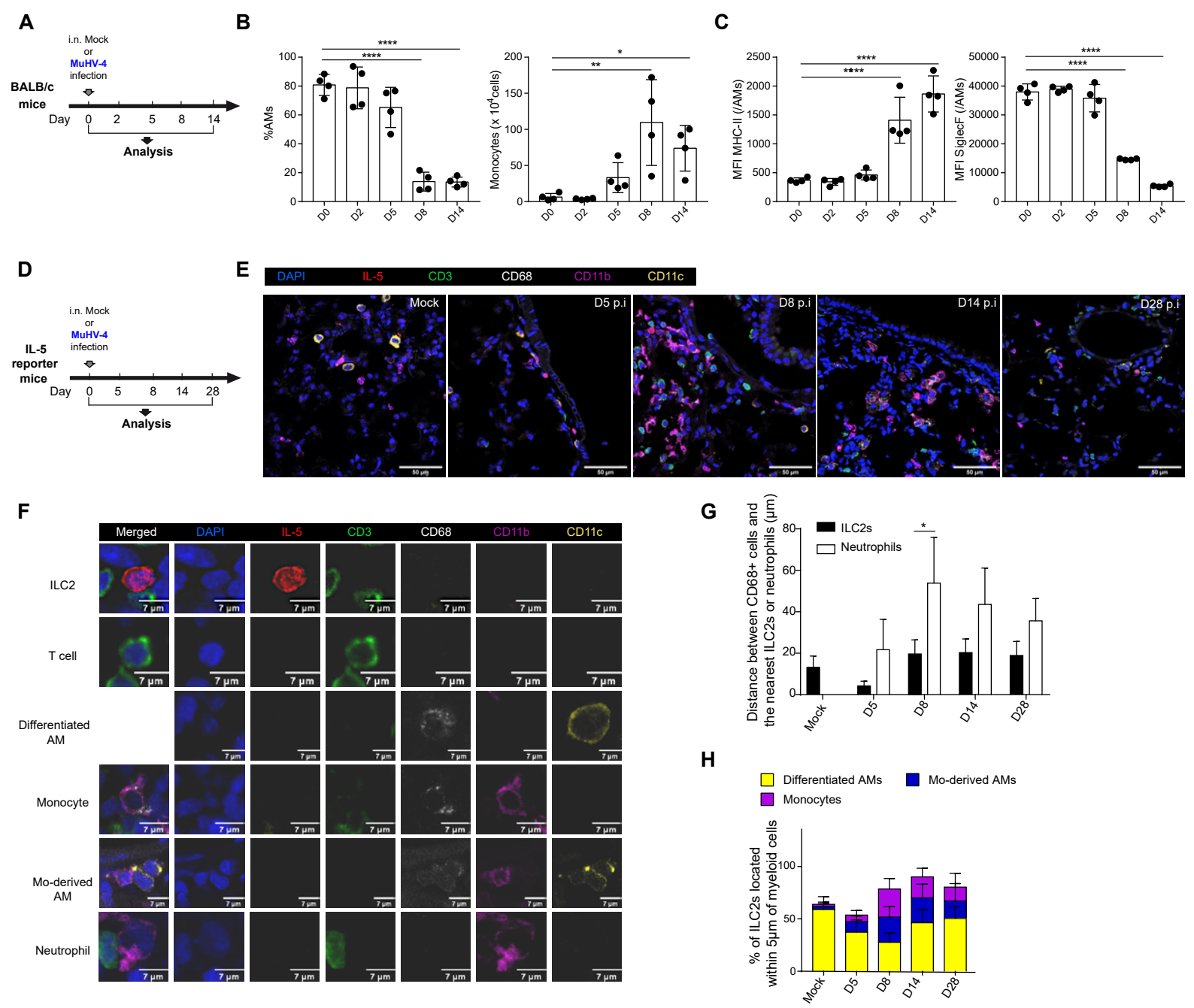
A
i.n. Mock or MuHV-4 infection
BALB/c mice
Day 0 2 5 8 14
Analysis
B
%AMs
Monocytes (x 10^4 cells)
D0 D2 D5 D8 D14
C
MFI MHC-II (/AMs)
MFI SiglecF (/AMs)
D
i.n. Mock or MuHV-4 infection
IL-5 reporter mice
Day 0 5 8 14 28
Analysis
E
DAPI IL-5 CD3 CD68 CD11b CD11c
Mock
D5 p.i
D8 p.i
D14 p.i
D28 p.i
F
Merged DAPI IL-5 CD3 CD68 CD11b CD11c
ILC2
T cell
Differentiated AM
Monocyte
Mo-derived AM
Neutrophil
7 µm
G
ILC2s
Neutrophils
Distance between CD68+ cells and the nearest ILC2s or neutrophils (µm)
Mock D5 D8 D14 D28
H
Differentiated AMs
Mo-derived AMs
Monocytes
% of ILC2s located within 5µm of myeloid cells
Mock D5 D8 D14 D28

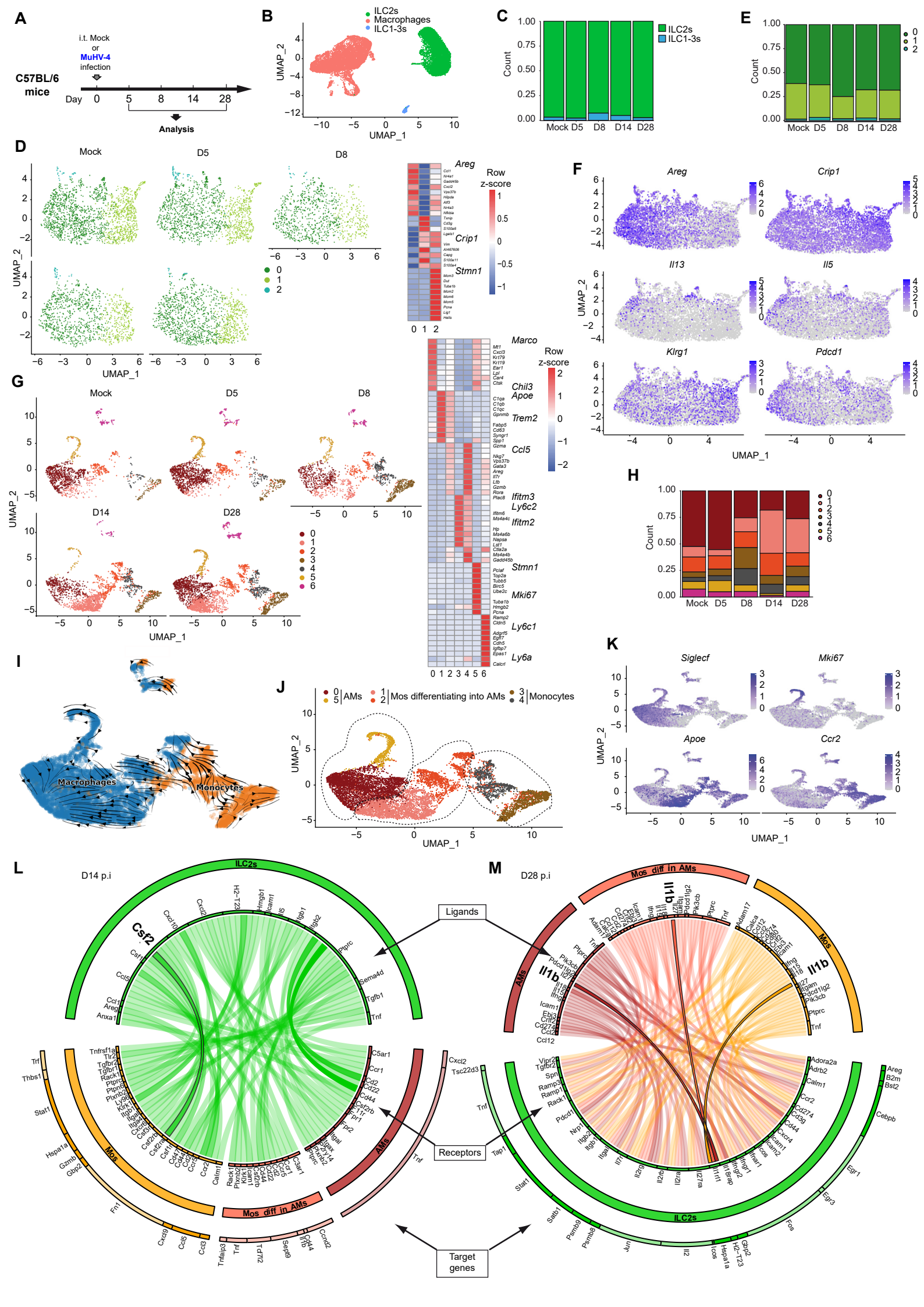
A
i.t. Mock
or
MuHV-4
infection
C57BL/6
mice
Day 0 5 8 14 28
Analysis
B
ILC2s
Macrophages
ILC1-3s
UMAP_1
UMAP_2
C
ILC2s
ILC1-3s
Count
Mock D5 D8 D14 D28
E
Count
Mock D5 D8 D14 D28
D
Mock
D5
D8
UMAP_1
UMAP_2
Areg
Crip1
Stmn1
Row z-score
F
Areg
Crip1
Il13
Il5
Klrg1
Pdcd1
UMAP_1
UMAP_2
G
Mock
D5
D8
D14
D28
UMAP_1
UMAP_2
Marco
Chil3
Apoe
Trem2
Ccl5
Ifitm3
Ly6c2
Ifitm2
Stmn1
Mki67
Ly6c1
Ly6a
Row z-score
H
Count
Mock D5 D8 D14 D28
I
Macrophages
Monocytes
J
0 5 AMs
1 2 Mos differentiating into AMs
3 4 Monocytes
UMAP_1
UMAP_2
K
Siglecf
Mki67
Apoe
Ccr2
UMAP_1
UMAP_2
L
D14 p.i
ILC2s
Csf2
Mos
Mos diff in AMs
AMs
Ligands
Receptors
Target genes
M
D28 p.i
Mos diff in AMs
Il1b
AMs
Mos
ILC2s
Ligands
Receptors
Target genes

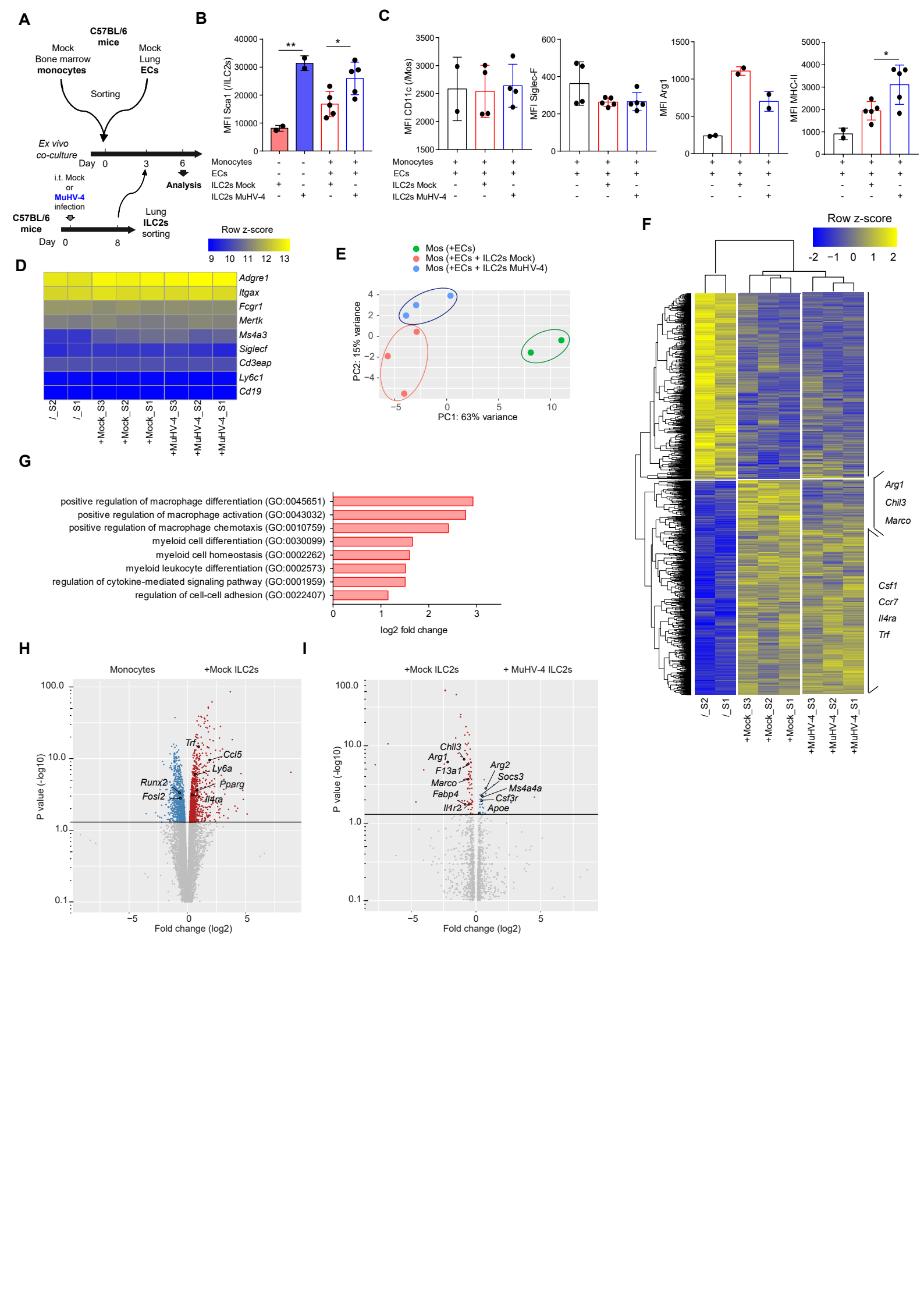
A
C57BL/6 mice
Mock Bone marrow monocytes
Mock Lung ECs
Sorting
Ex vivo co-culture
Day 0 3 6
Analysis
i.t. Mock or MuHV-4 infection
C57BL/6 mice
Day 0 8
Lung ILC2s sorting
B
MFI Sca1 (/ILC2s)
Monocytes
ECs
ILC2s Mock
ILC2s MuHV-4
C
MFI CD11c (/Mos)
MFI Siglec-F
MFI Arg1
MFI MHC-II
Row z-score
D
Adgre1
Itgax
Fcgr1
Mertk
Ms4a3
Siglecf
Cd3eap
Ly6c1
Cd19
/_S2
/_S1
+Mock_S3
+Mock_S2
+Mock_S1
+MuHV-4_S3
+MuHV-4_S2
+MuHV-4_S1
E
Mos (+ECs)
Mos (+ECs + ILC2s Mock)
Mos (+ECs + ILC2s MuHV-4)
PC2: 15% variance
PC1: 63% variance
F
Row z-score
Arg1
Chil3
Marco
Csf1
Ccr7
Il4ra
Trf
G
positive regulation of macrophage differentiation (GO:0045651)
positive regulation of macrophage activation (GO:0043032)
positive regulation of macrophage chemotaxis (GO:0010759)
myeloid cell differentiation (GO:0030099)
myeloid cell homeostasis (GO:0002262)
myeloid leukocyte differentiation (GO:0002573)
regulation of cytokine-mediated signaling pathway (GO:0001959)
regulation of cell-cell adhesion (GO:0022407)
log2 fold change
H
Monocytes
+Mock ILC2s
P value (-log10)
Trf
Ccl5
Ly6a
Runx2
Pparg
Fosl2
Il4ra
Fold change (log2)
I
+Mock ILC2s
+ MuHV-4 ILC2s
Chil3
Arg1
F13a1
Arg2
Socs3
Marco
Ms4a4a
Fabp4
Csf3r
Il1r2
Apoe
Fold change (log2)

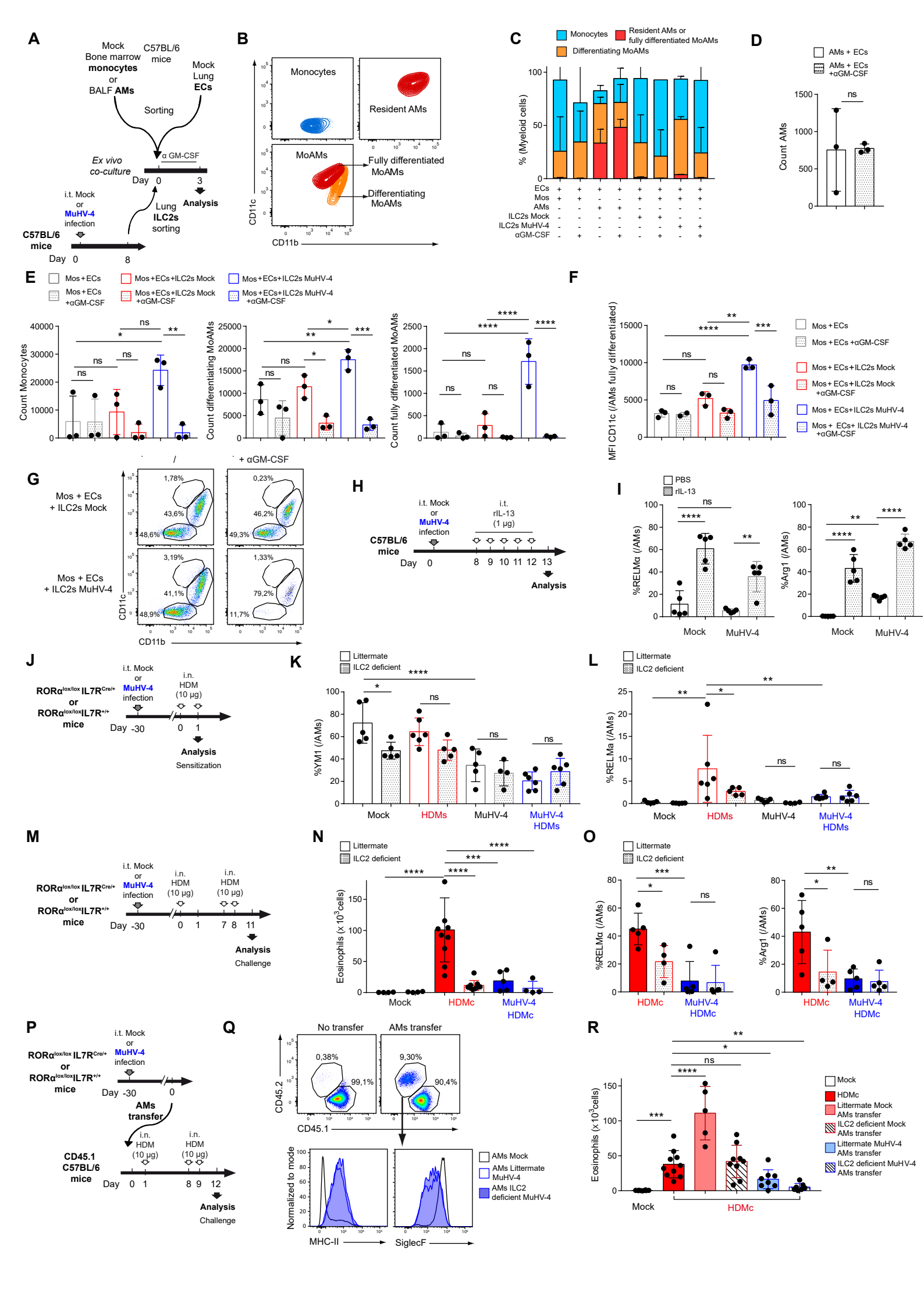
A
Mock Bone marrow monocytes or BALF AMs
C57BL/6 mice
Mock Lung ECs
Sorting
Ex vivo co-culture
α GM-CSF
Day 0
3
Analysis
i.t. Mock or MuHV-4 infection
C57BL/6 mice
Day 0
8
Lung ILC2s sorting
B
Monocytes
Resident AMs
MoAMs
Fully differentiated MoAMs
Differentiating MoAMs
CD11c
CD11b
C
Monocytes
Resident AMs or fully differentiated MoAMs
Differentiating MoAMs
% (Myeloid cells)
ECs
Mos
AMs
ILC2s Mock
ILC2s MuHV-4
αGM-CSF
D
AMs + ECs
AMs + ECs +αGM-CSF
Count AMs
ns
E
Mos+ECs
Mos+ECs +αGM-CSF
Mos+ECs+ILC2s Mock
Mos+ECs+ILC2s Mock +αGM-CSF
Mos+ECs+ILC2s MuHV-4
Mos+ECs+ILC2s MuHV-4 +αGM-CSF
Count Monocytes
Count differentiating MoAMs
Count fully differentiated MoAMs
/
+ αGM-CSF
F
MFI CD11c (/AMs fully differentiated)
Mos+ECs
Mos+ECs +αGM-CSF
Mos+ECs+ILC2s Mock
Mos+ECs+ILC2s Mock +αGM-CSF
Mos+ECs+ILC2s MuHV-4
Mos+ ECs+ ILC2s MuHV-4 +αGM-CSF
G
Mos + ECs + ILC2s Mock
Mos + ECs + ILC2s MuHV-4
1,78%
43,6%
48,6%
0,23%
46,2%
49,3%
3,19%
41,1%
48,9%
1,33%
79,2%
11,7%
CD11c
CD11b
H
i.t. Mock or MuHV-4 infection
C57BL/6 mice
Day 0
i.t. rIL-13 (1 µg)
8 9 10 11 12 13
Analysis
I
PBS
rIL-13
%RELMα (/AMs)
%Arg1 (/AMs)
Mock
MuHV-4
J
RORα lox/lox IL7R Cre/+ or RORα lox/lox IL7R +/+ mice
i.t. Mock or MuHV-4 infection
i.n. HDM (10 µg)
Day -30
0
1
Analysis
Sensitization
K
Littermate
ILC2 deficient
%YM1 (/AMs)
Mock
HDMs
MuHV-4
MuHV-4 HDMs
L
Littermate
ILC2 deficient
%RELMa (/AMs)
Mock
HDMs
MuHV-4
MuHV-4 HDMs
M
RORα lox/lox IL7R Cre/+ or RORα lox/lox IL7R +/+ mice
i.t. Mock or MuHV-4 infection
i.n. HDM (10 µg)
i.n. HDM (10 µg)
Day -30
0
1
7 8
11
Analysis
Challenge
N
Littermate
ILC2 deficient
Eosinophils (x 10³cells)
Mock
HDMc
MuHV-4 HDMc
O
Littermate
ILC2 deficient
%RELMα (/AMs)
%Arg1 (/AMs)
HDMc
MuHV-4 HDMc
P
RORα lox/lox IL7R Cre/+ or RORα lox/lox IL7R +/+ mice
i.t. Mock or MuHV-4 infection
Day -30
0
AMs transfer
CD45.1 C57BL/6 mice
i.n. HDM (10 µg)
i.n. HDM (10 µg)
Day 0 1
8 9 12
Analysis
Challenge
Q
No transfer
AMs transfer
0,38%
99,1%
9,30%
90,4%
CD45.2
CD45.1
Normalized to mode
MHC-II
SiglecF
AMs Mock
AMs Littermate MuHV-4
AMs ILC2 deficient MuHV-4
R
Eosinophils (x 10³cells)
Mock
HDMc
Littermate Mock AMs transfer
ILC2 deficient Mock AMs transfer
Littermate MuHV-4 AMs transfer
ILC2 deficient MuHV-4 AMs transfer

Supplementary Materials for

Dampening type 2 properties of group 2 innate lymphoid cells by a gammaherpesvirus infection reprograms alveolar macrophages

Loos P. *et al.*

Corresponding authors: Laurent Gillet l.gillet@uliege.be; Bénédicte Machiels bmachiels@uliege.be,

The file includes:

Supplementary Material and Methods

Figs. S1 to S5

Fig. S1. MuHV-4 infection affects the number and function of pulmonary ILC2s in C57BL/6 mice.

Fig. S2. Single cell transcriptomic analysis of lung ILCs and AMs from mock- or MuHV-4 infected-mice after HDM treatment and at different times post-infection.

Fig. S3. Transcriptional profiles of AMs and pulmonary ILC2s are modified following MuHV-4 infection and highlight potential interactions between these cells.

Fig. S4. ILC2s promote maturation of Mos into AM like cells.

Fig. S5. ILC2s failed to polarize resident AMs

Table S1

Table S1. Key resources

Other Supplementary Material for this manuscript includes the following:

Supplementary Movie 1. Reconstituted 3D image highlighting close contact between ILC2s and myeloid cells in lung at day 14 post MuHV-4 infection. Sytox staining is shown in blue, IL-5 in red, CD3 in green, CD68 in white, CD11b in magenta and CD11c in yellow.

Raw data file S1 (Excel spreadsheet)

Materials Design Analysis Reporting (MDAR) Checklist for Authors

Supplementary Material and Methods

Analysis of scRNA-seq samples.
Cell Ranger software (v.3.0.2) (10x Genomics) was used to demultiplex Illumina BCL files to FASTQ files (cellranger mkfastq), to perform alignment to mouse GRCm38/mm10 genome, filtering, UMI counting and to produce gene–barcode matrices (cellranger count). Subsequent analysis used R bioconductor (v.4.0.3) and the R package Seurat (v.2.1.5) (*1*). First, individual data sets were read into R as count matrices and converted into Seurat objects (min.cells = 3, min.features = 200 genes) cells with ≤ 200 ≥ 1500 (HDM data) or ≥ 6000 (MuHV-4 data) distinct genes and ≥ 5% (HDM data) or 8% (MuHV-4 data) of mitochondrial reads were filtered out. Each matrix were integrated using FindIntegrationAnchors with anchor.features = 2000 and dims = 1:30 options. Based on an elbow plot, principal components 1:10 (HDM data) or 1:20 (MuHV-4 data) were used in the subsequent analyses.

Cell types identification.
Cells were grouped in metacells (123 for HDM data and 102 for MuHV-4 data) using the FindCluster function of Seurat with a resolution of 10. Identification was made using the SingleR package (*2*).

UMAP representation.
Nonlinear dimensional reduction with UMAP was used to visualize the data sets, using the top 10 or 20 PCs (HDM and MuHV-4 data respectively). Non-integrated UMAP representations were generated based on the RNA assay of the Seurat object. The data were scaled on all the genes and the FindVariableFeatures with default option was run. Cells were clustered using the FindClusters function with a resolution of 0.2, 0.1, and 0.16 for HDM, MuHV-4 ILC2s, and MuHV-4 myeloid data respectively giving 5, 3, and 7 clusters respectively. In MuHV-4 data, the cluster 6 of myeloid cells was discarded, and clusters 0 and 5, 1 and 2, 3 and 4 were each grouped together, based on the gene expression profile and the scVelo analysis, into differentiated AMs, Mos differentiating into AMs, and Mos respectively.

RNA velocity analysis.
Kallisto (v.0.46.1) was used to perform pseudoalignment of RNA sequences. Loompy (v.3.0.6) was used to build a genome index with separate sequence fragments representing unspliced and spliced transcripts and to create a loom file including spliced and unspliced layers and metadata for genes and cells for each sample. The loom files were then processed in R to fuse samples, filter cells and map them to the existing UMAP, and convert the object into a h5ad file using Seurat, SeuratWrappers (v.0.3.0), SeuratDisk (v.0.0.0.9019), and velocyto.R (v.0.6) packages. The final figure was obtained using scVelo (v.0.2.4) in Jupyter notebook (v.6.2.0).

BubbleGUM analysis.
Bubblegum (*3*) analysis was used with default settings and the gene sets (containing between 20 and 500 genes) from Gene Ontology (13/11/2020) and gene set arbitrarily determined based on literature (*4*). The results with a FDR ≤ 0.25 were considered as significant.

NicheNet.
To study intercellular communication the NicheNet package for R was used (*5*). The top 20 ligands were kept and ‘mouse’ was selected for option organism in the function nichenet_seuratobj_aggregate.

Potential interaction scores.
In order to link NicheNet analysis with our data, we created the potential interaction score based on: average expression of ligand x average expression of receptor/target gene x weight of the interaction provide by the NicheNet package. The average expression of a gene is based on the Seurat package default calculation: log1p

(RNA count for this gene / total RNA count x 10.000). The weight of an interaction is retrieved from the corresponding databases of the NicheNet package.

Circlize.
The circular visualisation was made with the R package circlize (top 5% of the ligand-target genes scores and 50% top ligand-receptor scores) (*6, 7*). The intensity of the colour of the link between ligands and receptors is proportional to the score of the ligand-receptor link for each sender cell type (alpha from 0.25 to 1).

References

1. T. Stuart, A. Butler, P. Hoffman, C. Hafemeister, E. Papalexi, W. M. Mauck, Y. Hao, M. Stoeckius, P. Smibert, R. Satija, Comprehensive Integration of Single-Cell Data. *Cell*. **177**, 1888-1902.e21 (2019).

2. D. Aran, A. P. Looney, L. Liu, E. Wu, V. Fong, A. Hsu, S. Chak, R. P. Naikawadi, P. J. Wolters, A. R. Abate, A. J. Butte, M. Bhattacharya, Reference-based analysis of lung single-cell sequencing reveals a transitional profibrotic macrophage. *Nat. Immunol.* **20**, 163–172 (2019).

3. L. Spinelli, S. Carpentier, F. Montanana Sanchis, M. Dalod, T. P. Vu Manh, BubbleGUM: automatic extraction of phenotype molecular signatures and comprehensive visualization of multiple Gene Set Enrichment Analyses. *BMC Genomics*. **16**, 814 (2015).

4. B. Machiels, M. Dourcy, X. Xiao, J. Javaux, C. Mesnil, C. Sabatel, D. Desmecht, F. Lallemand, P. Martinive, H. Hammad, M. Guilliams, B. Dewals, A. Vanderplasschen, B. N. Lambrecht, F. Bureau, L. Gillet, A gammaherpesvirus provides protection against allergic asthma by inducing the replacement of resident alveolar macrophages with regulatory monocytes. *Nat. Immunol.* **18**, 1310–1320 (2017).

5. R. Browaeys, W. Saelens, Y. Saeys, NicheNet: modeling intercellular communication by linking ligands to target genes. *Nat. Methods*. **17**, 159–162 (2020).

6. J. Bonnardel, W. T'Jonck, D. Gaublomme, R. Browaeys, C. L. Scott, L. Martens, B. Vanneste, S. De Prijck, S. A. Nedospasov, A. Kremer, E. Van Hamme, P. Borghgraef, W. Toussaint, P. De Bleser, I. Mannaerts, A. Beschin, L. A. van Grunsven, B. N. Lambrecht, T. Taghon, S. Lippens, D. Elewaut, Y. Saeys, M. Guilliams, Stellate Cells, Hepatocytes, and Endothelial Cells Imprint the Kupffer Cell Identity on Monocytes Colonizing the Liver Macrophage Niche. *Immunity*. **51**, 638-654.e9 (2019).

7. Z. Gu, L. Gu, R. Eils, M. Schlesner, B. Brors, Circlize implements and enhances circular visualization in R. *Bioinformatics*. **30**, 2811–2812 (2014).

8. H. Adler, M. Messerle, M. Wagner, U. H. Koszinowski, "Cloning and Mutagenesis of the Murine Gammaherpesvirus 68 Genome as an Infectious Bacterial Artificial Chromosome" (2000).

Fig. S1. MuHV-4 infection affects the number and function of pulmonary ILC2s in C57BL/6 mice.

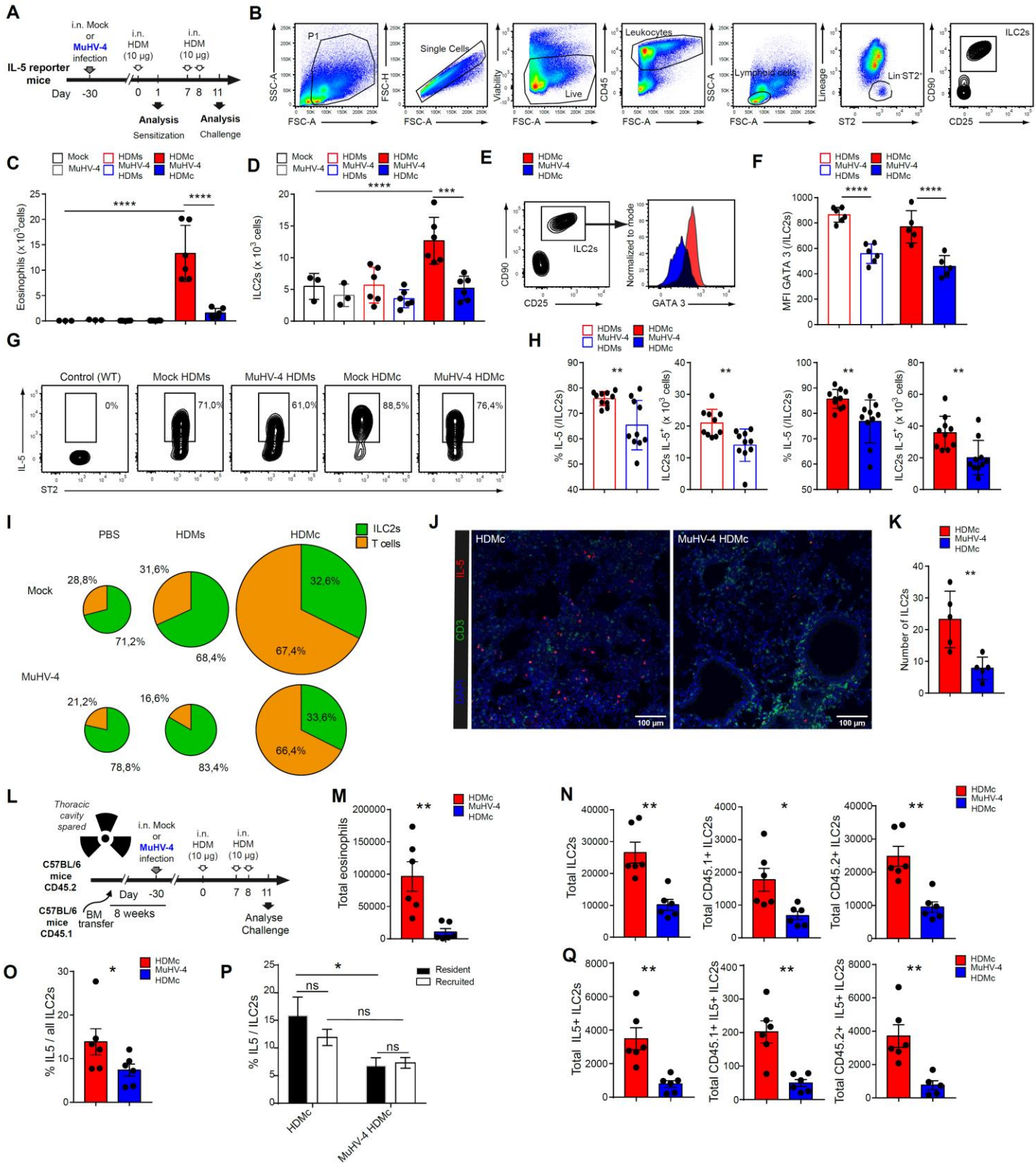

Fig. S1. MuHV-4 infection affects the number and function of pulmonary ILC2s in C57BL/6 mice.
8-week-old-Red5 (IL5-tdtomato-cre) reporter mice (n= 5 to 10 in each group) were infected or not with MuHV-4 and submitted to low-dose HDM sensitization or challenge before analysis.
(A) Experimental layout.
(B) Strategy for the identification of lung ILC2s by flow cytometry. Lineage was defined as B220, CD11c, CD3, CD49b, CD4, CD8α, F4/80, FcεRI, Gr1 and Siglec-F. ILC2s were described as $Lin^{-}CD45^{+}ST2^{+}CD90.2^{+}CD25^{+}$ living cells.
(C) Absolute numbers of eosinophils (gated as gated as out AMs (autofluorescent $CD11c^{+}SSC\text{-}A^{high}$) $Siglec\text{-}F^{+}CD11b^{+}$ living cells) in BALF.
(D) Absolute numbers of ILC2s in lung.
(E) Representative histograms of GATA 3 staining in lung ILC2s.
(F) MFI of GATA 3 staining in lung ILC2s.
(G) Flow cytometry plots of tdTomato/IL-5 fluorescence in lung ILC2s. Numbers indicate the percentage of positive cells in each quadrant.
(H) Percentage and total number of tdTomato/IL-5 positive cells among lung ILC2s.
(I) Circular diagrams of $IL\text{-}5^{+}$ lung cells of the indicated conditions. Area correspond to the relative amount of $IL\text{-}5^{+}$ cells in comparison with mock-infected mice. Numbers represent the percentage of ILC2s or T cells among tdTomato/IL-5 positive cells.
(J) Lungs of mock and MuHV-4 infected HDM challenged mice were submitted to 2D thin-cut, immunostained and imaged with ILC2s ($CD3^{-}$ $IL\text{-}5^{+}$ cells) and T-lymphocytes ($CD3^{+}$ cells). Images are representative of 3 mice.
(K) Numbers of ILC2s ($CD3^{-}$ $IL\text{-}5^{+}$ cells) observed in slides of indicated conditions.
(L-Q) 8 week-old-$CD45.2^{+}$ C57BL/6 mice were lethally irradiated, sparing the thoracic area, and transplanted with $CD45.1^{+}$ BM before being infected or not with MuHV-4 and submitted to a low-dose HDM challenge (n= 6 in each group).
(L) Experimental layout.
(M) Absolute numbers of eosinophils (out AMs (autofluorescent $CD11c^{+}SSC\text{-}A^{high}$) $Siglec\text{-}F^{+}CD11b^{+}$ living cells) from BALF.
(N) Absolute numbers of $CD45.1^{+}$ and $CD45.2^{+}$ cells among lung ILC2s.
(O) Percentage of IL-5 positive ILC2s in lung.
(P) Percentage of IL-5 positive ILC2s from resident or recruited lung ILC2s.
(Q) Absolute numbers of IL-5 positive lung ILC2s.
For comparisons between two groups, Student's two-tailed t test was used. For comparisons between multiple groups, one-way or two-way ANOVA was used with multiple-comparison tests. *P < 0.05, **P < 0.01, ***P < 0.001, and ****P < 0.0001. Bars show mean values ± SEM. Data represent two independent experiments with similar results.

Fig. S2. Single cell transcriptomic analysis of lung ILCs and AMs from mock- or MuHV-4 infected-mice after HDM treatment and at different times post-infection.

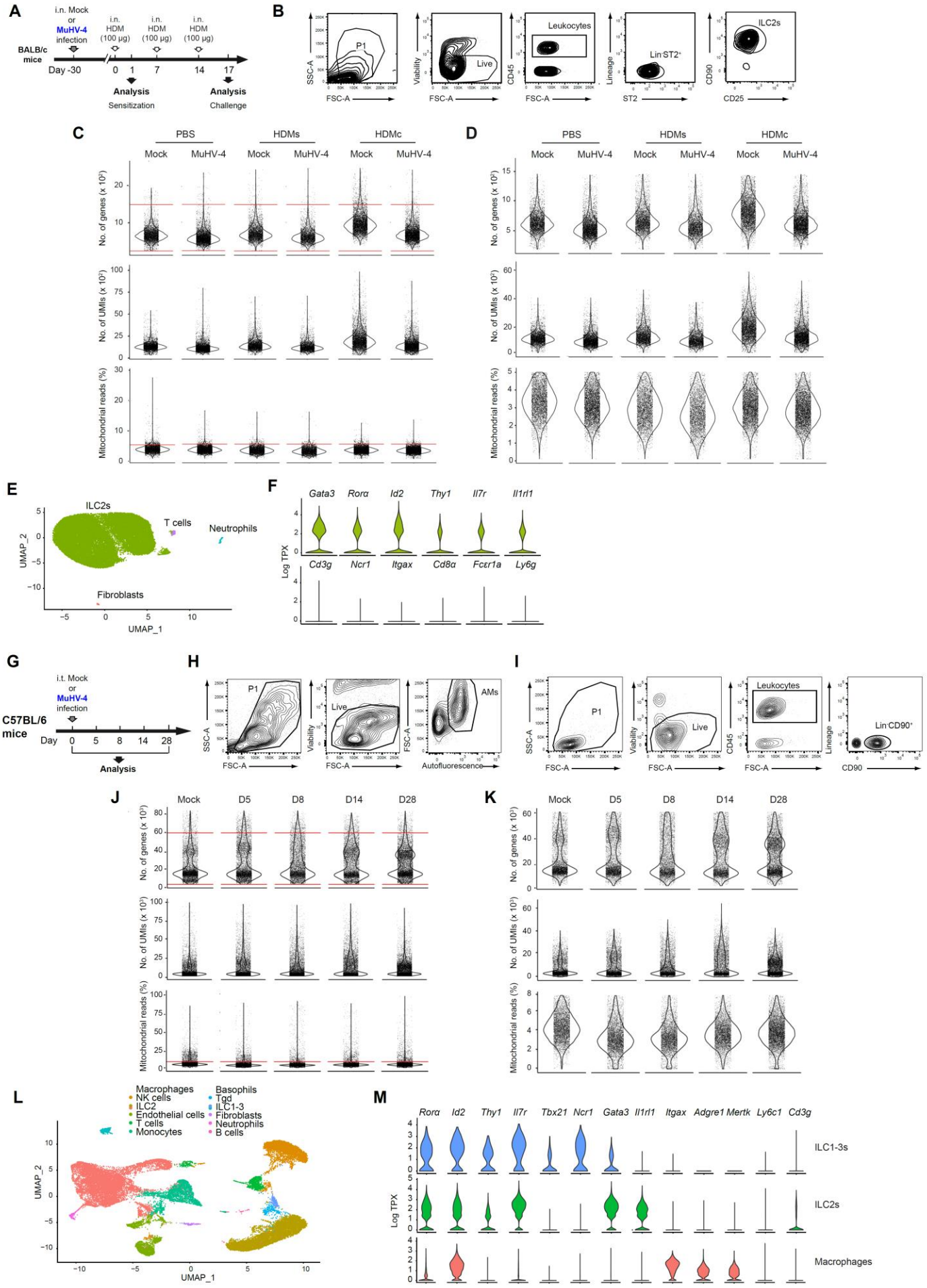
A
i.n. Mock or MuHV-4 infection
i.n. HDM (100 µg)
i.n. HDM (100 µg)
i.n. HDM (100 µg)
BALB/c mice
Day -30
0 1 7 14 17
Analysis
Sensitization
Analysis
Challenge
B
P1
Live
Leukocytes
Lin-ST2+
ILC2s
SSC-A
Viability
CD45
Lineage
ST2
CD90
CD25
FSC-A
C
PBS
HDMs
HDMc
Mock
MuHV-4
No. of genes (x 10³)
No. of UMIs (x 10³)
Mitochondrial reads (%)
D
E
ILC2s
T cells
Neutrophils
Fibroblasts
UMAP_1
UMAP_2
F
Gata3
Rorα
Id2
Thy1
Il7r
Il1rl1
Cd3g
Ncr1
Itgax
Cd8α
Fcεr1a
Ly6g
Log TPX
G
i.t. Mock or MuHV-4 infection
C57BL/6 mice
Day 0 5 8 14 28
Analysis
H
AMs
Autofluorescence
I
Lin-CD90+
CD90
J
Mock
D5
D8
D14
D28
K
L
Macrophages
NK cells
ILC2
Endothelial cells
T cells
Monocytes
Basophils
Tgd
ILC1-3
Fibroblasts
Neutrophils
B cells
M
Rorα
Id2
Thy1
Il7r
Tbx21
Ncr1
Gata3
Il1rl1
Itgax
Adgre1
Mertk
Ly6c1
Cd3g
ILC1-3s
ILC2s
Macrophages

Fig. S2. Single cell transcriptomic analysis of lung ILCs and AMs from mock- or MuHV-4 infected-mice after HDM treatment and at different times post-infection.

(A-F) Lung ILC2s from mock- or MuHV-4 infected mice submitted or not to HDM sensitization or challenge were profiled by droplet-based single cell RNA-sequencing.

(A) Experimental layout.

(B) Strategy for FACS sorting of lung ILC2s after MACS negative enrichment against lineage markers (B220, CD11c, CD3, CD4, CD49b, CD5, CD8α, F4/80, FcεR1, Gr1 and Siglec-F). ILC2s were identified as $Lin^{-}CD45^{+}ST2^{+}CD90.2^{+}CD25^{+}$ living cells. (n = 7 pooled mice per group). Cells from a mock-infected mouse are shown.

(C-D) Gene counts, Unique Molecular Identifiers (UMI) counts and percentage of mitochondrial genes detected in the indicated conditions before (C) and after (D) selection and filtering as described in the methods, presented as violin plots (individual dots representing individual cells).

(E) Non-linear representation (UMAP) of the top 15 PCs of all data, cells' identification was performed by the SingleR package.

(F) Violin plots of indicated genes expression for the 6 merged conditions.

(G-M) Lung ILC2s and BALF AMs from mock- or MuHV-4 infected C57BL/6 mice were profiled by droplet-based single cell RNA-sequencing.

(G) Experimental layout.

(H-I) Strategy for FACS sorting of lung ILCs after MACS negative enrichment against lineage markers (B220, CD11c, CD3, CD4, CD5, CD8α, F4/80, FcεR1, Gr1 and Siglec-F) and of BALF AMs. ILCs were identified as $Lin^{-}CD45^{+}CD90.2^{+}$ living cells (H) and AMs were identified as live large autofluorescent cells (I). One MuHV-4-infected (D14 p.i) mouse is shown. scRNA seq analysis was performed on cells from 7 pooled mice per group.

(J-K) Gene counts, Unique Molecular Identifiers (UMI) counts and percentage of mitochondrial genes detected in the indicated conditions before (J) and after (K) selection and filtering as described in the methods, presented as violin plots (individual dots representing individual cells).

(L) Non-linear representation (UMAP) of the top 20 PCs of all data, cells' identification was performed by the SingleR package.

(M) Violin plots of indicated genes expression for the 5 merged conditions.

Analyses were performed using R.

Fig. S3. Transcriptional profiles of AMs and pulmonary ILC2s are modified following MuHV-4 infection and highlight potential interactions between these cells.

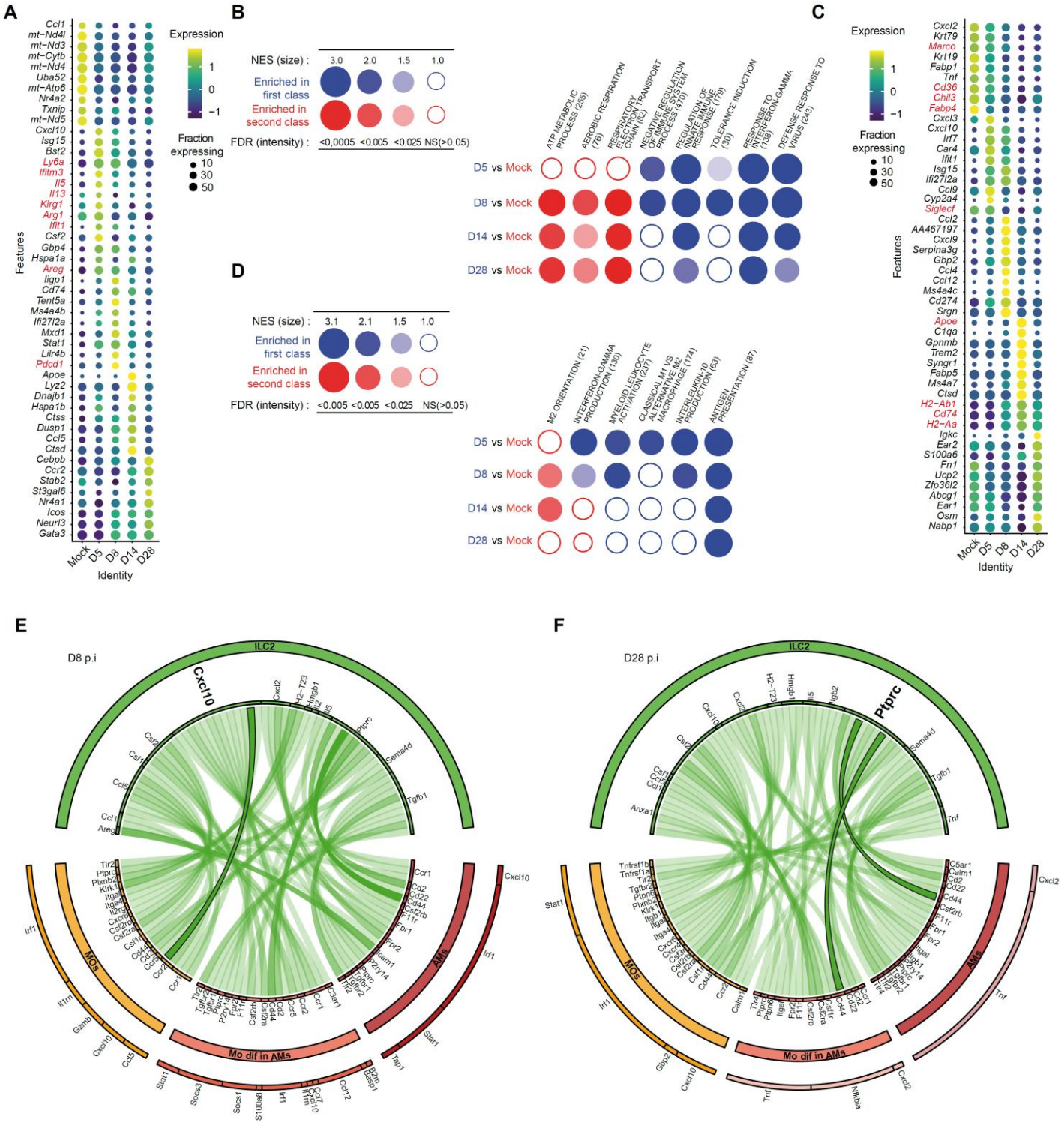

Fig. S3. Transcriptional profiles of AMs and pulmonary ILC2s are modified following MuHV-4 infection and highlight potential interactions between these cells.

Lung ILC2s (gated as CD45+Lin-CD90.2+ living cells) and BALF AMs (gated as autofluorescent CD11c+ living cells) from mock or MuHV-4 infected-8-week-old at different times post-infection.

(A, C) Relative expression of the 10 most expressed genes (y axis) at each different times post-infection (x axis) in ILC2s (A) and AMs (C).

(B, D) Enrichment for transcriptomic fingerprints specific for Gene Ontology sets by gene set enrichment analysis with BubbleGum software in ILC2s (C) and AMs (D). The color indicates the cell subset showing enrichment for the gene set. The surface area of the dots is proportional to the absolute value of the normalized enrichment score (NES). The color intensity indicates FDR. Numbers in parentheses indicate the number of genes in each gene set. NS, not significant.

(E-F) Circular plot of the putative interactions between ILC2s' ligands (top), AMs' receptors (bottom) and the target genes activated by these interactions (up- or down-regulated) in AMs based on their expression at day 8 (E) and 28 (F) post-MuHV-4 infection. Opacity of the link correlates with the interaction score (alpha from 0.25 to 1).

Fig. S4. ILC2s promote maturation of Mos into AM like cells.

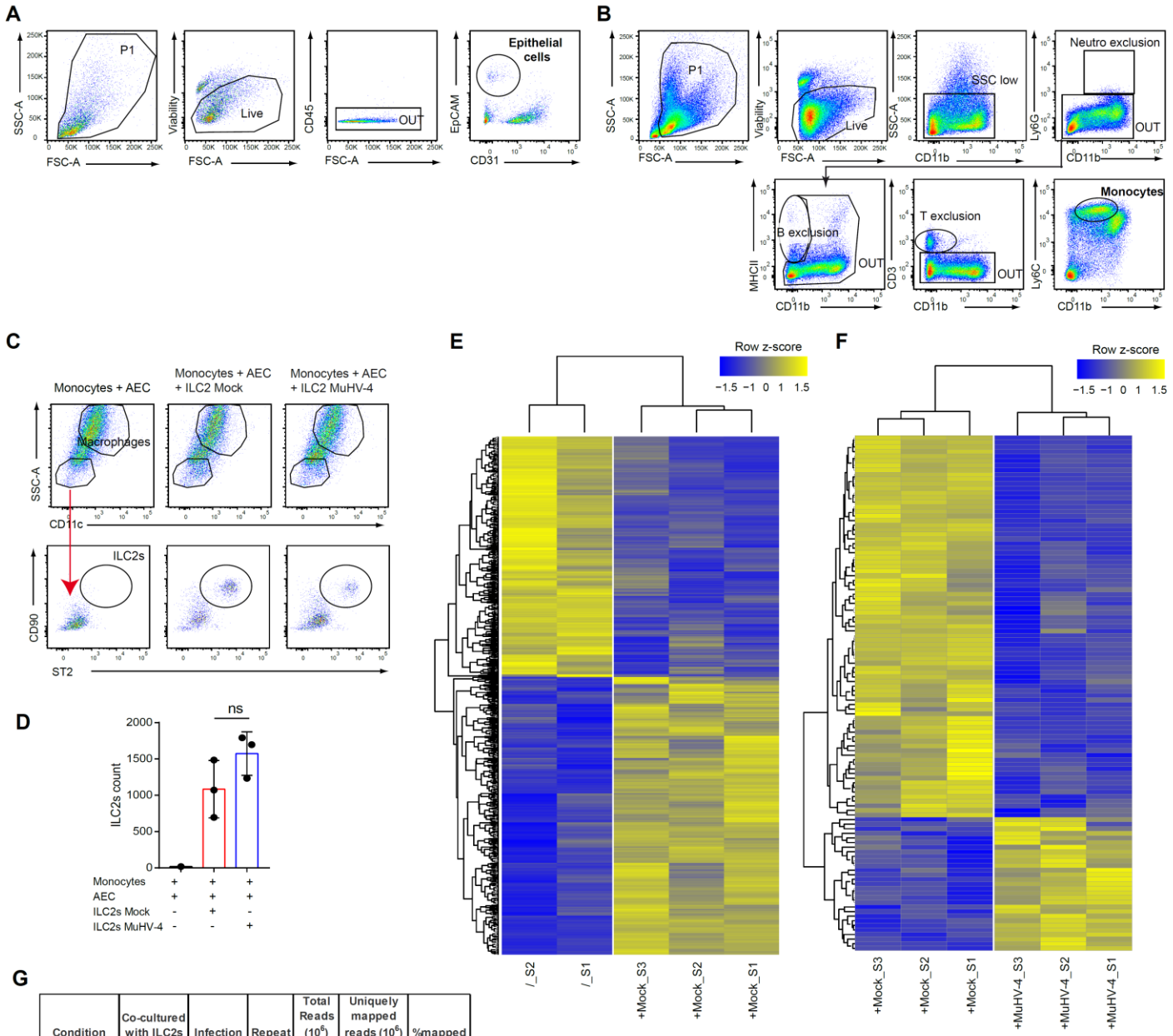

G

Condition	Co-cultured with ILC2s	Infection	Repeat	Total Reads (10^6)	Uniquely mapped reads (10^6)	%mapped
Macro_S1	None	Mock	1	24,8	20,8	0,84
Macro_S2	None	Mock	2	27,9	23,2	0,83
+Mock_S1	ILC2s	Mock	1	22,1	19,2	0,87
+Mock_S2	ILC2s	Mock	2	24,7	21	0,86
+Mock_S3	ILC2s	Mock	3	26,9	23,4	0,87
+MuHV-4_S1	ILC2s	MuHV-4	1	25,4	22,1	0,87
+MuHV-4_S2	ILC2s	MuHV-4	2	22,6	19,6	0,87
+MuHV-4_S3	ILC2s	MuHV-4	3	23,6	20,4	0,87

Fig. S4. ILC2s promote maturation of Mos into AM-like cells.

Lung Mos, ECs and ILC2s from mock- or MuHV-4 infected-mice were co-cultured as described in Figure 7.

(A) Gating strategy for FACS sorting of lung ECs, described as CD45-CD31-Epcam+ living cells after CD45 MACS depletion.

(B) Gating strategy for FACS sorting of BM Mos, described as SSC-AlowLy6C+CD11b+ living cells after exclusion of neutrophils (Ly6G+CD11b+), B cells (MHCII+CD11b-), T cells (CD3+ CD11b-) after cell enrichment through MACS negative selection (L6G and B220).

(C) Flow cytometry plots for AMs-like and ILC2s on the indicated conditions.

(D-E) Heatmap of all genes differentially expressed (FDR<0,05; change in expression of over twofold) (two to three biological replicates) in Mos.

(F) Sequence reads and mapping statistics for raw Illumina data.

Fig. S5. ILC2s failed to polarize resident AMs

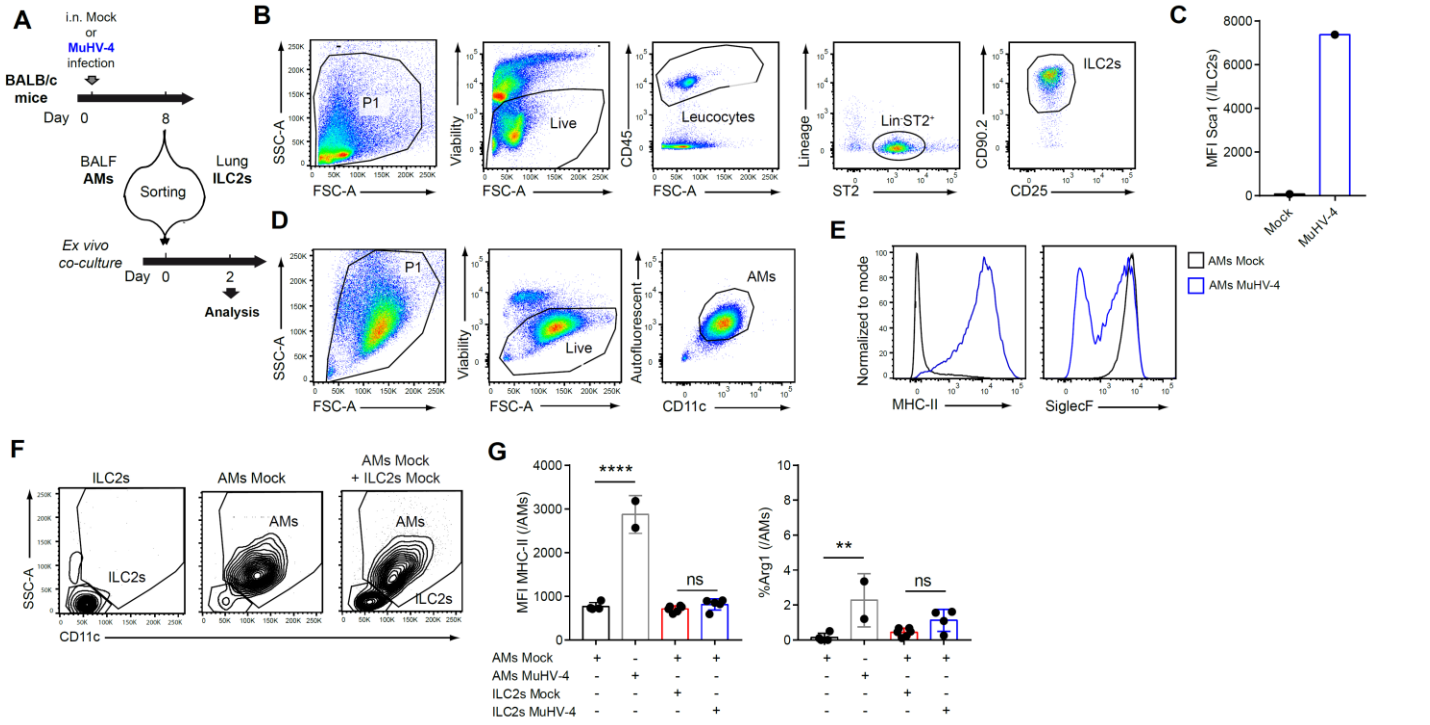

Fig. S5. ILC2s failed to polarize resident AMs.

BALF AMs and ILC2s from mock- or MuHV-4 infected-mice were co-cultured ex-vivo during 2 days.

(A) Experimental layout.

(B) Strategy for FACS sorting of lung ILC2s after MACS negative enrichment against lineage markers (B220, CD11c, CD3, CD4, CD49b, CD5, CD8α, F4/80, FcεR1, Gr1 and Siglec-F). ILC2s were identified as Lin-CD45+ST2+CD90.2+CD25+ living cells. (n = 7 pooled mice per group). Cells from a mock-infected mouse are shown.

(C) MFI of Sca1 staining in lung ILC2s.

(D) Gating strategy for FACS sorting of BALF AMs, described as Autofluorescent CD11c+ living cells after CD11c MACS enrichment.

(E) Histograms of MHC-II and Siglec-F staining in BALF AMs.

(F) Flow cytometry plots for AMs and ILC2s on the indicated conditions.

(G) MFI of MHC-II and percentage of Arg1 in AMs.

For comparisons between two groups, Student's two-tailed t test was used. For comparisons between multiple groups, one-way or two-way ANOVA was used with multiple-comparison tests. *P < 0.05, **P < 0.01, ***P < 0.001, and ****P < 0.0001.

Bars show mean values ± SEM.

Table S1. Key resources used in this study

REAGENT or RESOURCE	SOURCE	IDENTIFIER
Antibodies		
Anti-mouse Arginase 1, PE-Cy7, eBioscience™ (clone: A1exF5)	Thermo Fisher Scientific	Cat# 25-3697-82, RRID: AB_2734841
Anti-mouse CD11b, BV605 (clone M1/70)	BioLegend	Cat# 101237, RRID:AB_11126744
Anti-mouse CD11b, FITC (clone M1/70)	BioLegend	Cat# 101205, RRID: AB_312788
Anti-mouse CD11b, BV711 (clone M1/70)	BD Biosciences	Cat# 563168, RRID: AB_2716860
Anti-mouse CD11b, eF660 (clone M1/70)	Thermo Fisher Scientific	Cat# 50-0112-82, RRID: AB_11218507
Anti-mouse CD11c, APC (clone N418)	BioLegend	Cat# 117309, RRID: AB_313778
Anti-mouse CD11c, Alexa Fluor 488, eBioscience™ (clone N418)	Thermo Fisher Scientific	Cat# 56-0114-82, RRID: AB_493992
Anti-mouse CD11c, Alexa Fluor 700, eBioscience™ (clone N418)	Thermo Fisher Scientific	Cat# 56-0114-82, RRID: AB_493992
Anti-mouse CD16/32, Fc block (clone 93)	BioLegend	Cat# 101301, RRID:AB_312800
Anti-mouse CD19, APC/Cyanine7 (clone 6D5)	BioLegend	Cat# 115529, RRID:AB_830706
Anti-mouse CD25, Alexa Fluor 700 (clone PC61)	BioLegend	Cat# 102024, RRID:AB_493709
Anti-mouse CD274, APC (clone 10F.9G2)	BioLegend	Cat# 124311, RRID:AB_10612935
Anti-mouse CD274, BV711 (clone 10F.9G2)	BioLegend	Cat# 124319, RRID: AB_2563619
Anti-mouse CD279, APC/Fire (clone 29F.1A12)	BioLegend	Cat# 135239, RRID: AB_2563619
Anti-mouse CD3 (clone 17A2)	BioLegend	Cat# 100201; RRID: AB_312658
Anti-mouse CD3e, APC-Cy7 (clone 145-2C11)	BD Biosciences	Cat# 557596, RRID: AB_396759
Anti-mouse CD3e, BV421 (clone 145-2C11)	BD Biosciences	Cat# 100335, RRID: B_10898314
Anti-mouse CD3e, FITC (clone 145-2C11)	BioLegend	Cat# 100306, RRID:AB_312671
Anti-mouse CD3e, APC (clone 145-2C11)	BioLegend	Cat# 100311, RRID: AB_312676
Anti-mouse CD31, PE (clone: MEC13.3)	BioLegend	Cat# 102507, RRID:AB_312914
Anti-mouse CD326 (Ep-CAM), Alexa Fluor 488 (clone: G8.8)	BioLegend	Cat# 118210, RRID:AB_ 1134099
Anti-mouse CD4, APC (clone RM 4-5)	BioLegend	Cat# 100515, RRID:AB_312718
Anti-mouse CD4, BV421 (clone GK1.5)	BioLegend	Cat# 100405, RRID: AB_312690
Anti-mouse CD45, BV510 (clone 30-F11)	BioLegend	Cat# 103137, RRID:AB_2561392
Anti-mouse CD45, PE/Cyanine7 (clone 30-F11)	BioLegend	Cat# 103114, RRID:AB_312979

Anti-mouse CD45.1, APC (clone A20)	BioLegend	Cat# 110713, RRID:AB_313502
Anti-mouse CD45.1, BV421 (clone A20)	BioLegend	Cat# 110731, RRID: AB_10896425
Anti-mouse CD45.2, BV510 (clone 104)	BioLegend	Cat# 109837, RRID:AB_2561393
Anti-mouse CD45.2, PE/Cy7 (clone 104)	BioLegend	Cat# 109837, RRID: AB_1186103
Anti-mouse CD45R/B220, APC (clone RA3-6B2)	BioLegend	Cat# 103211, RRID: AB_312996
Anti-mouse CD49b, APC (clone DX5)	BioLegend	Cat# 108910, RRID:AB_313417
Anti-mouse CD5, APC, (clone: 53-7.3)	BioLegend	Cat#100625, RRID: AB_2563928
Anti-mouse CD68 purified (clone FA-11)	Thermo Fisher Scientific	Cat# 14-0681-82, RRID:AB_2572857
Anti-mouse CD8α, APC (clone 53-6.7)	BioLegend	Cat# 100711, RRID:AB_312750
Anti-mouse CD8α, PerCP/Cyanine5.5 (clone 53-6.7)	BioLegend	Cat# 100733, RRID:AB_2075239
Anti-mouse CD86, APC/Cy7, (clone: GL1)	BioLegend	Cat# 105029, RRID: AB_2074993
Anti-mouse CD90.2, BV421 (clone 53-2.1)	BioLegend	Cat# 140327, RRID: AB_2686992
Anti-mouse CD90.2, BV711 (clone 53-2.1)	BD Biosciences	Cat# 740647, RRID: AB_2740336
Anti-mouse F4/80, APC (clone BM8)	BioLegend	Cat# 123115, RRID: AB_893493
Anti-mouse FCεRIα, APC (clone MAR-1)	BioLegend	Cat# 134315, RRID: AB_10640726
Anti-mouse FOXP3, PE, eBioscience™ (clone: FJK-16S)	Thermo Fisher Scientific	Cat#12-5773-80, RRID: AB_465935
Anti-mouse GATA-3, PE, eBioscience™ (clone: TWAJ)	Thermo Fisher Scientific	Cat# 12-9966-42, RRID: AB_1963600
Anti-mouse I-A/I-E, FITC (clone M5/114.15.2)	BioLegend	Cat# 107605, RRID: AB_313320
Anti-mouse iNOS, PE, eBioscience™ (clone: CXNFT)	Thermo Fisher Scientific	Cat# 12-5920-82, RRID: AB_2572642
Anti-mouse I-A/I-E, PE/Cyanine7 (clone M5/114.15.2)	BioLegend	Cat# 107630, RRID:AB_2069376
Anti-mouse IFN-γ, BV711 (clone XMG1.2)	BioLegend	Cat# 505836, RRID:AB_2650928
Anti-mouse IL-5, BV421 (clone: TRFK5)	BioLegend	Cat# 504311, RRID: AB_2563161
Anti-mouse IL-5, PE (clone: TRFK5)	BioLegend	Cat# 504303 RRID: AB_315327
Anti-mouse IL-13, Alexa Fluor 488, eBioscience™ (clone: eBio13A)	Thermo Fisher Scientific	Cat#53-7133-82, RRID: AB_2016708
Anti-mouse Ki-67, Alexa Fluor 488 (clone: 16A8)	BioLegend	Cat# 652417, RRID:AB_2564236
Anti-mouse Ki-67, Alexa Fluor 488 (clone: 16A8)	BioLegend	Cat# 652403, RRID: AB_2561524
Anti-mouse KLRG1, BV711 (clone: 2F1)	BioLegend	Cat# 138427, RRID: AB_2629721
Anti-mouse KLRG1, BV86 (clone: 2F1)	BD Biosciences	Cat# 561620, RRID: AB_10895798
Anti-mouse Ly6A/E, FITC (clone D7)	BioLegend	Cat# 122506, RRID:AB_756191

Anti-mouse Ly6C, BV785 (clone HK1.4)	BioLegend	Cat# 128041, RRID:AB_2565852
Anti-mouse Ly6C, PE, eBioscience™ (clone: HK1.4)	Thermo Fisher Scientific	Cat# 12-5932-82, RRID: AB_10804510
Anti-mouse Ly-6G/Ly-6C (Gr-1), APC (clone RB6-8C5)	BioLegend	Cat# 108411, RRID: AB_313376
Anti-mouse Ly6G, APC-Cy7 (clone 1A8)	BD Biosciences	Cat# 560600, RRID:AB_1727561
Anti-mouse NK1.1, PE-Cy7, eBioscience™ (clone: PK136)	Thermo Fisher Scientific	Cat# 25-5941-82, RRID: AB_469665
Anti-mouse RELMα, PE, eBioscience™ (clone: DS8RELM)	Thermo Fisher Scientific	Cat# 12-5441-82, RRID: AB_2762682
Anti-mouse SiglecF, APC (clone S17007L)	BioLegend	Cat# 155507, RRID: AB_2750236
Anti-mouse SiglecF, PE (clone E50-2440)	BD Biosciences	Cat# 552126, RRID: AB_394341
Anti-mouse SiglecF, PE-CF594 (clone E50-2440)	BD Biosciences	Cat# 562757, RRID: AB_2687994
Anti-mouse ST2, BV421 (clone DIH9)	BioLegend	Cat# 145309, RRID: AB_2565634
Anti-mouse ST2, PE (clone DIH9)	BioLegend	Cat# 145303, RRID: AB_2561914
Anti-mouse T-bet, PE, eBioscience™ (clone: eBio4B10)	Thermo Fisher Scientific	Cat# 12-5825-82, RRID: AB_925761
Anti-rat IgG2a, Secondary Antibody, Alexa Fluor® 594	BioLegend	Cat# 407509 RRID: AB_2650845
Anti-Rat IgG2b, Secondary Antibody, Biotin	BioLegend	Cat# 408203; RRID: AB_492999
Goat Anti-mouse YM1/Chitinase 3-like 3 Biotinylated Antibody	R&D Systems	Cat# BAF2446 , RRID: AB_2260451
Goat anti-Rabbit IgG (H+L) Cross-Adsorbed Secondary Antibody, Alexa Fluor™ 594	Thermo Fisher Scientific	Cat# A-11012; RRID: AB_2534079
Living Colors® DsRed Polyclonal Antibody	Takara	Cat# 632496; RRID: AB_10013483
Bacterial and Virus strains		
MHV-68 pHA3 strain (MuHV-4)	Stevenson Laboratory	Adler et al., 2000
MuHV-4 del73	Stevenson Laboratory	Fowler et al., 2004
Chemicals, peptides, and recombinant proteins		
1X RBC Lysis Buffer	Thermo Fisher Scientific	Cat# 00433357
7-AAD	BioLegend	Cat# 420403
Annexin V FITC	BioLegend	Cat# 640905, RRID: AB_2561291
Brefeldin A Solution	BioLegend	Cat# 420601
Cell Dissociation Buffer, enzyme-free, PBS	Thermo Fisher Scientific	Cat# 13151014
cOmplete™ Protease Inhibitor Cocktail	Roche	Cat# 11697498001
DAPI (4',6-Diamidino-2-Phenylindole, Dilactate)	BioLegend	Cat# 422801
Dispase	Sigma-Aldrich	Cat# D4818
DNase I	Roche	Cat# 11284932001

Liberase	Roche	Cat# 5401127001
Emdotrim 10% SOL	Emdoka	N/A
Fixable Viability Dye eFluor 780	Thermo Fisher Scientific	Cat# 65-0865-14
Extracts of lyophilized HDM (*Dermatophagoides farina*)	Greer Laboratories	Cat# XPB81D3A2.5
InVivoMAb anti-mouse GM-CSF (MP1-22E9)	BioXCell	Cat# BE0259
Ionomycin	Sigma-Aldrich	Cat# I9657
Monensin Solution	BioLegend	Cat# 420701
Phorbol 12-myristate 13-acetate	Sigma-Aldrich	Cat# 79346
ProLongTM Gold Antifade Mountant mounting media	Thermo Fisher Scientific	Cat# P10144
SYTOX™ Blue Dead Cell Stain	Thermo Fisher Scientific	Cat#S34857
Scigen O.C.T. Compound Cryostat Embedding Medium	Thermo Fisher Scientific	Cat# 23-730-625
SIGMAFAST™ p-Nitrophenyl phosphate Tablets	Sigma-Aldrich	Cat# N-1891
Recombinant mouse IL-2	BioLegend	Cat# 575402
Recombinant mouse IL-13	BioLegend	Cat# 575904
Streptavidin APC	BD Biosciences	Cat# 554067
Streptavidin BV421	BioLegend	Cat# 405226
Streptavidin FITC	Thermo Fisher Scientific	Cat# SA1001
TRIzol	Thermo Fisher Scientific	Cat# 15596026
Tuerk solution	Sigma-Aldrich	Cat# 93770
Zombie Aqua Fixable Viability Kit	BioLegend	Cat# 423101
Zombie Violet Fixable Viability Kit	BioLegend	Cat# 423113
β-mercaptoethanol	Sigma-Aldrich	Cat# 3148
Critical commercial assays		
CD11c MicroBeads UltraPure, mouse	Miltenyi	Cat# 130-125-835
FoxP3/transcription factor staining buffer kit	Thermo Fisher Scientific	Cat# 00-5523-00
GentleMACS C tube	Miltenyi	Cat# 130-093-237
iQ™ Supermix	Bio-Rad	Cat# 170-8860
iScript™ cDNA Synthesis Kit	Bio-Rad	Cat# 170-8897
LD columns	Miltenyi	Cat# 130-042-901
MojoSort™ Mouse anti-APC Nanobeads	BioLegend	Cat# 480071

MojoSort™ Mouse anti-CD45 Nanobeads	BioLegend	Cat# 480028
Mouse IFN gamma ELISA Ready-SET-Go	Fisher Scientific	Cat# 88-7314-88, RRID:AB_2575070
Mouse IL-5 ELISA Ready-SET-Go	Fisher Scientific	Cat# 88-7054-86, RRID: AB_2574979
Mouse IL-13 ELISA Ready-SET-Go	Fisher Scientific	Cat# 88-7439-22, RRID: AB_2575122
RNeasy mini kit	Qiagen	Cat# 74106
Experimental models: Cell lines		
Baby hamster kidney (BHK)-21 cells	ATCC	ATCC Cat# CCL-10, RRID:CVCL_1915
Experimental models: Organisms/strains		
Mouse : C57BL/6J (JAX™)	Charles River	Cat# JAX:000664, RRID:IMSR_JAX:000664)
Mouse: C57BL/6 Il5$^{tm1.1(icre)Lky}$ (Red5/R5 or IL5-tdtomato-cre)	The Jackson Laboratory	Cat#030926, RRID: IMSR_JAX:030926
Mouse : BALB/cByJ CD45.1^{+}	The Jackson Laboratory	Cat#006584, RRID: IMSR_JAX:006584
Mouse : BALB/cAnNCrl	Charles River	Cat# CRL:028, RRID:IMSR_CRL:028
Mouse : C57BL/6 CD45.1^{+}	Charles River	Cat# CRL:494, RRID:IMSR_CRL:494
Mouse : C57BL/6 CD45.1^{+}.2^{+}	GIGA	N/A
Mouse : C57BL/6 IFN-γR-/-	The Jackson Laboratory	Cat# JAX :004999, RRID:IMSR_JAX:004999
Mouse : C57BL/6 Ifng$^{tm3.1Lky}$ (Great mice)	The Jackson Laboratory	Cat# JAX :017580, RRID:IMSR_JAX:017580
Mouse: C57BL/6 Rora$^{fl/sg}$ Il7rCre	Prof. A. N.J. McKenzie (Cambridge, UK) and Prof. H. Rodewald (Heidelberg, Ger)	Olifant et al., 2014
Oligonucleotides		
IL-33 reverse : TTG-TGA-AGG-ACG-AAG-AAG-GC	Eurogentec	N/A
IL-33 forward : GAT-GGG-AAG-AAG-CTG-ATG-GTG	Eurogentec	N/A
Software and algorithms		
FlowJo software v10	Three Star	https://www.flowjo.com
GraphPad Prism 7	GraphPad	https://www.graphpad.com/scientific-software/prism/
Fiji software	ImageJ	https://imagej.net/software/fiji/
R (v.4.1.0), R package Seurat (v.4.0.3)	The R Foundation	http://www.r-project.org/
Fiji software	ImageJ	https://imagej.net/software/fiji/

Imaris Microscopy Image Analysis Software	OXFORD instruments	https://imaris.oxinst.com/